Processing, microstructure and properties of polymer-based nano-composite dielectrics for capacitor applications



Amoghavarsha Mahadevegowda

Kellogg College

University of Oxford

A thesis submitted for the degree of

Doctor of Philosophy in Materials

Trinity 2014

Acknowledgements

I owe a great deal of gratitude to my supervisor Prof. Patrick S Grant for his guidance and support throughout the course of my research at Oxford. The super-productive discussions studded with insights from his rich experience and intellect helped to hone my scientific skills and finely moulded my research. His invaluable advice and feedback on my work have been immensely useful in producing high quality research, scientific reports and presentations. I am extremely grateful for his patience and for giving me the freedom to work at my own comfortable pace which helped me to try out a number of new ideas that had a significant impact on my research. I would like to thank him for supporting my application to the department's continuation bursary and providing financial assistance to finish my DPhil. He was also instrumental in helping me to secure the Felix Scholarship by providing a recommendation letter and useful tips for the scholarship interview. Many thanks to him for teaching me a better technique to manoeuvre the boat while punting on the river Cherwell - very useful for punt-races. However, moving like a snake, hitting the banks of the river and dodging (sometimes hanging on to) low lying branches is so much fun.

I am deeply indebted to my co-supervisor Dr. Neil P Young for his constant encouragement, guidance and support. He has been very kind and patient in teaching me the theoretical and practical aspects of transmission electron microscopy (TEM). In the course of learning TEM, he has always been very welcoming to even my ignorant and silly questions and invested a lot of time in training me on many microscopes that played a key role in my research. He also sat down with me in the TEM suite on numerous occasions while dealing with an arduous problem that then seemed impossible to crack, and keenly looked at my data analysis and gave feedback. His expertise guided me in carrying out cutting-edge research via the state-of-art machines and helped to give a better and fuller picture to my thesis.

I would like to extend my sincere gratitude to Dr. Colin Johnston, Dr. Alison Crossley, Dr. Hugh Bishop, Dr. Andrew Cook, Ms. Gabriella Chapman, Mr. Chris Salter, Mr. Richard Turner, Dr. Andrew Watt, Dr. Peter Kovacik, Dr. Judy Kim, Mr. Ron Doole, Dr. Rebecca Nicholls, Prof. Angus Kirkland, Prof. Peter Nellist, Dr. Kerstin Jurkschat, and Dr. Radka Chakalova for kindly training me on numerous machines, addressing my queries, and sharing facilities and knowledge.

My special thanks to Ms. Jan Pearson, Ms. Julie Young, Dr. Adrian Taylor, Ms. Marion Beckett, Mr. Barry Fellows, Mr. Ian Sutton, Dr. Paul Warren, and Mr. Shaun Boyce for various forms of assistance.

Many thanks to my peeps in my lab and department for many casual chats and stimulating discussions.

My sincere thanks to my family (especially appa, amma and ammu) and teachers for incessantly bestowing me with love and knowledge. They made me a learned person capable enough to take up doctoral studies at Oxford, and more importantly taught me the way of life that I practise, evolve and celebrate everyday.

I read somewhere that each friend represents a world in us, and my friends at home, department and away created many exciting and cherishable mini-worlds for me. My heartfelt thanks to my dear friends for sharing their world with me and creating a plethora of invaluable, incredible (the OMG moments) and indelible memories.

I would like to thank the UK Engineering and Physical Sciences Research Council, the Defence Science and Technology Laboratory - UK, the Felix Scholarship, the Department of Materials and Kellogg College for supporting my study at Oxford.

Abstract

The processing and properties of novel polymer-based nano-composite (PNC) dielectrics for capacitor applications has been studied. PNCs were fabricated via a vacuum based deposition technique and their micro/nano-structure, chemical and dielectric properties investigated. After process development and optimisation, co-deposited Al and nylon-6 PNCs had a dielectric constant k~7 at an approximate Al volume fraction of 0.3 that agreed with analytical predictions if it was assumed that the Al transformed to an oxide *in-situ* and/or after deposition. The significant effect of absorbed water vapour and temperature on PNC dielectric properties was revealed using different types of post-deposition heat treatment.

Alternately-deposited PNCs consisting of Al or Ag 2-20 nm layers sandwiched between nylon-6 layers were fabricated in which the overall PNC Al or Ag volume fraction was controlled by varying the nominal Al or Ag layer thickness. Ag layers comprised of discrete nano-islands that produced a nano-capacitor network effect that increased k to ~11. In the case of Al layers, when the layer thickness was ≥5 nm, corresponding to a nominal volume fraction of 0.1, Al (core)-oxide (shell) nanoparticles were formed and the PNC dielectric constant increased to ~19. The detailed nano-structure of the core-shell particles was studied using various types of transmission electron microscopy (TEM), and the elevations in dielectric constant ascribed to multiple-interface polarisation effects dependent on the formation

of the core-shell structure.

PNCs based on alternate deposition of Ti sandwiched in nylon-6, and then both Ti and Ag in nylon-6 were also fabricated, with k reaching ~73 for Ag+Ti/nylon-6 PNCs. As well as Ti-based core (metal)-shell (oxide) particles, the Ag volume fraction was sufficiently high in the 10 nm nylon-6 layers to again form a nano-capacitor network that contributed to the overall device capacitance and effective dielectric constant. Again, various types of high magnification TEM were critical in resolving the Ti-based core-shell structure and its role in high-k behaviour.

The vacuum-based alternate deposition technique has been developed to offer ease of operation, reliability, flexibility and applicability to chemically different filler and matrix systems in the fabrication of high-k PNC based capacitors, in which high-k performance relies critically on the formation of core (metal)-shell (oxide) particles in both Al and Ti based systems.

Contents

1 Introduction **1**

2 Literature Review **5**

2.1 Principles of electrostatic capacitors 6

2.1.1 Frequency response of permittivity 8

2.2 Types of capacitors 12

2.2.1 Polymer based capacitors 12

2.2.2 Polymer composite based capacitors 13

2.2.3 Polymer nanocomposite based capacitors 14

2.3 Types of fillers 19

2.3.1 Ceramic fillers 19

2.3.2 Conductive fillers 21

2.3.3 Ceramic and conductive fillers 25

2.3.4 Surface modified fillers 28

2.4 Factors influencing energy density 29

2.4.1 Filler size 29

2.4.2 Filler shape 30

2.4.3 Microstructural arrangement and distribution of filler . . . 31

2.4.4 Dielectric breakdown strength 32

2.4.5 Operating temperature 36

2.4.6 The interface in dielectric composites 37

2.5 Processing techniques 39
2.5.1 Vacuum deposition 39
2.5.2 Spraying 40
2.5.3 Spin coating 41
2.5.4 Other techniques 41
2.6 Conclusions 42

3 Experimental **45**
3.1 Fabrication 45
3.1.1 Vacuum deposition 45
3.2 Characterisation 49
3.2.1 Transmission electron microscopy (TEM) 50
3.2.2 Scanning electron microscopy (SEM) 58
3.2.3 X-ray photoelectron spectroscopy (XPS) 58
3.2.4 Impedance spectroscopy 59
3.2.5 Surface Profilometer 59

4 Co-deposition of Al and nylon-6 **60**
4.1 Introduction 60
4.2 Experimental 61
4.2.1 Fabrication 61
4.2.2 Characterisation 63
4.3 Results and discussion 66
4.4 Conclusions 76

5 Alternate deposition of Al or Ag and nylon-6 **78**
5.1 Introduction 78
5.1.1 Alternate deposition technique 80
5.2 Experimental 82
5.2.1 Fabrication 82

5.2.2 Characterisation 83
5.3 Results and discussion 84
5.3.1 The formation of core-shell nanoparticles 91
5.4 Conclusions 99

6 Engineering nanocomposite capacitors consisting of Ti, Ag+Ti and nylon-6 101

6.1 Introduction 101
6.2 Experimental Procedure 103
6.2.1 Fabrication 103
6.3 Results and discussion 104
6.3.1 Effect of adding Ag nanoparticles and the Ti deposition rate 114
6.3.2 Effect of the nylon-6 layer thickness 125
6.4 Conclusions 128

7 Conclusions and Future Work 130

7.1 Conclusions 130
7.2 Future Work 133

References 135

Chapter 1

Introduction

Electrical transport systems require complex electrical sub-systems to condition, manipulate and distribute their electrical power. A critical part of almost all such sub-systems are power capacitors that operate typically at 1 kHz and 500 V, for example in the more electric airframe[1] being adopted by Airbus and Boeing. Figure 1.1 shows a schematic representation of the generation and distribution of power in a conventional aircraft and comprises hydraulic, pneumatic and electrical sub-systems for myriad actuation and control functions. In the particular case of hydraulics that is the dominant actuation technology for high lift surfaces even in the most modern civil airframes, the pumps are situated in the fuselage, distributing power through complex, multiple hydraulic pipes, often with multiple redundancy at ~1.4 MPa in a small aircraft up to ~34.5 MPa in a large transport/civil aircraft[2]. The total weight of all the hardware and the contained hydraulic fluid represents a significant fraction of the total actuation system weight.

The more electric aircraft (MEA) concept involves the replacement of myriad sub-systems for power, actuation and control with a single optimised electrical system for the entire aircraft. At some point, each of the electrical sub-systems requires power conditioning equipment (because every watt of generated power

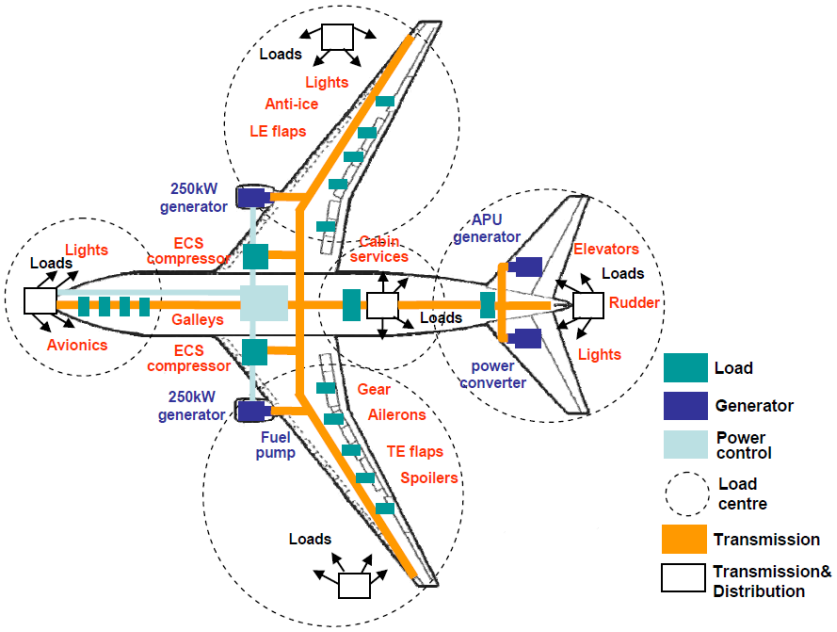


Figure 1.1: Schematic representation of generation and distribution of power in a conventional aircraft.

has to be processed) where it is integrated to the starter/generator of the aircraft's distributed power system.

Power conditioning equipment consists of passive components such as capacitors that filter out unwanted frequencies in order to maintain desirable power quality. Capacitors may account for up to ~30% by weight and ~20% by volume of the power conditioning systems[3].

A fully MEA will have electrical systems that actuate flaps, rudder, ailerons, landing gear and replace the systems that are currently operated hydraulically. This switch from hydraulics to electrical systems is advantageous because: [1] electrical systems are more energy efficient than hydraulics/pneumatics (hydraulics have piping that is more lossy when compared with electrical cabling); [2] currently, hydraulics are kept energised (pressurised) for the entire duration of flight, whereas, electrical systems can be designed to be energised as and when necessary; and [3] electrical systems ensure that the right amount of power is used for the given function[4]. Overall, the aim is to treat the entire airframe as a single electrical system (actuation, avionics, air handling, in-flight entertainment,

etc.) rather than a series of isolated electrical, hydraulic and pneumatic systems. This allows the potential for a "whole system" optimisation of electrical load and generation, and associated energy savings.

Drawbacks of the current capacitor technology

The current capacitor technology of choice in the MEA and other large, more electric transport concepts such as trains for conditioning power, is the electrolytic capacitor that is usually based on a thin Ta-based oxide film mounted on mica or paper, rolled and immersed in a liquid. The electrolytic capacitors provide very high absolute capacitances (of up to several thousand farads, F) but suffer from high mass, high volume and require the use of liquid electrolytes that can neither freeze nor boil during operation. For example, each unit of the Al based electrolytic capacitor assembly shown in Fig. 1.2 weighs ~ 12 kg. Oil-impregnated power capacitors also find application in the resonant circuits of the traction converters in the Siemens high-speed (350 km/h) train[5]. However, these capacitor assemblies are again liquid based systems (operating temperature: -50 to $+70^0$C) and are heavy (weight ~ 56 kg). In the MEA in particular, weight, volume and limited range of temperature for operation places awkward limitations on design flexibility. This situation will only get worse as power requirements for a twin engine aircraft approach 2 MW[6,7].



Figure 1.2: Al based electrolytic capacitor assemblies. Each unit weighs ~ 12 kg.[8]

This thesis investigates the manufacture, microstructure and behaviour of novel polymer-nanocomposite (PNC) based dielectrics for capacitive applications

related to the MEA concept. It is arranged as follows: Chapter 2 reviews the theory behind electrostatic capacitors, the challenges involved in their design and processing, and recent developments in the field of dielectrics; Chapter 3 gives details of the experimental set-up and the characterisation techniques employed to fabricate and study PNCs; Chapter 4 explores vacuum based co-deposition of Al and nylon-6 to fabricate simple parallel plate capacitors whose dielectric properties, chemistry and structure are studied to provide a baseline of understanding; Chapter 5 deals with PNCs fabricated using a modified alternate deposition technique and presents an in-depth study of the dielectric properties in relation to the nano-structure of Al or Ag and nylon-6 based PNCs; Chapter 6 further explores alternate deposition to fabricate Ti, Ag+Ti and nylon-6 based PNCs with relatively high dielectric constant, including studies of the influence of deposition rate and thickness of the deposited layers on the dielectric properties; and finally Chapter 7 presents a summary of the thesis with suggestions for future work. References to all chapters may be found at the end of the thesis.

Chapter 2

Literature Review

This review gives a background of the requirements and challenges for short term energy storage usually provided by capacitors, and familiarises the reader with the basic principles and recent developments in the field of electrostatic capacitors. The various material systems, factors that influence the energy storage capability, and the processing techniques for polymer-nanocomposites (as dielectrics for capacitors) are also reviewed.

Although high dielectric permittivity (high potential for energy storage) fillers play an important role in determining the overall dielectric properties of composite capacitors that are a focus of the experimental work in the thesis, the techniques (mostly chemical) to produce fillers themselves are not reviewed, unless they relate to *in-situ* formation during the processing of the composite. Instead, more emphasis is laid on cost-effective scalable processing techniques for dielectric composites. At the end, a summary of the review is presented.

Polymer based composites for capacitor applications

Polymer capacitors as the "dielectric" in a simple parallel plate configuration are used widely in microelectronic circuits at low voltage and current, across a wide range of frequencies. Polymers are attractive dielectric materials for electrostatic capacitors because they offer low cost, low density and ease of processing

to large area and thin films, with comparatively high breakdown strength of ~ 10^5 kV/m. However, polymers have a low dielectric permittivity of usually 3-5, compared with 10^3 for certain ceramics (such as barium titanate), which limits the absolute capacitances that can be achieved. So, polymers loaded with a minority fraction of fillers that enhance the effective dielectric permittivity of the material between the electrodes are being extensively researched for higher energy density applications, for example, in advanced electronic devices, hybrid electric vehicles and pulse power applications[9].

2.1 Principles of electrostatic capacitors

Electrostatic capacitors are one of the most fundamental devices in electronic circuits and consist of two conductive electrodes separated by an insulator, called the dielectric. A capacitor stores electrical energy in the electric field in the dielectric due to the electrical charges segregated on the conductive electrodes. The ability of a capacitor to store electrical energy is measured by its capacitance. For a parallel-plate capacitor, capacitance C is given by:

$$C = \frac{\epsilon_0 k A}{d} \tag{2.1}$$

where A is the area of the dielectric, k is the dielectric constant (also known as relative permittivity) of the material between the two plates, $\epsilon_0 = 8.854\text{x}10^{-12}$ Fm^{-1} is the permittivity of free space and d is the separation between the plates. Figure 2.1 shows a simple parallel plate capacitor with a dielectric material in between the conductive plates (each plate of area A). The greater the area A, the greater the number of charges that can be stored on each plate. The smaller the distance d between the plates, the better the interaction between the positive and negative charges on the opposite plates. This interaction is important in keeping the charges firmly tethered to the plates, because the greater the number

of charges remaining on plates, then the higher the capacitance. The dielectric constant k can be increased by introducing a dielectric material that has a high intrinsic polarisability. As a result of polarisation, an internal opposing electric field develops in the dielectric which decreases the effective electric field across the capacitor. So, in order to increase the effective electric field across the capacitor to match the applied electric field, more charges have to be stored in the capacitor resulting in enhanced capacitance.

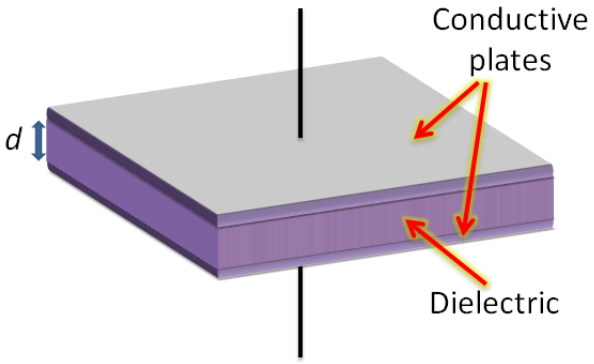


Figure 2.1: A parallel plate capacitor with a dielectric material in between the conductive plates.

The electrical energy E_s stored in a parallel-plate capacitor is given by:

$$E_s = \frac{1}{2}CV^2 \tag{2.2}$$

where V is the potential difference across the plates. The energy stored in a real capacitor is dissipated due to dielectric losses (charge migration resulting in current leakage and molecular vibrations leading to conversion of electrical energy to thermal energy) and resistive losses in electrodes. These losses are accounted for by a term called dissipation factor or loss tangent $tan\ \delta$. The dielectric loss is given by the imaginary part of the permittivity, ϵ''. Permittivity ϵ^*, which is a complex entity, is given by:

$$\epsilon^* = \epsilon' - j\epsilon'' \tag{2.3}$$

where $j = \sqrt{-1}$, ϵ' and ϵ'' are the real and imaginary parts of complex permittivity. The real part of the permittivity ϵ' is equal to $\epsilon_0 k$ which was introduced earlier in Equation 2.1.

The earlier mentioned dissipation factor $tan\ \delta$ is defined as:

$$tan\ \delta = \frac{\epsilon''}{\epsilon'} \tag{2.4}$$

The energy density W of a dielectric capacitor is given by:

$$W = \frac{1}{2} k E^2 \tag{2.5}$$

where E is the electric field strength. From Equation 2.5, it is apparent that by increasing the electric field strength, the energy density of the capacitor can be increased, but the limit is the dielectric breakdown strength of the material E_d. So, maximum energy density W_{max} is attained when E equals E_d.

2.1.1 Frequency response of permittivity

Permittivity is complex in nature because the response of polarisation that occurs in a material under the influence of an external field is not instantaneous. The magnitude and phase difference of this response is accounted for by expressing permittivity as a complex entity. Hence, the dielectric constant of a material is dependent on the frequency of the applied electric field. Various polarisation mechanisms gain dominance at different ranges of frequency as shown in Fig. 2.2(a)[10]. The extent of polarisation that the dielectric undergoes decides the energy density attainable for a particular frequency.

Space charge polarisation, also known as Maxwell-Wagner interfacial polarisation, arises due to moving and piling up of the charge carriers at the interfaces of grains or phases under the influence of an electric field below 1 kHz.

A molecule can be polar or non-polar depending on the distribution of the elec-

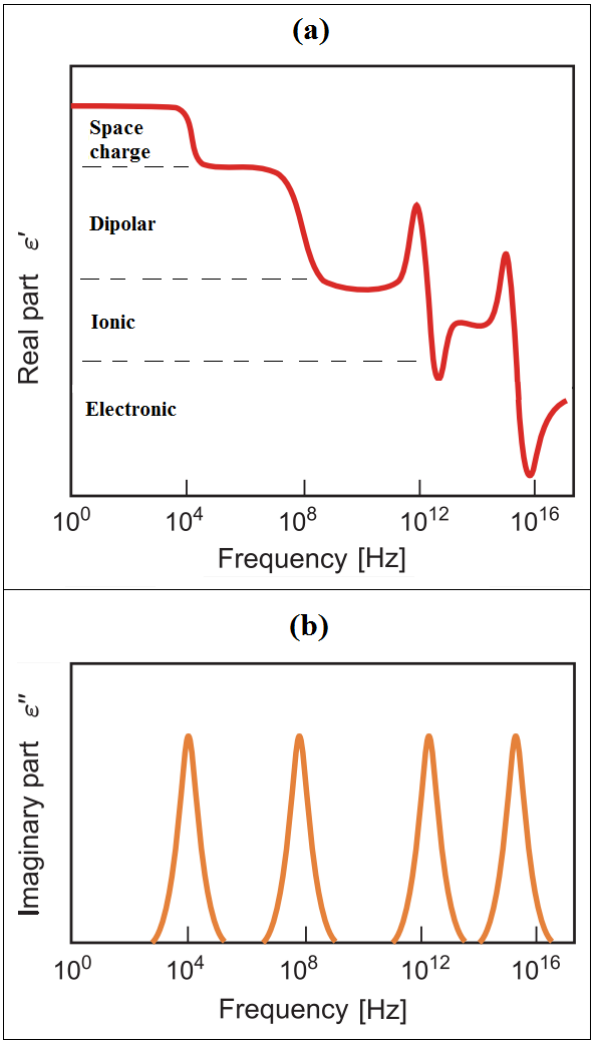


Figure 2.2: Dominance of various polarisation mechanisms at different ranges of frequency[10].

tron cloud between the constituting atoms. This polarity can be permanent or induced. In the absence of an electric field, the dipole moments of molecules are randomly oriented. On the application of an electric field, the dipoles rotate and align themselves in the direction of the applied field giving rise to dipolar polarisation observed in the frequency range 10^3-10^9 Hz. The rotation of dipoles gives rise to dielectric loss due to friction during orientation. This loss can be so significant that it has found practical application in heating food in a microwave oven where the heat is produced due to rotation of permanent dipoles of water molecules (here, the dipoles rotate to keep up with the alternating electric field). When the applied electric field is reversed, the space charge and dipolar polarisation mechanisms also change directions, which involve the movement of space charges and the rotation of dipoles. However, this change is not instantaneous and the time taken is known as the relaxation time. So relaxation effects are seen in space charge and dipolar polarisation mechanisms.

Ionic polarisation, which is dominant in the range 10^{10}-10^{13} Hz, occurs due to the displacement between the positive and negative ions in the presence of an electric field.

Electronic polarisation is caused in neutral atoms due to shift of electron clouds with respect to the nucleus under the influence of an electric field. Electronic polarisation occurs in all dry solids up to 10^{16} Hz, and it is the sole contributor after 10^{14} Hz.

The frequency dependence of ionic and the electronic polarisation mechanisms is governed by resonance phenomena as these are similar to driven damped harmonic oscillators. This leads to peaks at the resonance frequencies of the ionic and electronic polarisation modes as seen in Fig. 2.2(a)[10]. A dip can be seen at frequencies just above the resonance peaks, corresponding to the response of the oscillating system (ionic or electronic) being out of phase with the driving force (applied AC field). A schematic representation of the polarisation mechanisms is

shown in Fig. 2.3[11].

The dielectric loss is especially high in the vicinity of the relaxation or resonance frequencies of the polarisation mechanisms, as seen in Fig. 2.2(b), because the polarisation lags behind the applied electric field, giving rise to an interaction between the field and the dielectric medium's polarisation that results in heating. Apart from these polarisation mechanisms, dielectric loss also depends on a number of other factors such as ambient temperature and humidity (which affect the conductance and polarisation loss in the dielectric), electro-magnetic interference from other operating devices in the vicinity of the capacitor and channel noise during transmission of a monitored signal[12].

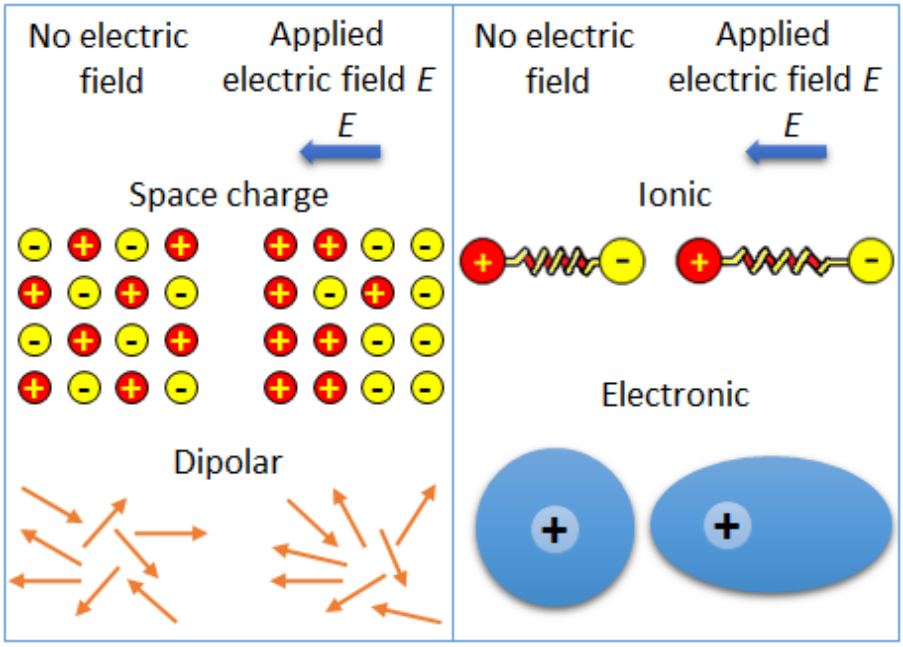


Figure 2.3: Schematic representation of different mechanisms of polarisation[11]. The arrows in dipolar polarisation represent the orientation of the dipole moments.

2.2 Types of capacitors

2.2.1 Polymer based capacitors

High dielectric constant polymers find applications in artificial muscles, actuators and charge storage devices[13] . From Equations 2.1 and 2.5, the main advantages of using polymers for capacitors are:

- easily processed into thin films (low d) with large area (high A)
- high electric breakdown strength E_d

In the initial stages of research in the field of dielectrics, ferroelectric polymers were investigated and the first organic material that was found to have appreciable ferroelectric and piezoelectric properties was poly (vinylidene fluoride) (PVDF). Amongst polymers, PVDF has a relatively high dielectric constant of ~10 and remarkable mechanical and chemical properties[14]. The high dielectric constant is due to the presence of C-F dipoles that re-orientate in the crystalline phase under the influence of an applied electric field[15]. Similar to PVDF, all polymers that have strongly electro-negative groups can spontaneously align in the presence of the electric field, and so possess a comparatively high dielectric constant. However, PVDF and similar polymers are not suitable for *high energy density* capacitors due to their low dielectric permittivities when compared with certain ceramics. PVDF also exhibited relatively high dielectric loss.

The focus on PVDF was then replaced by lower loss polymers such as silicone, benzocyclobutane (BCB), polynorbornene (PNB) and polyimide (PI)[16]. Table 2.1 gives a list of most commonly used polymers in capacitors[17]. Due to their low dielectric permittivities, which are apparent from Table 2.1, none of them can be used in high energy applications, but many are very widely used as cheap and effective lightweight capacitors in mass market mobile electronics such as laptops and mobile phones.

Polymer	Dielectric permittivity
Nonfluorinated aromatic polyimides	3.2-3.6
Fluorinated polyimide	2.6-2.8
Poly(phenyl quinoxaline)	2.8
Poly(arylene ether oxazole)	2.6-2.8
Poly(arylene ether)	2.9
Polyquinoline	2.8
Silsesquioxane	2.8-3.0
Poly(norborene)	2.4
Perfluorocyclobutane polyether	2.4
Fluorinated poly(arylene ether)	2.7
Polynaphthalene	2.2
Poly(tetrafluoroethylene)	1.96
Polystyrene	2.6
Poly(vinylidene fluoride-co-hexafluoropropylene)	~12
Poly(ether ketone ketone)	~3.5

Table 2.1: Dielectric permittivities of commonly used polymers in capacitors[17].

2.2.2 Polymer composite based capacitors

Ceramics offer high dielectric constant (e.g. up to ~100,000 for $La_{1.8}Sr_{0.2}NiO_4$) but have low breakdown strength (~10^4 kV/m). Also, processing of ceramics to manufacture capacitors is difficult, and high dielectric permittivity ceramics are often dense, for example, barium titanate has a density of ~6.08 g/cc, which undermines their specific energy density. Therefore, the basic polymer based composite approach is to add a minority second ceramic phase "filler" with high dielectric constant into the polymer "matrix" to promote polarisability, without undermining the polymer properties. The filler phase should be sufficiently small length scale that significant volume fraction can be incorporated without compromising film thicknesses while avoiding percolation of current "loss"). High filler volume fractions result in a decrease in the breakdown strength, and dielectric constant due to formation of voids[9]. Thus, using polymer composites as dielectrics is an optimised trade-off between high dielectric constant, processability, high breakdown strength and low dielectric loss.

The increase in the dielectric constant of a composite is due to the increase

in the average electric field within the polymer matrix. However, the resulting dielectric medium will have an inhomogeneous internal electric field because of the large difference between the dielectric constants of the constituent phase, concentrating electric field lines at or around microstructured features that can promote localised breakdown, excessive ohmic heating in an oscillating field, and cascade breakdown where local breakdown concentrates the field elsewhere, which leads to breakdown, and so on until the whole film breaks down at lower fields than expected.

The distortion of electric field within the composite is dependent on the filler particle size. As the particle size increases, the probability of distortion also increases, and this effect is significant in micro-sized particles[18] and in systems where small particles agglomerate to form larger particles[17]. Particle aggregates introduce defect centres and again enhance the local electric field, leading to a decrease in the breakdown strength of the composite. So, using nano-sized fillers can be advantageous, providing agglomeration is avoided. Nanoparticles also allow thin films to be used, without excessive percolation.

2.2.3 Polymer nanocomposite based capacitors

Adding nano-sized fillers to polymers increases the dielectric constant of the composite more than micro-sized fillers[19]. Figure 2.4 shows the variation of dielectric constant with aluminium (filler) loading in an epoxy-nanocomposite[20]. At a filler loading of 50%, 100 nm sized Al particles, the epoxy nanocomposites exhibited a dielectric constant of ~60, which is more than twice that of Al-epoxy microcomposites (dielectric constants are ~30 and ~25 for 3 and 10 μm sized Al particles respectively). Here, the Al particles underwent *in-situ* oxidation in the epoxy matrix, more of which will be discussed later.

The high surface area to volume ratio of a nanoparticle provides opportunities to functionalise, which can be exploited to improve the compatibility between

the polymer and the nanoparticle[9] and can also be used to reduce internal fields[18] (and hence high breakdown strength of the resulting nanocomposite). The nano-size of the fillers has also enabled production of thin films with high capacitances[9].

Polymer nanocomposite systems, such as the popular barium titanate[21] and aluminium oxide nanoparticles[20,22] in epoxy-like matrices, have been studied widely for embedded capacitor applications. These so-called embedded passives reduce internal parasitic resistance and inductance associated with surface mounted discreet components[20]. Figure 2.5 shows the dependence of dielectric constant on frequency of barium titanate (BT)-polymer nanocomposite based capacitors[21]. An increase in the volume fraction of BT by two times (from 0.25 to 0.50) resulted in a three times (from 15 to 45) increase in the effective dielectric constant of the nanocomposite.

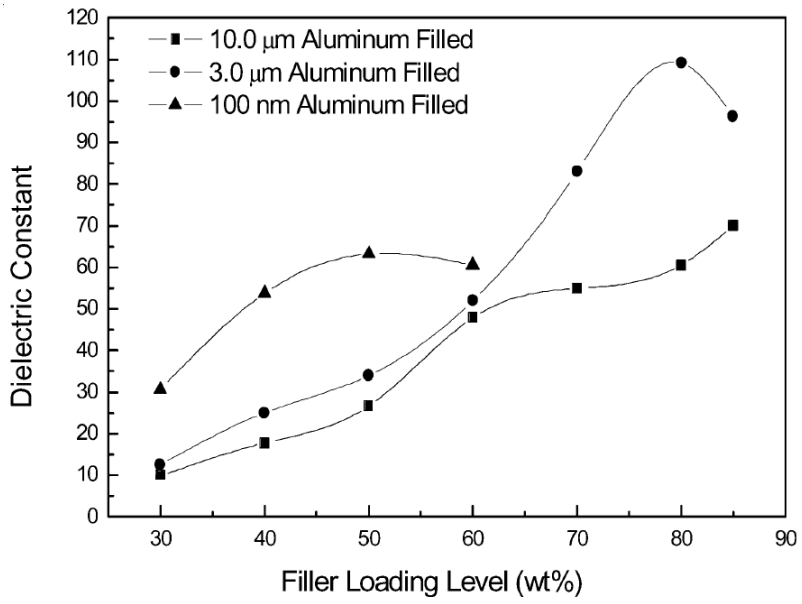


Figure 2.4: Variation of dielectric constant with aluminium (filler) loading in a epoxy-nanocomposite[20]. At filler loading of 50%, 100 nm sized Al particle-epoxy nanocomposites exhibited a dielectric constant of 60, which is more than twice that of Al-epoxy microcomposites (dielectric constants are ~ 30 and ~ 25 for 3 and 10 μm sized Al particles respectively).

Until very recently, few authors have attributed the enhanced dielectric properties

to *interfacial* mechanisms, although as the size of the filler particles reduces to the nanometer scale, the dielectric properties of the interface between the polymer and filler might be expected to play a progressively more important role in the effective dielectric behaviour[23,24]. Nonetheless, the role of the interface is now gaining prominence and it has been suggested, for example, that large interfacial areas that facilitate interface exchange coupling through a dipolar interface layer lead to enhanced polarization at the interface and hence a high drop in the local electric field[25,26], ultimately resulting in an enhanced effective dielectric constant.

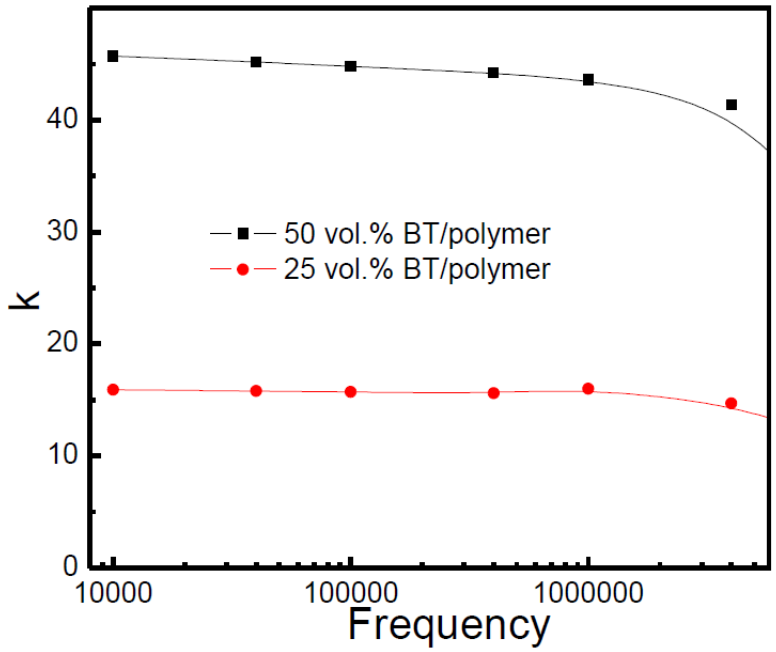


Figure 2.5: The dependence of dielectric constant on frequency of a barium titanate (BT)-polymer nanocomposite based capacitor[21]. An increase in the volume fraction of BT by two times (from 0.25 to 0.50) resulted in a three times (from ~ 15 to ~ 45) increase in the effective dielectric constant of the nanocomposite.

To predict the effective dielectric constant and understand the behaviour of the composite as an effective single medium dielectric, many theoretical models have been proposed. In the simplest model, an increase in effective dielectric permit-

tivity (ϵ_{eff}) is realised by a rule of mixtures approach:

$$\epsilon_{eff} = v_{f_1}\epsilon_1 + v_{f_2}\epsilon_2 \tag{2.6}$$

where the subscripts 1 and 2 represent the two phases, ϵ and v_f represent dielectric constant and volume fraction respectively. Equation 2.6 is also known as Lichtenecker's parallel mixing rule[27], which gives the upper limit of the effective dielectric constant. The ϵ_{eff} can also be estimated by Lichtenecker logarithmic mixing rule:

$$log(\epsilon_{eff}) = v_{f_1}[log(\epsilon_1)] + v_{f_2}[log(\epsilon_2)] \tag{2.7}$$

Equation 2.6 does not predict accurately the effective dielectric constant of all dielectric materials with many experimental results and theoretical approaches disproving the trend in Equation 2.6, especially at low volume fractions of the filler[28–31]. More rigorous models based on mean field theory have been developed. For filler volume fraction in the range 10-50%, Maxwell's equation generally gives a good approximation of the effective dielectric constant[32]:

$$\epsilon_{eff} = \epsilon_1 \left(\frac{\epsilon_1 + 2\epsilon_1 - 2(1 - v_{f_1})(\epsilon_1 - \epsilon_2)}{\epsilon_2 + 2\epsilon_1 + (1 - v_{f_1})(\epsilon_1 - \epsilon_2)} \right) \tag{2.8}$$

Maxwell's equation is applicable to a system consisting of spherical inclusions in a continuous matrix at infinite dilution.

Piezoelectric investigations of PVDF and lead zirconate titanate composites[33] lead to an alternative theoretical approach to the calculation of dielectric constant, which is given by Yamada equation:

$$\epsilon_{eff} = \epsilon_p \left(1 + \frac{n v_{f_c}(\epsilon_c - \epsilon_p)}{n\epsilon_p + (\epsilon_c - \epsilon_p)(1 - v_{f_c})} \right) \tag{2.9}$$

where ϵ_p and ϵ_c are the dielectric constants of polymer and ceramic respectively, n

is a parameter attributed to the shape of ellipsoidal particles and v_{f_c} is the volume fraction of the ceramic. The Yamada equation has become the most widely-fitted equation to experimental data.

Predictions based on effective medium theory are not applicable to *conductive* filler-polymer composite systems where near percolation effects have a significant influence on the dielectric properties. Very high values of ϵ_{eff} ($\sim 10^7$) have been reported just below the critical volume fraction of the minority phase at which significant current percolation occurs. This phenomenon in the vicinity of the percolation threshold follows a power law[34,35]:

$$\epsilon_{eff} \propto \sigma \propto (f_c - f)^{-t} \quad (f < f_c) \tag{2.10}$$

where σ is the AC conductivity, t is a scaling exponent, f is the filler fraction, and f_c is the percolation threshold fraction. When f approaches f_c, the filler particles are on average very close to one another, but remain separated by a thin insulating layer of polymer, thereby forming a micro-capacitor network[35], resulting in very high dielectric permittivities. The formation of the micro-capacitor network is discussed in detail in section 2.3.2. Figure 2.6 shows the effective dielectric constant of the Ag-PVDF nanocomposites as a function of Ag volume fraction at 1 kHz and room temperature (inset shows a plot of log k vs. volume fraction of Ag)[36]. Here, the dielectric constant increased dramatically to 110 with an Ag loading of 17.5% due to near-percolation threshold effect. Ag-PVDF is a classic example of a metal-polymer nanocomposite system, where percolation theory is applicable.

Although such a high dielectric constant appears attractive, losses also dramatically increase near the percolation threshold. Further, because the increase in dielectric constant is often strongly non-linear, see Equation 2.10, in practice the manufacture of these films at an industrial scale is highly problematical: too little filler and there is barely an increase in dielectric behaviour, slightly too much

and the capacitor is highly lossy, leaks excessive currents and may breakdown completely.

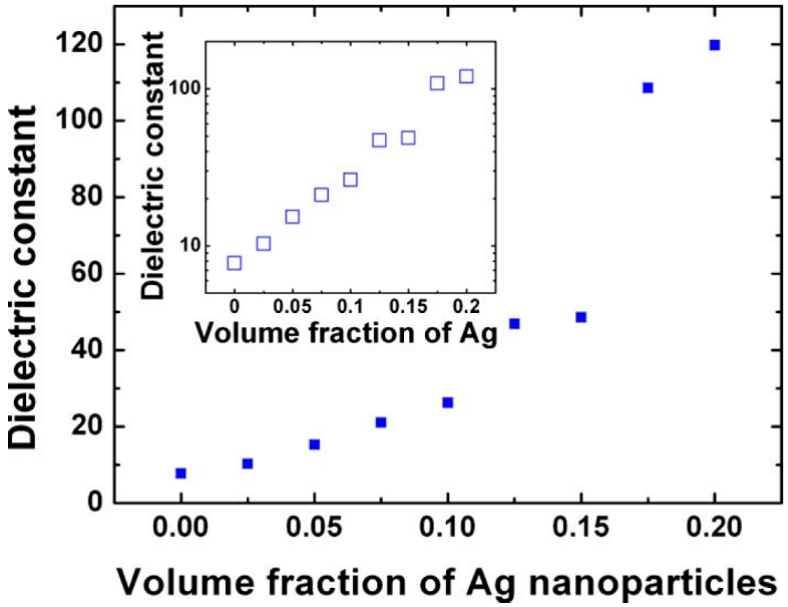


Figure 2.6: Effective dielectric constant of nanocomposite Ag-PVDF as a function of Ag volume fraction (at 1 kHz and room temperature). Inset: A plot of log k vs. Ag volume fraction[36].

2.3 Types of fillers

2.3.1 Ceramic fillers

Generally, ceramics have very high dielectric constant, especially those with perovskite crystal structure that exhibit extraordinary dielectric properties of many thousands depending on temperature. Table 2.2 gives the dielectric constants of commonly used ceramics for capacitors[17].

Barium titanate (BT) is the most widely investigated oxide in the field of dielectrics. BT was recognised as a ferroelectric compound in the mid 20th century and since then it has attracted the attention of researchers as a dielectric material. Figure 2.7 shows the perovskite crystal structure of BT, with Ba^{2+} ion in the centre (green) and corner-sharing octahedral TiO_6 in blue[17]. The formation of

Composition	Dielectric permittivity
$BaTiO_3$	1,700
PMN-PT (65/35)	3,640
$PbNb_2O_6$	225
PLZT (7/60/40)	2,590
SiO_2	3.9
Al_2O_3	9
Ta_2O_5	22
TiO_2	80
$SrTiO_3$	2,000
ZrO_2	25
HfO_2	25
$HfSiO_4$	11
La_2O_3	30
Y_2O_3	15
$\alpha - LaAlO_3$	30
$CaCu_3Ti_4O_{12}$	~60,000
$La_{1.8}Sr_{0.2}NiO_4$	~100,000

Table 2.2: Dielectric permittivities of commonly used ceramics in capacitors[17](room temperature properties). PMN-PT (65/35) is the abbreviation for 65% lead magnesium niobate and 35% lead titanate. PLZT (7/60/40) is the abbreviation for lead lanthanum zirconium titanate.

electric dipoles due to structural change involving relative displacement of Ba^{2+} and Ti^{4+} cations with respect to the O^{2-} ions gives rise to the impressive dielectric properties of BT. The peak value of dielectric constant of BT is over 12,000 at the Curie temperature of 132^0C. Such high value of dielectric constant has made BT a promising dielectric.

In terms of composite materials, agglomeration of BT particles has been of particular concern, especially in simple solution processed composites. Agglomeration results in poor film quality and inhomogenity. To facilitate dispersion of BT particles in a polymer matrix, surfactants such as phosphate esters and oligomers have been tried[37,38]. However, residual free surfactants have been reported to increase the leakage current and make the capacitors lossy[39].

The dielectric properties of BT are dependent on grain size[40–42]. At room temperature, the dielectric constant of BT particles is in the range of 1500-2000 for

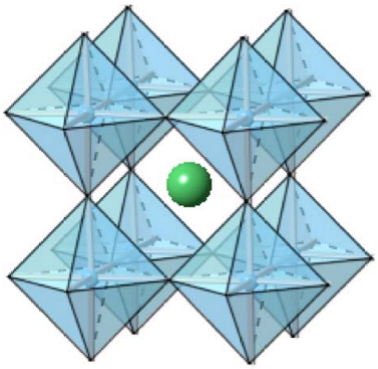


Figure 2.7: Perovskite crystal structure of barium titanate, with Ba^{2+} ion in the centre (green) and corner-sharing octahedral TiO_6 in blue[17].

coarse grained structure (grain size ~ 10 μm) and 3500-6000 for fine grained structure (grain size ~ 1 μm). This dependence on grain size has been attributed to the higher internal stresses (and hence higher dielectric constant) in fine grains as compared with coarse grains of BT[43]. So, carefully engineering the microstructure of the BT particles can produce composites that have varying dielectric constant for the same filler fraction. This is a very important aspect since variation of filler fraction influences the thermo-mechanical properties of the composite film.

Many other ceramics such as lead magnesium niobate-lead titanate (PMN-PT)[44], $CaCu_3Ti_4O_{12}$ (CCTO)[45], strontium titanate ($SrTiO_3$)[46], Li_2MgSiO_4 (LMS)[47] and titania (TiO_2)[48] have also been tried as fillers in polymers to obtain high energy density capacitors, and all contribute to enhanced performance, which can be best fitted to one of the expressions in Equations 2.6 to 2.9.

2.3.2 Conductive fillers

Conductive filler-polymer composites can have very high dielectric constant at very low volume fraction of filler. The effective dielectric constant of composites with conductive fillers follows the power law in Equation 2.10 and enhancement is due to the micro-capacitor network effect.

Formation of the micro-capacitor network

Figure 2.8 shows the effective dielectric constant of PVDF based nanocomposites as a function of exfoliated graphite nanoplates (xGnPs) filler volume fraction, measured at 1 kHz and room temperature[49]. The variation in the microstructure of the nanocomposite film at f <0.75, 0.75-2.25 and >2.25 is shown in the schematics in Figs. 2.9 (a), (b) and (c) respectively.

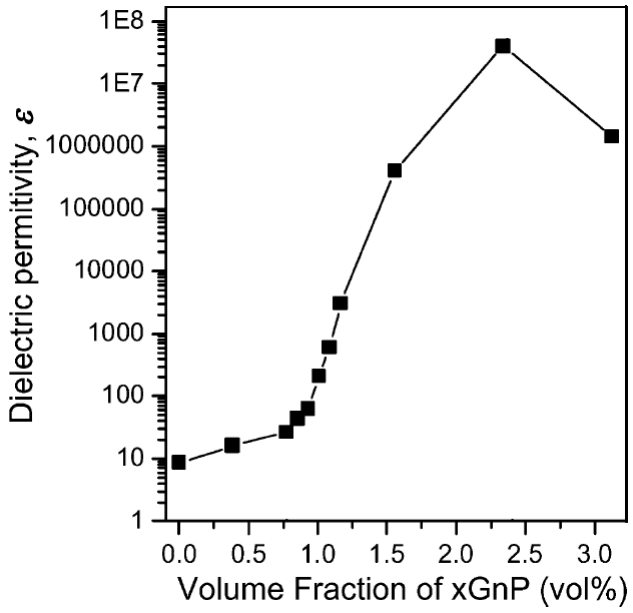


Figure 2.8: Effective dielectric constant of PVDF based nanocomposites as a function of exfoliated graphite nanoplates (xGnPs) filler volume fraction, measured at 1 kHz and room temperature[49].

In Fig. 2.9 (a), when the filler volume fraction f was <0.75, the fillers were relatively too far from each other to form an electrically conductive network. So the nanocomposite film remained largely insulating. When the f was in the range 0.75-2.25, the fillers were separated by a very thin layer of polymer, as shown in Fig. 2.9 (b), but were still not sufficiently close to form a percolative network. The nanocomposite is then considered to be a near-percolating medium in which two adjacent conductive fillers separated by a thin dielectric layer of thickness d' can be thought of as two electrodes of a miniature capacitor. Such a miniature capacitor has a relatively high capacitance due to the ultra-thin nature of the

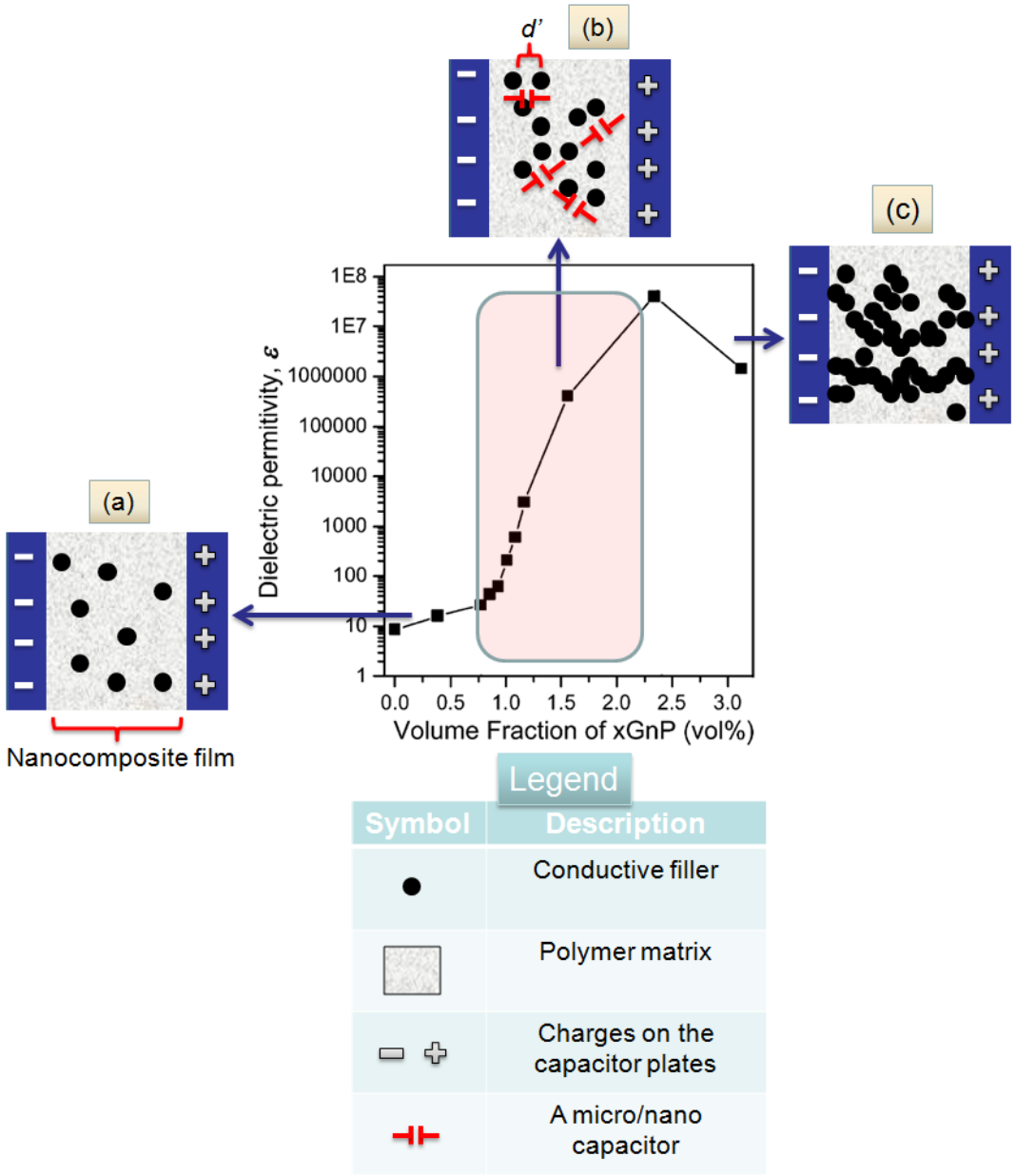


Figure 2.9: Effective dielectric constant of PVDF based nanocomposites as a function of exfoliated graphite nanoplates (xGnPs) filler volume fraction, measured at 1 kHz and room temperature[49]. The variation in the microstructure of the nanocomposite film at filler volume fraction f <0.75, 0.75-2.25 and >2.25 is shown in the schematics (a), (b) and (c) respectively.

dielectric film between the fillers. A number of such miniature capacitors in random series and parallel combinations formed a high-k micro-/nano-capacitor network that lead to an enhancement in the overall k of the nanocomposite film. At f>2.25, the filler fraction was sufficiently high to form a continuous percolating network throughout the film, as shown in Fig. 2.9 (c), resulting in a relatively low-k nanocomposite film.

Conducting carbon fillers (carbon black, graphite nanoplates, carbon nanotubes), metallic fillers (Ni, Ag, Mo) and non-metallic conductive polymer particles (for example, polyaniline) and have all been used as fillers in such conductor-insulator composites[35,36,49–56]. The enhancement in dielectric constant is most marked for one-dimensional fillers such as carbon nanotubes (CNTs) and two-dimensional exfoliated graphite nanoplates with an increase of ~ 10^4 times and ~ 10^7 in dielectric permittivity respectively, as shown in Figs. 2.10[56] and 2.8[49].

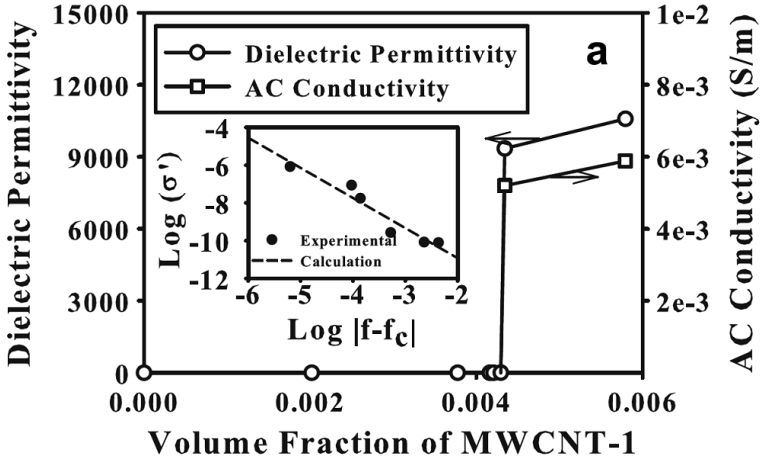


Figure 2.10: The dependence of dielectric permittivity and AC conductivity of perfluoro alkoxy (PFA)/multiwalled carbon nanotube (MWCNT) films on the volume fractions of MWCNTs at 10 kHz and 25^{0}C[56]. The inset shows the best-fit of AC conductivity to Equation 2.10.

In these composites, unlike composites containing ceramics, an increase in filler fraction does not always ensure a corresponding increase in dielectric constant, and beyond the percolation threshold, the composite becomes conductive as seen in Fig. 2.9. The main disadvantages of using a conductive filler is the control of

the volume fraction at close to the critical point during large-scale production, and near-percolating composite films tend to suffer from unusable high loss, especially at low frequencies (<10 kHz)[56]. Moreover, operational parameters such as temperature can bring about microstructural changes that can alter the inter-particle spacing and "convert" these dielectrics into "lossy" *conducting* materials.

2.3.3 Ceramic and conductive fillers

A polymer film can be incorporated with two different types of ceramic/conductive fillers at the same time: [1] core-shell particles, where the ceramic and conductive phases are closely associated with each other; and [2] two distinct ceramic and conductive phases.

Core-shell particles

Core-shell particles with metallic cores and ceramic shells can enhance the dielectric constant of composite films[16,57]. The shell can be an oxide of the metal constituting the core or an oxide of another metal (cobalt particles coated with zinc oxide were used as core-shell fillers in PVDF to enhance the dielectric constant to 51 at 100 Hz and 10% filler loading[57]). In the case of composite films with Al filler particles, post-deposition reaction of isolated Al regions may lead to the formation of core-shell particles, with Al as the core with an Al_2O_3 shell[20,22]. Figure 2.11 is a high resolution TEM micrograph of a 100 nm aluminium particle with Al_2O_3 shell of thickness 2.8 nm[16,22,58]. Composites containing 80 wt% Al-Al_2O_3 core-shell particles have shown high dielectric constant of 109 and low dissipation factor of ~ 0.02[59]. This dielectric constant was ~ 30 times higher than the dielectric constant of the epoxy. The enhanced dielectric performance of these composites could not be explained by effective medium theory models because the effective dielectric constant of the composite was more than dielectric constant of the constituent phases.

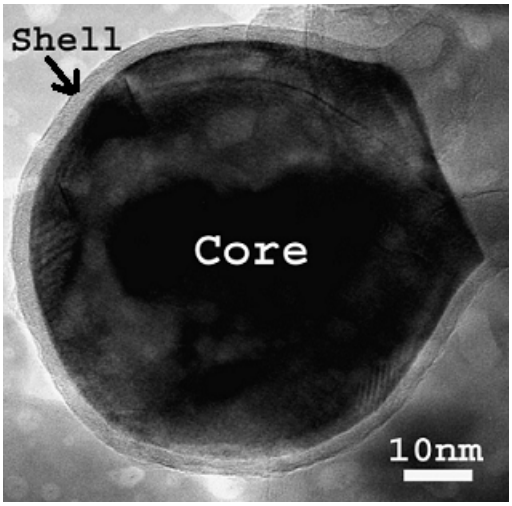


Figure 2.11: High resolution TEM micrograph of a 100 nm aluminium particle with Al_2O_3 shell of thickness 2.8 nm[16,22,58].

This "anomalous" increase in dielectric constant was attributed to near-percolation effect and interfacial polarisation due to spatial or space charges (electrons) that tunnel out from the metallic Al-core to the Al_2O_3-shell. However, the composite containing Al (core)-Al_2O_3 (shell) particles was not a typical percolative system due to the absence of a percolation threshold. The presence of an insulating oxide-shell around the conductive Al-core prevented the formation of a percolative network, and hence the dielectric constant of the composites steadily increased with the filler loading.

The authors in[58] do not provide a detailed explanation of the polarisation mechanism and the physical phenomena occurring in the vicinity of the core-shell particles, but it can be implied that the role played by the tunnelling process in enhancing polarisation is by contributing spatial charges that might migrate and accumulate at the interfaces of dielectrically different phases, such as oxide/polymer interfaces, in the composite arrangements of particles and matrix. This build-up of charges at heterogeneous interfaces leads to the so-called interfacial polarisation resulting in an elevation of the overall or effective dielectric response of the composite. Interfacial polarisation has also been reported elsewhere[60] in Al (core) - Al_2O_3 (shell) particles and again the enhancement of the

dielectric properties was suggested to be due to the motion of the free charges both in the core and oxide layer, but the underlying physics was not discussed in detail and is generally lacking from the literature. An in-depth study of the structure and chemistry of core-shell particles on a nano-scale together with systematic measurements of dielectric response might provide an insight into the physical processes governing the "super-k" behaviour in composites containing core-shell particles.

Returning to the aspect of space charge and tunnelling effects, researchers in the mid-twentieth century showed that electron tunnelling through 3-5 nm thick layers of Al_2O_3 was possible[61,62], because the wave function of a free electron ψ_e in the metal (here Al) remains finite across the thickness of the insulator (here Al_2O_3), yielding a measurable probability of electron passage from one side of the insulator to the other[63]. These reports on electron tunnelling stress the importance of the thickness of the oxide-shell. If the shell is too thick (tens of nm), electron tunnelling is suppressed and the core-shell particles contributions to dielectric enhancement is limited. It is important to note that the effect of defect energy levels that might be present in the oxide was not considered in this qualitative description, because chemistry and structural variations within the oxide shell were not considered.

There has also been an on-going debate[64–68] on the time-scale involved in the tunnelling process based on experimental investigations and theoretical predictions that has not yet arrived at a definitive conclusion. However, the near-instantaneous nature of tunnelling rules out the possibility of any considerable phase difference between the tunnelling current and the applied electric field. Nevertheless, under the influence of an AC field, the physical processes involving migration, accumulation and reordering of the charged species at interfaces, that might "trap" charges, might result in a phase-shift and make them capacitive in nature.

The development of an out-of-phase dipole moment at the interfaces, particularly at the poles of the particles in nanocomposite films, due to the accumulation of charges at relatively low frequencies, has been suggested to be responsible for an enhancement in the dielectric properties beyond the predictions of Maxwell-Wagner theory[69,70]. So core-shell particles, which inherently have multiple interfaces, might create a conducive environment for enhanced interfacial polarisation.

Distinct ceramic and conductive particles

Composite systems consisting of both ceramic and conductive filler particles can exhibit an increase in dielectric constant by superimposing the effects of polarised ceramics and a microcapacitor network of conductive fillers. Again, $BaTiO_3$ is the most used ceramic in combination with Al[71], Ag[72,73], Ni[74] and carbon fibre[75]. These systems, although believed to show near-percolative effects have so far not exhibited enhancement in dielectric properties beyond those already reported conductive filler-polymer composites and their distinct benefits (if any) have not been demonstrated.

2.3.4 Surface modified fillers

Surface functionalisation has been proved to improve the mechanical flexibility of composite films, compatibility between filler and matrix, and also has resulted in better dispersion of nanofillers in the matrix leading to enhanced energy storage[25,48,57,76–78]. Coating metal particles with organic dielectrics which form an insulating high dielectric constant shell has also been used as a technique to enhance the dielectric properties of composites[55]. Such core-shell particles showed percolative-like enhancement in dielectric constant (k increased by an impressive two orders of magnitude). By modifying the surface of BT nanoparticles using phosphonic acid groups, aggregation of particles has been reduced[77]. In this case, the dielectric constant was increased, but the breakdown strength de-

creased. In contrast, introduction of surface modified titanium dioxide nanoparticles into low density polyethylene (LDPE) increased the breakdown strength by 40% as compared with composites made up of untreated titanium dioxide nanoparticles[18]. A polar silane coupling agent N-(2-aminoethyl) 3-aminopropyltrimethoxysilane (AEAPS) was used for surface modification of the titanium dioxide nanoparticles. The polar groups in the AEAPS decreased charge trapping in the deep traps of the insulating material at the nanoparticle surface, and these variations improved the dielectric breakdown strength. However, the breakdown strength of the nanocomposite was still lower than pure LDPE. Surface modification also had a negative influence by leading to agglomeration and formation of a mechanically weak interface. Surface modification did strongly affect the percolation threshold, which increased by ~ 25% when compared with untreated Al nanoparticles in systems such as polyethylene/aluminium[79]. So, surface modification of fillers can have contrasting effects on the dielectric properties of the composites and it is highly dependent on the specific nature of modification, the host filler and the matrix.

2.4 Factors influencing energy density

2.4.1 Filler size

London-van der Waals forces are high at the nanoscale as these forces are inversely proportional to the sixth power of the particle radius. So, nanoparticles have a great tendency to aggregate and form clusters[36,80]. At high filler volume fraction, the particle size limits the minimum thickness of the film, as the film will have the roughness of at least the particle size. This dictates the production of thicker films with lower capacitances.

For a given filler fraction, bimodal nanocomposites (with two different filler particle sizes) have been shown to have higher capacitances than unimodal nanocom-

posites[21,81]. Figure 2.12 shows the variation of capacitance with frequency of BT-epoxy bimodal and unimodal nanocomposites for the same thickness (7 μm) capacitors at a BT volume fraction of 0.6[81]. At 1 kHz, the capacitance of bimodal nanocomposite was much higher (~1000 pF) than the unimodal nanocomposites (~300 pF and ~400 pF for 1000 nm and 200 nm sized BT particles respectively) because the high packing efficiency (the small particles filled up the voids in between large particles) and increased particle surface coverage in the case of bimodal nanocomposites.

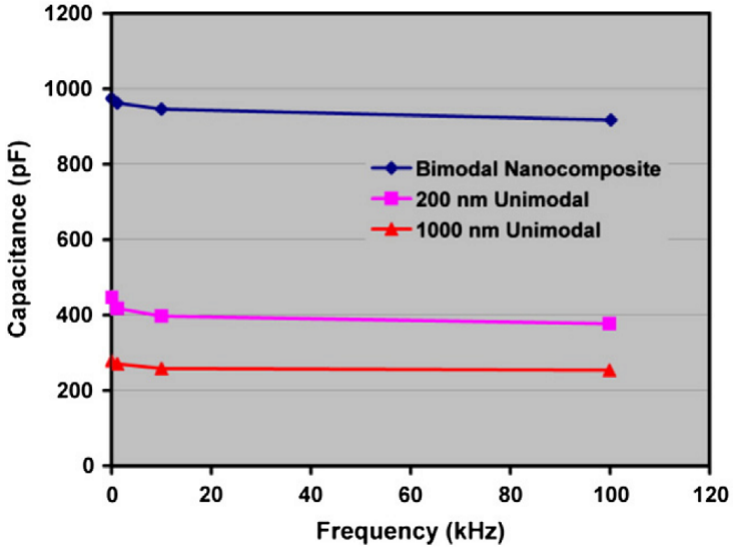


Figure 2.12: Variation of capacitance with frequency of BT-epoxy bimodal and unimodal nanocomposites for the same thickness (7 μm) capacitors at BT volume fraction of 0.6[81].

2.4.2 Filler shape

The effect of filler shape should be considered seriously when the particle aspect ratio deviates by more than an order of magnitude from that of a sphere[82]. Such non-spherical particles can establish conducting paths easily, leading to a low percolation threshold[83], and as previously described these composites can exhibit high dielectric constant (due to near-percolation effects) at low filler fractions. In the presence of an external electric field of 15 kV/mm and a filler volume fraction

of 50%, high aspect ratio lead zirconate titanate (PZT) nanowires showed an increase in energy density of 78% over low aspect ratio PZT nanorods[9]. Observance of such effects has lead to extensive studies on modelling the influence of particle shape on dielectric permittivity by many research groups[82–85]. In one particular study, the strong mutual interaction between the edges and corners of symmetric angular shapes (like cubes and square cylinders) has been proposed to result in very low polarisation per unit volume[84]. This interaction was not significant between circular cylinders and spheres and hence these had high dipole moments leading to high dielectric constant.

2.4.3 Microstructural arrangement and distribution of filler

The dielectric constant is also dependent on the spatial arrangement and any directional alignment of the fillers. Recent computational approaches to analyse these dependences have produced results typified in Figs. 2.13 and 2.14[86]. The relationship between filler microstructure and effective properties of dielectric composites were studied by employing a phase field dielectric composite model[86,87], which solved electrostatic and magnetostatic equations in terms of a polarisation vector field in reciprocal Fourier space. The versatility of this model was showcased by the authors by formulating it for dielectric and magnetic composites[87] containing single phase[86] and multi-phase fillers (core-shell particles)[88]. In dielectric composites, the dielectric constant was determined by calculating heterogeneous distribution of polarisation, local electric field and charge density[86].

The results obtained from this model are presented in terms of dielectric susceptibility instead of dielectric constant for convenience, where dielectric constant k is related to dielectric susceptibility χ by $k = 1 + \chi$. From Figs. 2.13 and 2.14, composites with closely arranged filler particle microstructure and high aspect ratio particles aligned (long axis) in the direction of applied field exhibited the

highest dielectric constant. However, predictions from this type of theoretical model and simulation have yet to be compared with experimental data systematically, in part owing to the lack of a manufacturing process that can produce such tightly controlled microstructures of low dispersivity. Such comparison and verification will throw light on the accuracy of the approach and could identify to which real systems the approach is applicable. These "geometric" arrangements also tend to only show significant elevations in dielectric constant over relatively narrow frequency widths.

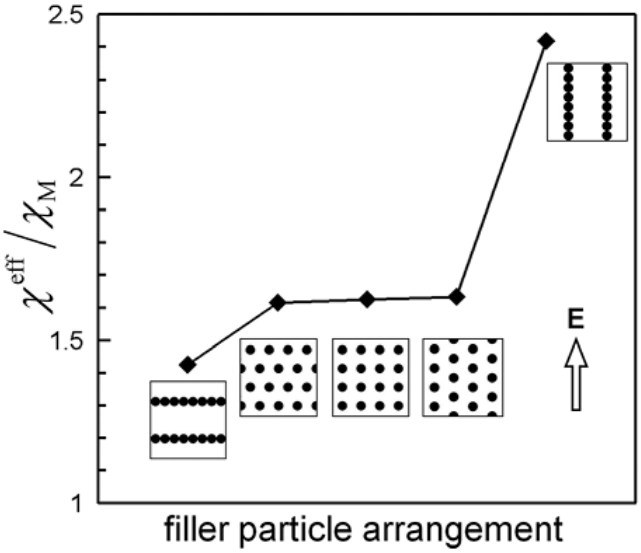


Figure 2.13: Effect of filler particle microstructural arrangement on effective composite susceptibility in composites composed of 20% volume fraction of circular fillers with dielectric susceptibility $\chi_F/\chi_M = 10$. Insets illustrate the corresponding particle arrangements. Arrow indicates electric field E direction. χ_{eff} is the dielectric susceptibility component in the E direction, χ_F and χ_M are the dielectric susceptibility of filler and matrix respectively[86].

2.4.4 Dielectric breakdown strength

Polymers are excellent insulators because the band gap between valence and conduction bands is >2 eV[89] and is typically about 7 eV[90]. Table 2.3 shows the band gap energies of some polymers[91,92]. Due to the high band gap energies, the electric fields need to be > 10^7 kV/m for tunnelling of electrons from the

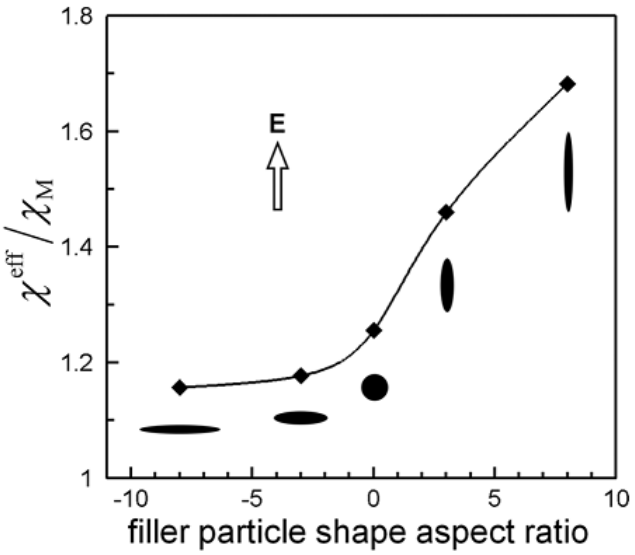


Figure 2.14: Effect of filler particle shape and orientation on effective composite susceptibility in composites composed of 8.7% volume fraction of fillers with dielectric susceptibility $\chi_F/\chi_M = 10$. Insets illustrate the corresponding particle shapes and orientations. Shape aspect ratio is defined as R_{long}/R_{short} -1, where R_{long} and R_{short} are the radii along long and short axes of the particle, respectively. The sign indicates particle orientation with long axis parallel (+) or perpendicular (-) to electric field E direction as indicated by arrow. χ_{eff} is the susceptibility component in E direction[86].

valence to the conduction band, which might lead to breakdown of the polymer. However, polymers are known to breakdown at a relatively lower field of ~ 10^5 kV/m by other mechanisms.

Polymer	**Band gap energy (eV)**
Polypropylene	7
Polyethylene	6.9
Polyamide-6 (Nylon-6)	4.9
Polystyrene	4.4

Table 2.3: Band gap energies of some polymers[91,92].

Avalanche breakdown (also known as ionisation breakdown) is characterised by conduction and multiplication of a large number of electrons (and other charge carriers) resulting from multiple high energy collisions between the electrons in the polymer matrix. This multiplication of electrons occurs when free electrons in polymers acquire sufficient kinetic energy by accelerating (under the influence of an external field) along the mean free path and knock out other electrons. Polymers are good hosts for this mechanism to take place because they often contain regions of amorphous phases. These amorphous phases have unoccupied volume consisting of voids/cavities which are filled with gases of dielectric strength ~ 10^3 kV/m. The differences between the dielectric properties of the polymer and the gases in the voids, and a number of other factors (such as gas pressure, void size and shape) might lead to a local intensification of field resulting in an additional breakdown within the void. Since such breakdown occurs only inside the void and not necessarily in the whole polymer, such a breakdown is known as partial discharge breakdown, which can be supported by relatively large voids of dimensions ~ μm. The electrons that are generated by breakdown are accelerated along the length of the void and they might gain sufficient energy to knock off more electrons on the other side of the void and erode the matrix. The distribution of such voids throughout the matrix might lead to the overall breakdown of the polymer.

In relatively small voids of molecular order, which are referred to as holes by Artbauer[93], the void size is not sufficient to support partial discharge breakdown because the voltage appearing across the voids is not sufficient to cause breakdown. However, these holes provide longer mean-free paths than the polymer for the *free electrons* (not the electrons produced by ionisation because the breakdown has not occurred yet) to accelerate and gain sufficient energy to *initiate* breakdown[17,93].

A simple solution to the problem caused by the voids (in decreasing the breakdown strength of polymers) is to fill them up, preferably with non-conducting material. Various chemical and physical modifications have been suggested to improve the breakdown strength. When the voids of poly (ethylene terephthalate) (PET) were filled with non-conductive polyaniline (PANI), the dielectric breakdown strength increased by 30%[94].

Polyethylene (PE) blends consisting of linear and branched chains have shown higher breakdown strength than linear PE[95]. This improvement in breakdown strength was attributed to the network of thick lamellae structure that altered local charge transport processes. Impregnation with rape-seed oil into polypropylene (PP) films has resulted in 25% enhancement of breakdown strength[96].

In polymers which have short free mean paths, conductive paths are formed as a result of polymer degeneration. Since the life of a polymer decreases exponentially with the applied electric field, the formation of conducting channels depends on the intensity and duration of the external applied field[97]. Also, high electric fields can ionise molecules due to tunnelling of electrons through a reduced potential barrier. Due to this ionising effect, the electric field intensity at which ionisation of macromolecules starts can be considered as the theoretical maximum breakdown strength of polymers. Localised high electric fields can form in a polymer due to structural differences and defects. These local fields can also lead to degeneration of polymer. Degeneration leading to premature dielectric

breakdown not only limits the energy storage capability of the capacitor, but also makes the capacitor less reliable.

2.4.5 Operating temperature

The degradation temperature of polymer matrices limits the temperature at which the capacitors can be used. Also, the mismatch between the coefficients of thermal expansion of the passive components in an embedded system may lead to delamination and system failure[16]. So, choosing the right materials for the components gains importance at variable operating temperature (such as expected in more electric aircraft). Incorporation of nanoparticles generally increases the crystallization temperature of the polymer[25]. A 5% addition of $BaTiO_3$ increased the crystallization temperature of poly (vinylidene fluoride-ter-trifluoroethylene-ter-chlorotrifluoroethylene) from ~100 to ~ 106^0 C. The presence of crystalline phases can enhance charge transport due to the more ordered structure. In a crystalline polymer, fillers preferentially occupy the non-crystalline spaces (boundaries) and this can form a continuous network that facilitates charge transport (and thus make the capacitor lossy).

In a composite, the dielectric constant generally increases with temperature in the range of 25-150^0 C. This increase can be due to an increase in the mobility of polymer chains, any increase in the permittivity of the filler (in the case of semiconducting fillers) and enhanced charge carrier diffusion with temperature[48,56,98,99]. However, this increase is not always useful or significant: for example, in the temperature range of 25-150^0 C, the dielectric constant of polymerised tripropylene glycol diacrylate-30 volume % $BaTiO_3$ films increased from 39 to 45[98] and in composites containing 40 volume % zinc oxide (ZnO) fillers in low density polyethylene, there was a slight increase in dielectric permittivity from ~5 at 20^0C to ~7.5 at 100^0C[99].

A change in temperature can also lead to changes in the allotropic forms of the

ceramic filler. If this change is exhibited in bulk properties, then the dielectric constant of the whole composite can be altered. For example, $BaTiO_3$ changes its crystal structure from cubic to tetragonal at the Curie temperature of 132^0C[100] and this results in a rapid and progressive decrease in dielectric constant.
The study of variation in dielectric constant at high temperatures is quite important in the context of industrial applications because capacitors that have relatively stable dielectric constant can be placed much closer to other heat generating components such as generators or combustors, and such capacitors require less thermal-proof packaging.

2.4.6 The interface in dielectric composites

The interface between the polymer and the filler might sometimes usefully be considered as a separate phase - an "interphase" - especially where a reaction between filler and matrix, or of the filler, has occurred. Similarly an interphase might be expected where significant surface modification of the filler has been used. The idea of this interphase has been developed to try and help understand the dielectric behaviour of these types of composite systems. For example, the interphase power-law (IPL) model[101] predicts the effective dielectric constant of a composite by taking into consideration the dielectric constant and volume fraction of the interphase. This model suggested that deviations from standard mixture models in experiment may be due to the interphase, such as enhanced molecular polarisability at the interface due to the formation of interfacial dipoles[102].
Interfacial polarisation, often referred to as Maxwell-Wagner-Sillars polarisation (MWS)[103,104] takes place due to the charges[105] that move and pile up at the interfaces in heterogeneous materials. Charge accumulation and separation might also take place at the interfaces due to "trapping" of charges that originate by thermionic emission from metallic fillers/electrode and by quantum mechanical tunnelling of charge carriers above an applied threshold electrical field[106].

Defect-rich interfaces have been found to enhance charge trapping around metallic core-oxide shell particles[107].

These interfacial effects can be expected to become more significant in the case of nanocomposites than composite systems with micron-sized fillers but the field is still somewhat in its infancy, mainly due to problems in accurate characterisation of interfaces in these materials at the nanoscale.

The interface between the dielectric material and the electrode (current collector) can also influence the effective device dielectric properties. This influence has been seen as an increase in the permittivity and dissipation factor of the capacitor due to free charge build up at the interface[108]. Enhanced dielectric constant and dissipation factor have also been observed in epoxy-silica composites due to interface mechanisms and ionic conductivity by contaminants[19]. Water is one such contaminant that fills up voids along interfaces and sometimes forms a "water-shell" around the nanoparticles[109]. When nanoparticles are in close proximity, these water-shells overlap and allow charge-carrier movement in between them as shown in the Fig. 2.15[109]. Since water has polar molecules (H_2O), the presence of water in nanocomposites increases both dielectric constant and dielectric loss.

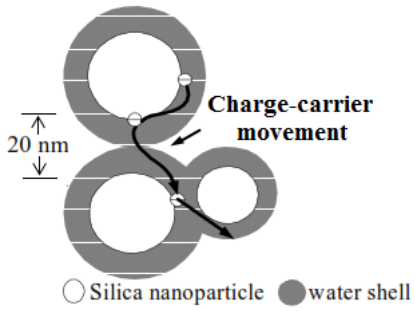


Figure 2.15: Schematic of charge-carrier movement in between nanoparticles through water-shells[109].

2.5 Processing techniques

2.5.1 Vacuum deposition

Vacuum deposition is a well-known and widely used economic technique to produce polymer films and monolithic layers of metals. Vacuum deposition can be readily carried out on the laboratory scale, as well as in industrial scale roll-to-roll coaters[110–119]. Thermal vacuum deposition involves evaporation of the material (by heating) and its subsequent deposition (condensation) on a cold substrate in vacuum. In the case of preparing polymer nanocomposites, the polymer and the minority phase (for example a metal) are simultaneously heated to form two vapours. Mixing of vapours takes place and the intention is that the film condensate is a composite. Polymers such as poly(vinylidene fluoride) (PVDF), poly(p-phenylene), poly(methyl methacrylate) (PMMA), Teflon AF 1600 and nylon-6[110–112] have been studied previously for their applicability to vacuum deposition. Co-evaporation of two or more monomers[120] has also been studied to obtain more complex co-polymer films.

Effect of deposition rate

Low temperatures in the chamber during evaporation facilitate low deposition rate of metal. Under such conditions, vaporized metal atoms and small metal clusters have greater probability of encountering each other to form large nanoparticles before deposition[121]. Low temperature is also not favourable for random diffusion of nanoparticles in the polymer.

While fabricating a composite material, if the rate of evaporation of a polymer is increased to try to approach those of metals, then the tendency of "spitting" of polymer increases leading to formation of non-uniform films[122]. During evaporation, the scission of polymer chain can occur randomly or can follow an orderly depolymerisation mechanism depending on the nature of the polymer. Increas-

ing the temperature of polymer evaporation has shown to yield a wide array of degradation products (with higher mass)[123].

In electron beam assisted physical vapour deposition, the target (anode) is bombarded with an accelerated electron beam under high vacuum. The electron beam (produced by a charged W filament) causes evaporation of the metal/polymer from the target and deposits on cooler substrates. The mechanism of polymer evaporation by accelerated electrons is essentially thermal in nature, whereas in ion beam evaporation of polymers, the mechanism can be thermal or sputtering[123].

The main disadvantages of vacuum deposition processes are: [1] line of sight deposition; [2] control over the relative deposition rates of two or more materials is difficult; and [3] degradation of polymers can lead to products of unknown chemistry, making characterisation and co-relating properties to chemistry of deposited films difficult.

2.5.2 Spraying

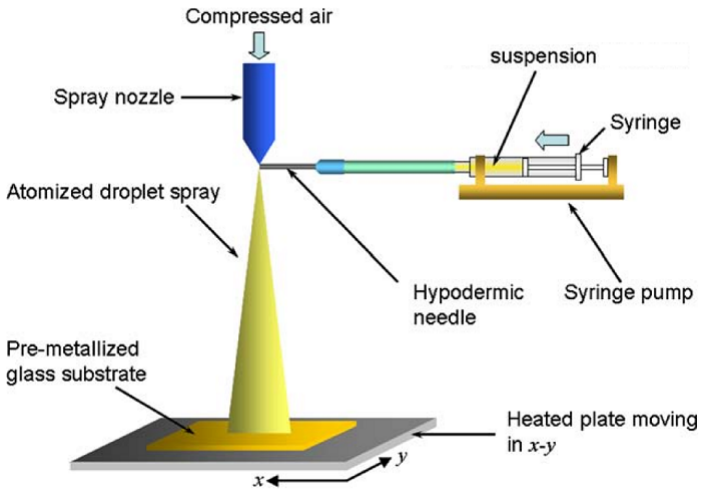


Figure 2.16: Schematic of spray deposition process[56,98].

In spraying[56,98], a high accuracy controlled flow rate syringe pump delivers a suspension (containing polymer and monomer) to an atomising device, such as

a hypodermic needle that is placed at the end of an atomising (spray) nozzle as shown in Fig. 2.16. The suspension is atomised continuously into droplets with diameters of less than 0.1 mm and is sprayed onto a heated substrate, which moves in the x-y direction. Films of required thickness can be produced by programmed repetitive spray cycles. The monomer can be polymerised (for example, thermally) later to produce a polymer-composite film. Well-dispersed $BaTiO_3$ nanoparticles embedded in a polydiacrylate matrix with dielectric constant of ~39 at 10 kHz has been produced from this process[98]. Maintaining well dispersed particles in the suspension is a challenge and this issue is usually addressed by using surfactants and by sonication.

2.5.3 Spin coating

Spin coating involves rotating (spinning) a substrate containing a polymer solution. Due to spinning, the polymer solution covers the substrate completely by centrifugal force and later, the solvent evaporates leaving behind a polymer film[124]. Fillers can be added to the polymer solution to produce composite films by spinning. This technique has been employed to produce dielectric composite films[16,26,125] but has been successful only on a small scale.

2.5.4 Other techniques

Many other processes such as ion implantation[121], sol-gel method and intercalation have also been tried. Processes such as extrusion coating and tape casting can be employed to produce high volume and cost effective composite films, but the thickness of these films can be well controlled only above a few μm. So, these processes are not suitable for production of extremely thin polymer composite films (in the order of nm) with high capacitances (for embedded capacitors).

2.6 Conclusions

Polymer-nanocomposites provide many attractive attributes for use in the thin film high energy density capacitors. However, as described in this review, there are several routes to enhance the capacity in these materials.

Composites containing conductive fillers offer the highest absolute dielectric constants of over 10^4, but critically controlling the filler volume fraction in large-scale production of capacitors is a major challenge and these capacitors are by definition always lossy.

Moderately high-k PNCs have been realized by dispersing $BaTiO_3$ particles to produce PNCs with k~15 at 10 kHz and v_f~0.25. Higher k values are difficult to achieve or not always desirable because higher volume fractions of filler are hard to process and the relatively high density of the filler undermines specific energy/power density, as well as breakdown strength. The dielectric properties of such ceramic-polymer based composites generally fall in the regime of effective medium theories (EMTs) such as a rule of mixtures. Figure 2.17 is a graphical representation of the properties of (a) polymers, (b) ceramics, (c) composites that obey an EMT, and (d) composites that do not obey an EMT. The subscripts p and c represent the "parent" phases - polymer and ceramic respectively, and the size of the circles represents the magnitude of the denoted variable. Although a composite represented in Fig. 2.17(c) does inherit the attractive properties of processibility into thin films (small d) with large area (high A) and high electric breakdown strength (high E_d) from a polymer, the effective enhancement in the dielectric constant is restricted even when high-k ceramics such as $BaTiO_3$ are used because the ceramic is always a minority phase.

Relatively low-loss PNCs with "super-normal" k have been fabricated by incorporating surface-modified fillers into a polymer matrix. The high k observed at low frequencies (<1 kHz) has been ascribed to the motion and accumulation of charges in and around the core-shell particles, which are a popular choice of sur-

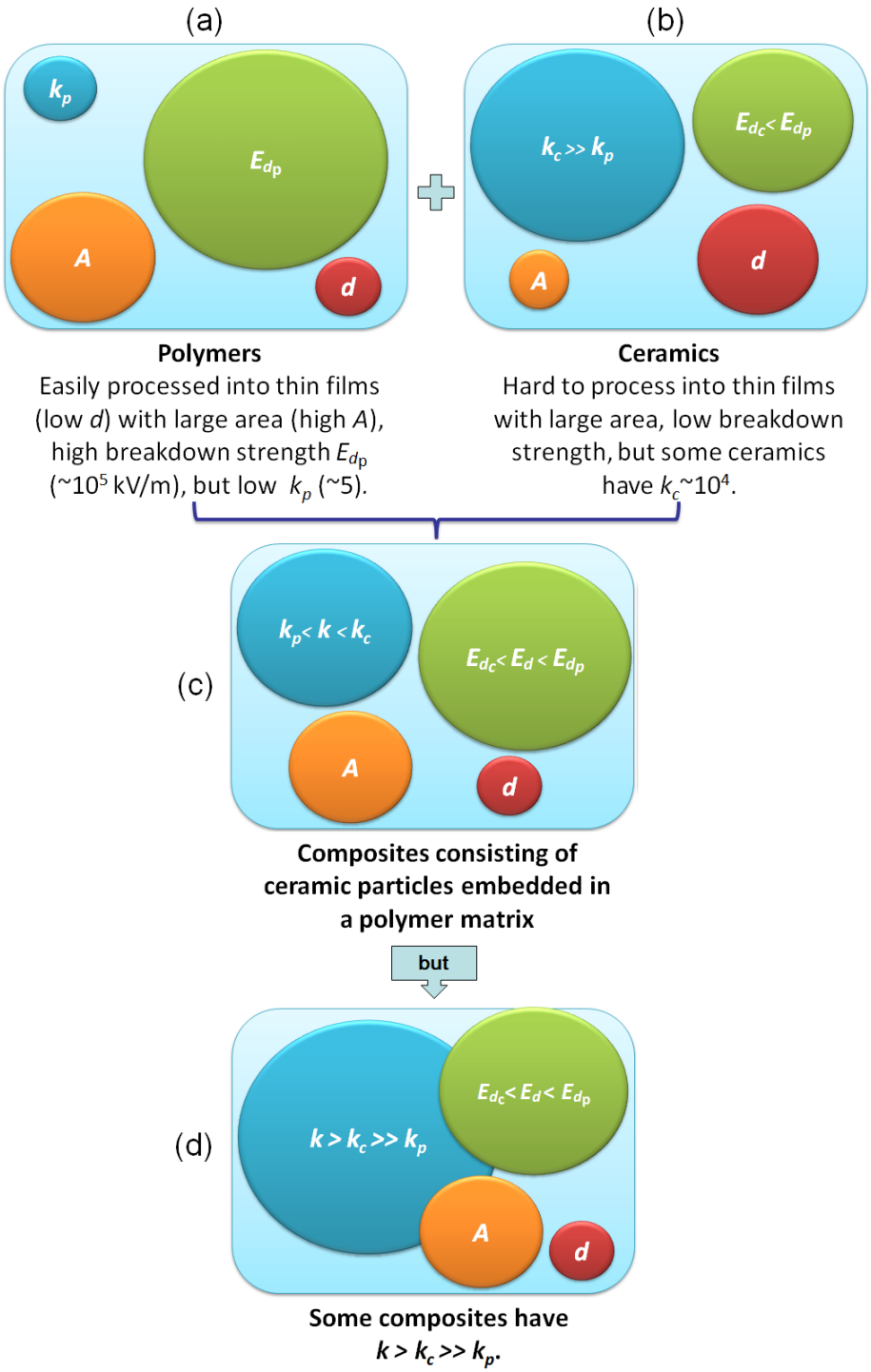


Figure 2.17: A graphical representation of the properties of (a) polymers, (b) ceramics, (c) composites that obey an effective medium theory (EMT), and (d) composites that do not obey an EMT. The subscripts p and c represent the "parent" phases - polymer and ceramic respectively, and the size of the circles represents the magnitude of the denoted variable.

face modified fillers, but the physical processes happening on a nano-scale that govern the bulk dielectric properties are not discussed in detail and continue to offer many exciting and challenging research areas for exploration. Although enhancing the polarisability of interfaces in PNCs is a promising approach to obtain the properties envisaged in Fig. 2.17(d), this approach demands critical control over the structure and chemistry of the interfaces at a nano-scale, stressing the importance of the choice of the processing technique.

As far as processing techniques are concerned, vacuum deposition and spraying, in principle, offer good control over the operation parameters and potential for cost effective scale-up. Most of the other current processing techniques, such as spin coating, face problems related to scalability when large areas of continuous films have to be produced (for example, continuous composite films for wound electrostatic capacitors).

Chapter 3

Experimental

The thrust of the thesis is to fabricate polymer based films by evaporation and to research how and why their dielectric response might be enhanced by the addition of a second metallic phase during processing. Electron microscopy and impedance testing, as well as the fabrication by evaporation are used extensively.
This chapter discusses the techniques used to fabricate and characterise polymer-nanocomposite (PNC) films. More information on specific experiments related to particular material combinations is provided in the subsequent chapters as appropriate, and this chapter focuses on the "platform" techniques that were used throughout.

3.1 Fabrication

3.1.1 Vacuum deposition

PNCs were fabricated by two vacuum based deposition techniques: co-deposition of a nylon-6 matrix and a metallic filler simultaneously, and alternate-deposition of materials in a "stack" of sequential layers using nylon-6 and various metals. An Edwards Auto 306 Cryo thermal evaporator was used for all the vacuum deposition experiments and is shown in Fig. 3.1. A schematic of a typical experi-

mental set-up inside the evaporator chamber is shown in Fig. 3.2. At the outset, the evaporator chamber was designed to accommodate four evaporation source boats, but only one boat could be heated at a time. The unit was therefore modified to accommodate an additional boat that was heated using a TDK-Lambda Genesys 8-300 DC power supply to allow co-evaporation of a metal and a polymer simultaneously. The boats were mounted on a rotating table that was later used to achieve alternate deposition of metal and polymer layers, rather than co-deposition. The detailed procedure to carry out co-deposition and alternate-deposition for the various PNCs is presented in subsequent chapters, and only the common aspects of vacuum deposition based fabrication are given below.

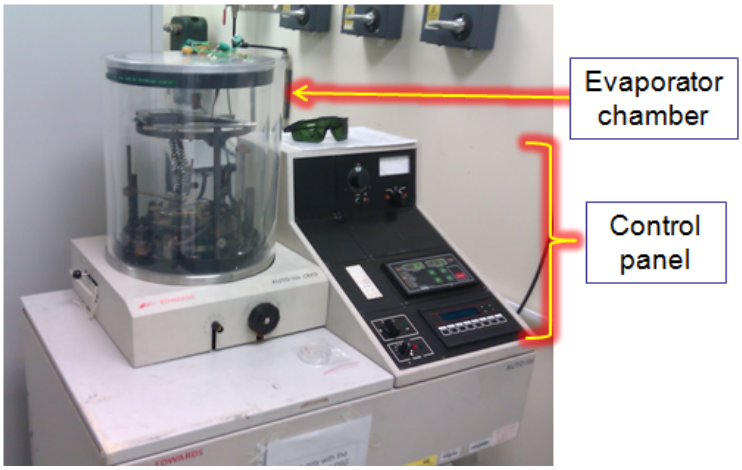


Figure 3.1: Edwards Auto 306 Cryo evaporator.

In all experiments, the deposition rate and the thickness of the polymer and various metallic coatings as they formed on a glass slide substrate were measured in real-time using a calibrated quartz crystal thickness monitor. The quartz crystal was placed immediately adjacent to the substrate in the deposition chamber. Since thermal evaporation was achieved by resistive heating of the sample "boats", the deposition rate was controlled by varying the heating current passing through the boats. Very many labourious experiments were carried out using different types of boats at various temperatures to establish stable and reproducible deposition rates: this proved to be a challenging task, especially while

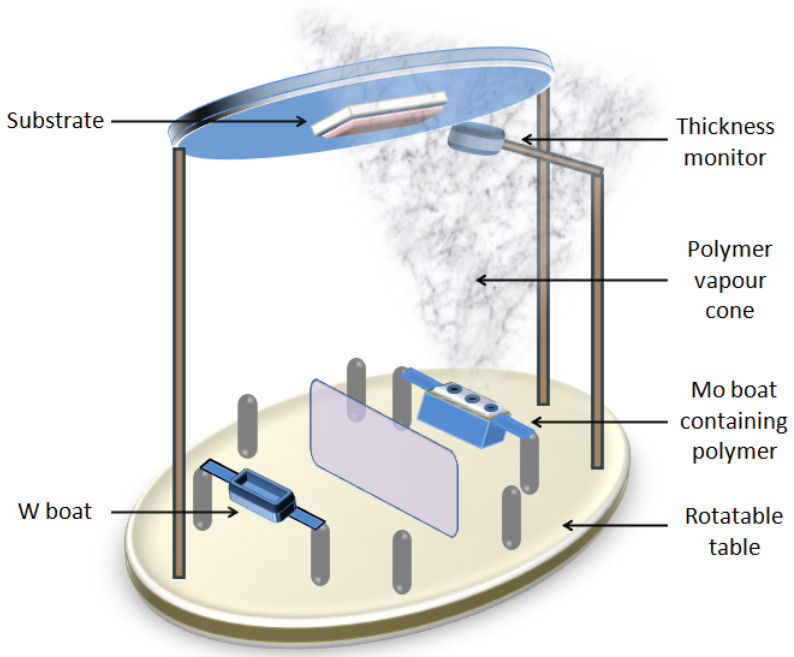


Figure 3.2: A schematic of a typical experimental set-up.

depositing two materials simultaneously using only one thickness monitor (more details later).

Figure 3.3 shows the various boats and filaments (Umicore) used for thermal evaporation. A relatively large Mo-boat with a perforated Mo-cover (#1) was used to evaporate polymers, for example nylon-6 (Ny), during co-deposition. It transpired that the use of a perforated Mo-cover was essential to prevent "spitting"[122] of the nylon-6 during evaporation. A K-type thermocouple was attached to the side of the Mo-boat as shown in Fig. 3.4(a) to monitor the temperature and prevent over-heating and degradation of polymer[126] during evaporation. The advantage of using a larger Mo-boat over smaller version (#2) was in the overall deposition rate $\dot{t}$ of up to 0.1 nm/s that could be achieved. Achieving the same magnitude of $\dot{t}$ with boat #2 required higher currents that eventually led to charring of the polymer. A comparatively high $\dot{t}$ for nylon-6, which was always the majority phase in all the co-deposited PNCs, facilitated greater flexibility in then varying and controlling the fraction of the more readily evaporating metal

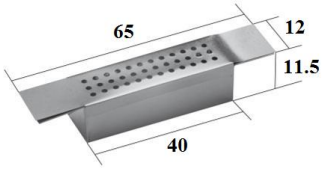
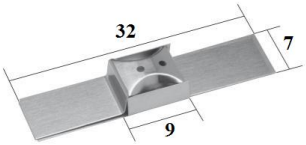
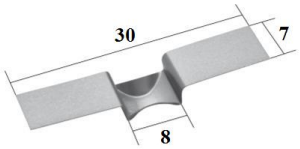
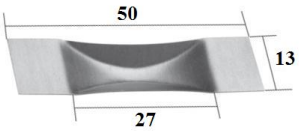
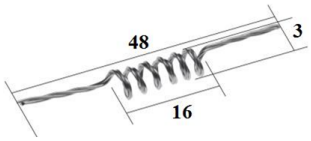
#	Boat (all units are in mm)
1	The relatively large Mo-boat with a perforated Mo-cover 
2	The relatively small Mo-boat with a perforated Mo-cover 
3	The smaller W-boat 
4	The larger W-boat 
5	The W-coil 

Figure 3.3: Boats and filaments (Umicore) used for thermal evaporation.

minority phase during co-deposition.

W-boat #3 was ideal to evaporate the metals Al and Ag at $\dot{t}$ ~1 nm/s since these metal sources conducted heat more readily and were quick to melt and vapourise. A larger and thicker (~0.3 mm) W-boat (#4) was then used to achieve controllably $\dot{t}$ <0.1 nm/s since the thicker boat heated up more slowly and steadily and allowed more stable control, avoiding under/over shoots in current/temperature. A W-coil was used to achieve the highest deposition rates of >1 nm/s since it could hold and melt the largest metal feedstock in the form of wound wire.

Generally, conditions that facilitated a relatively high $\dot{t}$ resulted in less control over the absolute value of $\dot{t}$, and maintaining $\dot{t}$ constant over a long period of

time (up to 0.5 h) was particularly difficult while evaporating polymers in this relatively primitive (but flexible) system. Since initial experiments showed that a thick W-boat offered the highest control over $\dot{t}$, a perforated Mo-plate was modified to act as a cover for W-boat #4, as shown in Fig. 3.4(b), and this combination was used to evaporate polymers successfully.

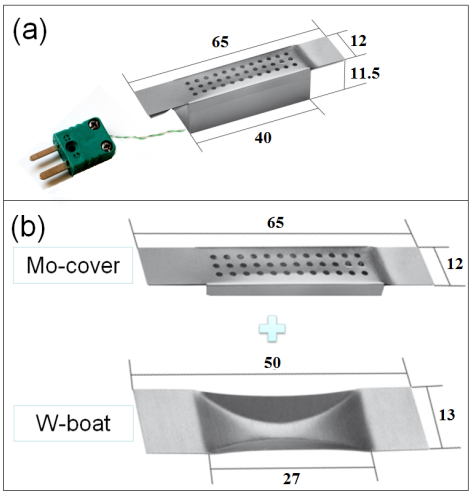


Figure 3.4: (a) A K-type thermocouple attached to a Mo-boat and (b) a modified boat consisting of a Mo-cover on a W-boat. All units are in mm.

Device yield

The yield was very low - only approximately 20% of the capacitors were free from short-circuits - during the optimisation process that primarily involved varying the deposition rate and layer thickness of the deposited material. However, after optimisation, approximately 95% of the capacitors showed consistent, capacitative behaviour.

3.2 Characterisation

The nature of the fine-scale microstructure and the presence of a disperse phase in a polymeric matrix presented very significant challenges for materials characterisation, and the development of suitable approaches that yielded the required

information constituted a major part of the experimental work in this thesis, with hundreds of hours dedicated in particular to electron microscopy of different types. Although the PNC and "core-shell" particle literature[16,20,22,57,59] in particular has grown rapidly in recent years, there were surprisingly very few convincing examples of careful characterisation of these types of particles in a polymer matrix in the literature. As will be shown, substantial experience and some bespoke approaches were required to link explicitly the measured capacitor behaviour to changes in the micro/nano-structure.

3.2.1 Transmission electron microscopy (TEM)

TEM was the most powerful tool used in this thesis to study the micro- and nano-structure of the PNCs, and therefore pertinent background information is provided on image formation and contrast mechanisms in the transmission electron microscope.

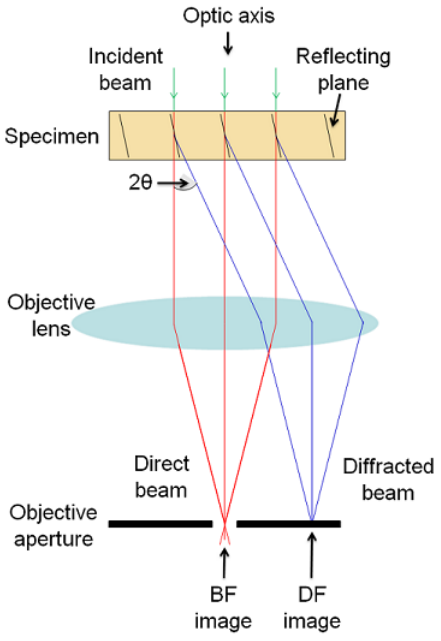


Figure 3.5: Schematic diagram of the formation of a bright-field (BF) and a dark-field (DF) image in a transmission electron microscope. θ is the angle between the incident beam and the reflecting plane.

When a parallel beam of electrons is incident on a specimen, the image formed

by the direct-beam is called a bright-field (BF) image, and the image formed by the elastically scattered or the diffracted beam is called a dark-field (DF) image. A schematic diagram of the formation of a BF and a DF image is shown in Fig. 3.5 where θ is the angle between the incident beam and the reflecting plane.

In scanning transmission electron microscopy (STEM), a focused beam of electrons is scanned over a specimen, and the scattered electrons are collected by a detector. Figure 3.6 is a schematic representation of the various signals that are formed during STEM. The forward-scattered electrons along the axis of the incident beam form the BF image; the electrons that are scattered through small angles ϕ <~55 mrad contribute to the formation of an annular dark-field (ADF) image; and the electrons scattered at higher angles form high-angle annular dark-field (HAADF) image[127].

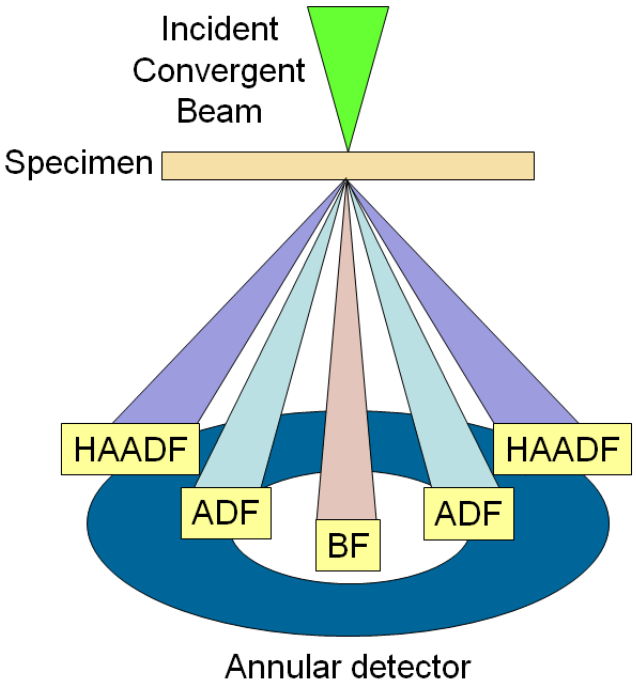


Figure 3.6: Schematic representation of BF, ADF and HAADF signals formed during STEM.

In order to obtain DF-STEM images, an annular detector is used to collect only the ADF and HAADF signals. Since the size of the annular detector is fixed, the camera length is varied to selectively receive the forward-scattered electrons

at a particular angle to obtain an ADF/HAADF image or an image formed by a contribution from both signals.

The following section briefly discusses the contrast mechanisms with a few typical images from the PNC investigations in which they are manifest. These images exemplify the rationale behind the choice of the various microscopy techniques to study the PNCs in this thesis.

Mass-thickness contrast

Mass-thickness contrast arises due to the variation in the sample-thickness or the atomic number Z of the elements present in the sample. Relatively thick regions and high-Z elements deplete/scatter the transmitted beam more than relatively thin and low-Z regions, as shown in Fig. 3.7, leading to the formation of relatively dark (bright) regions in a BF (DF) image. Figure 3.8 is a plan-view bright-field image of a "pure" evaporated nylon-6 film. The relatively dark regions, which can be (and initially were) easily confused as particles, in the amorphous polymer sample are due to the variations in thickness of the nylon-6 film. Therefore, this contrast can also provide a qualitative impression of the roughness of the film. Figure 3.9(a) shows a HAADF-STEM image of a nylon-based PNC film containing evaporated Al. Bright Al-rich regions, for example, the highlighted regions in Fig. 3.9(a), are distinguishable from the relatively dark nylon-6 matrix due the differences in the brightness arising from Z-contrast.

Diffraction contrast

Elastically scattered electrons from a crystalline region in the specimen give rise to diffraction contrast. Figure 3.9(b) is an ADF-STEM image of a PNC film containing Al and nylon-6. Since the image was taken at a relatively low angle, the elastically scattered beam was captured by the ADF detector and hence diffraction contrast is predominant. The highlighted region in Fig. 3.9(a) appears

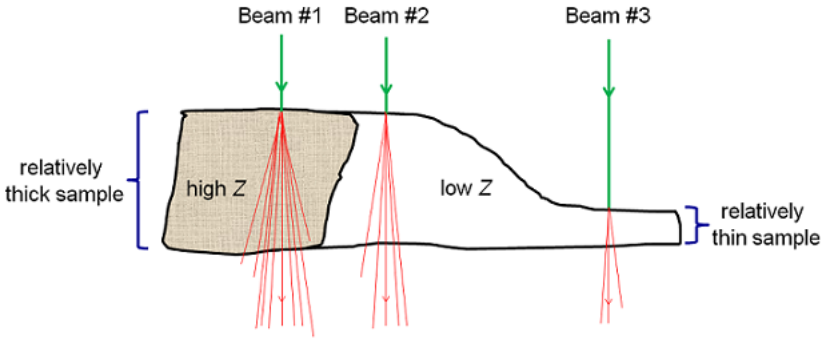


Figure 3.7: A schematic representation of electron beam scattering through a specimen with varying sample thickness and Z.

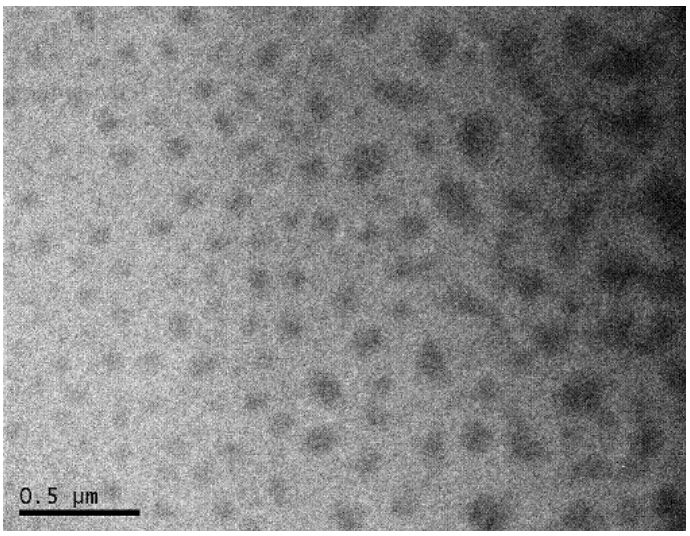


Figure 3.8: A plan-view bright-field (BF) image of a "pure" nylon-6 film.

brighter in Fig. 3.9(b) due to diffraction contrast arising from an Al-crystal. In a BF image, diffracting regions appear dark.

Phase contrast

High resolution transmission electron microscopy (HRTEM) makes use of phase contrast in image formation. When an electron beam passes through a crystalline sample, the electron waves that interact with the atoms of the crystal undergo a phase change. A HRTEM image is formed by converting the phase differences between the different beams at the exit-surface of the specimen into intensity variations. This conversion is achieved by suitably adjusting the aberrations, such as defocus, of the microscope. Figure 3.10 is a schematic representation of

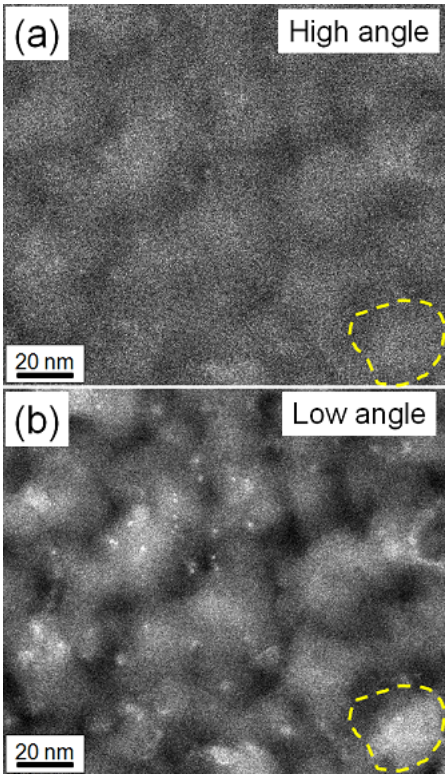


Figure 3.9: (a) HAADF-STEM image of a PNC film containing Al and nylon-6 showing Z-contrast, and (b) the corresponding ADF-STEM image taken at a relatively low angle showing (predominantly) diffraction contrast. The presence of bright Al-regions in a relatively dark nylon-6 matrix is evident from the DF-STEM images. The highlighted region in (a) appears brighter in (b) due to diffraction-contrast arising from an Al-crystal.

image formation in HRTEM. Figure 3.10 shows a large objective aperture being used to allow many coherently scattered beams for the formation of a HRTEM image. Figure 3.11 is a HRTEM image of an Al-crystal. The d-spacing between the lattice planes can be measured from such an image. HRTEM also gives a wealth of information (for example, on defects) about the crystallography on an atomic scale.

Sample preparation

Plan-view TEM specimens i.e. through-film orientation, were prepared by depositing the PNCs on a 400-mesh Cu-grid coated with a continuous C-film (Agar) that was mounted adjacent to the substrate while deposition proceeded. In this

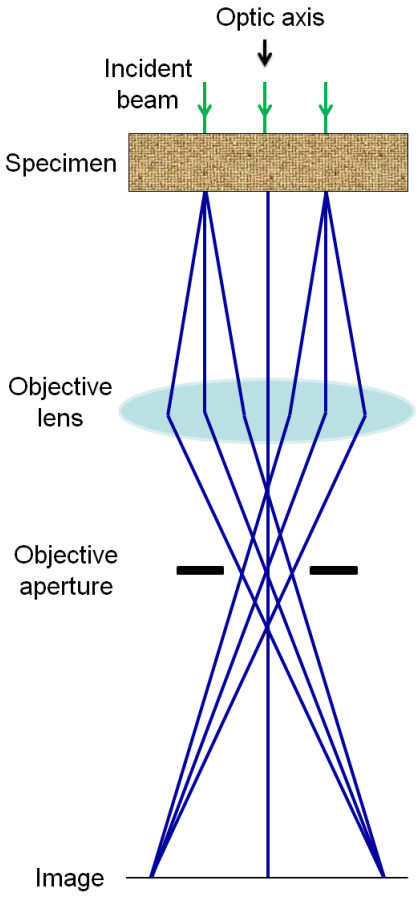


Figure 3.10: Schematic representation of image formation in HRTEM.

way, matching TEM samples were prepared for each PNC film that was manufactured and tested. The continuous C-film on the grid played an important role in supporting the electron beam-sensitive PNC film.

In the case of cross-sectional TEM examination, the PNC was deposited on a ~20 μm thick Al-foil adjacent to the substrate during fabrication. A narrow strip of the PNC-coated Al-foil was then carefully aligned along the axis of a pyramid-tip mould (Agar). The mould was filled with an epoxy resin that was freshly made each time, and the resin then cured at 60 ^{0}C for 24 hours. The pyramid containing the specimen was then mounted on a cylinder (Agar) using super-glue. Cross-sectional specimens were prepared by cutting 50-200 nm slices from the tip of the pyramid using a NOVA LKB Bromma microtome. These slices, which

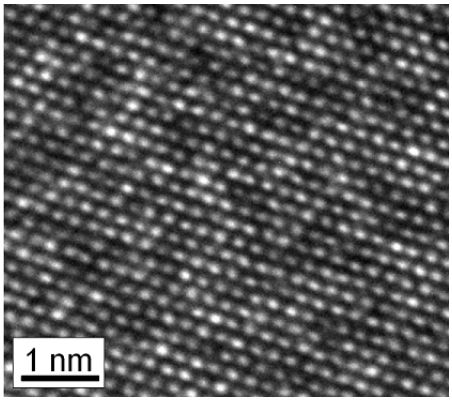


Figure 3.11: A HRTEM image of an Al-crystal.

were floated in water, were then collected and dried on a 400 mesh Cu-grid. The Al-foil also served as a marker to help locate the <50 nm thick PNC films in the microscope.

TEM instrumentation

The following transmission electron microscopes were used to study the structure and chemistry of the PNCs on a micro- and nano-scale:

1. JEM-2000FX

   The JEM-2000FX is an analytical instrument fitted with a tungsten filament. It has a point resolution of 0.3 nm, and the electron probe can be sized down to 1 nm. This instrument was primarily used for bright-field imaging of the PNCs at 200 kV.

2. JEM-2010

   The JEM-2010 is an analytical microscope with a LaB_6 electron gun. It has a point resolution of 0.19 nm, and the electron probe can be sized down to 0.5 nm. This microscope was used at 200 kV for BF and DF imaging, and to obtain selected area electron diffraction (SAED) patterns.

3. JEM-3000F

   The JEM-3000F is equipped with a field emission gun (FEG) and an Oxford

Instruments energy dispersive X-ray spectrometer with a super atmospheric thin window (SATW) detector. It was operated at 300 kV and had a point resolution of 0.16 nm. A HAADF detector was used for carrying out STEM, and customised lens settings allowed small probes to be formed, capable in the best case of resolving the Si dumbell at 0.14 nm spacing. The JEOL-3000F was used extensively to carry out BF and DF imaging, HRTEM, STEM and energy dispersive X-ray spectroscopy (EDS). The microscope was also used to obtain SAED patterns and elemental maps.

4. VG-HB501

   The Vacuum Generators (VG) HB501 instrument is a dedicated scanning transmission electron microscope with a cold field emission electron source. The instrument was used exclusively for annular dark field imaging and STEM at 100 kV with the help of Mr. Ron Doole, Dr. Rebecca Nicholls, and Prof. Peter Nellist.

5. JEM-2200MCO

   The JEM-2200MCO is equipped with a monochromated Schottky FEG source and aberration correctors are fitted to the imaging and probe forming lenses. The resolution in TEM imaging system is 0.12 nm, and the probe can be sized down to 0.1 nm in STEM. The microscope was used with the help of Dr. Neil P Young, Dr. Judy Kim and Prof. Angus Kirkland to carry out HRTEM and STEM at 200 kV.

Gatan, ImageJ, Web Electron Microscopy Applications Software (WebEMAPS), and CrystalMaker were used variously to acquire, process, analyse, and simulate TEM data. The features in some SAED patterns were enhanced through the adjustment of levels using the "HDR" plug-in in ImageJ/Picasa image processing software. All processed images will be henceforth referred to as "enhanced" images and presented alongside the original images.

3.2.2 Scanning electron microscopy (SEM)

A JEOL JSM-840F scanning electron microscope was used to characterise the PNCs. JSM-840F has a cold cathode field emission gun and operates between 0.5 and 40 kV. Using secondary electron imaging, the best resolution attainable on high contrast samples (Au on C) is 1.8 nm at 35 kV. The JSM-840F was primarily used in the secondary electron imaging mode at 5 kV to study the cross-section of the PNCs.

The cross-sectional SEM samples were prepared by freezing and fracturing the PNC films, supported on a glass substrate, in liquid nitrogen. The slivers of glass containing the PNC film were then held in between two parallel plates of a cross-sectional sample holder. In order to minimise charging of the sample while imaging, the sample was coated with ~3 nm of Pt using a Cressington sputter coater, and an electrical contact was made in between the PNC film and the metallic sample holder using carbon paste.

3.2.3 X-ray photoelectron spectroscopy (XPS)

XPS was performed in an ion pumped VG Microtech CLAM 4 MCD analyser system using a 200 W unmonochromated Mg X-ray excitation. Samples supported on carbon pads on stubs were introduced into the instrument via a turbo molecular pumped entry lock. The entry lock was pumped for about 15 min before the sample was introduced into the analysis chamber. The analyser was operated at a constant pass energy of 100 eV for wide scans and 20 eV for detailed scans. Data was obtained using SPECTRA version-8 software and was then processed using CasaXPS software. Peak areas were measured after satellite subtraction and background subtraction following the methods of Shirley[128]. The area under the principal peak of each element in the spectrum, divided by an empirically derived sensitivity factor[129] is proportional to the concentration of that element on the surface (approximately the top 10 nm). The sensitivity of the technique

was about 0.1 atomic percent, depending on the element under examination. The XPS experiments were carried out with the help of Dr. Alison Crossley and Dr. Hugh Bishop from the Oxford Materials Characterisation Service.

3.2.4 Impedance spectroscopy

A simple parallel-plate capacitor was formed from the PNC multilayer films by evaporating Al (40 nm thick) onto both sides of the PNC film of interest prior to dielectric measurements (more details later). A Solartron SI 1260 impedance analyzer was used to study the dielectric properties of the PNC based capacitors. The impedance analyser was interfaced with a computer and controlled by Solartron Analytical SMaRT software. An alternating voltage of 1 V (about a mean of 0 V) was applied at 1 kHz. All measurements were made *in-situ* in a Faraday cage that housed a thin-film heater. The temperature of the heating stage was controlled by a Eurotherm 2216e controller connected to a K-type thermocouple mounted next to the capacitors on the glass slide. Another K-type thermocouple was used to monitor independently the temperature of the heating stage. Changes were made subsequently in the Faraday cage sample holder during the course of the investigation to accommodate up to three samples at a time.

3.2.5 Surface Profilometer

The thickness of the PNC films was measured using a DekTak 6M profilometer (Veeco Instruments, Inc). The profilometer measures the surface topography by moving a diamond-tipped stylus across the sample. A "hills and valleys" profile[130] was then used to measure the average step height, between the "smooth" glass substrate as a reference and the surface of the PNC film.

Chapter 4

Co-deposition of Al and nylon-6

4.1 Introduction

Polymer-nanocomposites are promising dielectric materials in which a comparatively polarizable minority phase is embedded in an easily processable thin and large area polymeric matrix[9]. In addition to an increase in dielectric constant k over polymer only equivalents[36,49], PNCs retain attractive properties of polymers of low loss[131,132] and high dielectric breakdown strength[133]. However, the full potential of PNCs has not been realized commercially due to difficulties in scaling-up laboratory processing techniques, such as spin coating, used to contrive a fine dispersion of polarizable micro- and nano-scale particles in thin polymer films.

An alternative approach is based on vacuum deposition that is well established for polymer processing of thin films, and which has been scaled up, for example, for the roll-to-roll evaporator for the high-volume, cost-effective manufacture of multilayers on food packaging and polymer-only micro-capacitors.

In principle, this vacuum-based process might be adapted to produce composite films by co-deposition from two or more sources in which the volume fraction v_f of the constituent phases is controlled by varying the relative deposition rates. If

a good control over the relative deposition rates can be achieved, co-deposition facilitates three-dimensional and homogeneous distribution of the minority phase. Co-deposition, in principle, could also allow processing of a multi-material composite (three or more materials) by evaporating all of them simultaneously.

The objective of the work presented in this chapter was to explore co-deposition as a technique to fabricate polymer-nanocomposites with enhanced dielectric response over polymer only equivalents. Aluminium was chosen as the initial filler because Al is highly reactive readily forming a self-passivating layer of surface oxide[20,22] that may give rise to high-k due to enhanced interfacial polarisation. Nylon-6 (Ny) was used as the matrix because of the comparative ease of its processability by evaporation and wide-spread applicability. Both Al and nylon-6 are relatively cheap materials.

The effect of temperature and water on the co-deposited PNCs was studied by subjecting the PNCs to different types of heat treatment after deposition. The variation of the dielectric properties with v_f was then studied and compared with effective medium expressions. Microstructural investigations were carried out by employing cross-sectional SEM and TEM, and chemical characterisation was performed by XPS to confirm the presence of aluminium oxide and its potential role in any increase in k. Based on the experimental findings, a framework for processing and studying PNCs was established.

4.2 Experimental

4.2.1 Fabrication

PNC films were fabricated by co-evaporation and subsequent deposition of aluminium and nylon-6 in the Edwards Auto 306 Cryo evaporator, where the evaporator-chamber was evacuated to a pressure of 5x10^{-4} Pa before evaporation. With reference to the schematic arrangement in Figs. 4.1 and 4.2, the following steps

were carried out during processing:

1. An aluminium layer (thickness t~40 nm) was deposited on a glass substrate by thermally evaporating Al wire (99.999% pure, Alfa Aesar, 0.5 mm diameter) from a W boat at a deposition rate $\dot{t}$=0.5 nm/s where $\dot{t}_{Al}$ and t were measured in real-time using the quartz-crystal thickness-monitor. The deposited Al layer provided the "bottom" electrode of a simple parallel-plate capacitor.

2. The Al electrode was partially masked to preserve a metallic region without any PNC coating to serve as an electrical connection.

3. Before starting the co-deposition process, the glass substrate was covered completely while adjustments in $\dot{t}_{Al}$ and $\dot{t}_{Ny}$ to the target values were made. Firstly the W boat containing the Al was heated, and substantial time was given to melt the Al, adjust the heating current and to obtain the required $\dot{t}_{Al}$.

4. The Al source was then covered (but continued to be heated) and heating of a Mo boat containing nylon-6 (Aldrich) was started. The temperature was monitored to prevent excessive heating > 375 ^{0}C[126].

5. Once $\dot{t}_{Ny}$ ~0.1 nm/s was achieved, the Al source was again uncovered and the vapours of Al and nylon-6 allowed to mix in the vacuum chamber, and the cover over the pre-coated glass substrate was removed allowing the condensation of the vapour mixture onto the slide surface. To try to control the v_f of Al in the films, $\dot{t}_{Al}$ was varied while keeping $\dot{t}_{Ny}$ constant at 0.1 nm/s. If $\dot{t}_{Ny}$>0.1 nm/s, then nylon-6 charring resulted.

6. The coated substrate was covered with a different mask with ten discrete windows of equal area ~30 mm^2.

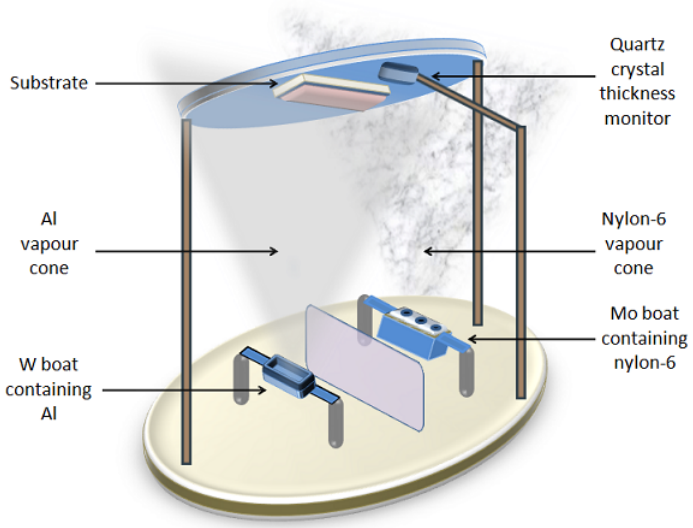


Figure 4.1: Schematic diagram of the vacuum co-deposition process for nanocomposite films.

7. A top Al electrode (t~40 nm) was evaporated through the mask to form 10 capacitors, as shown in Fig. 4.3.

Silver-dag was used to make electrical contacts with the bottom and top electrodes of each capacitor, as shown in Fig. 4.3. Subsequently the nominal volume percentage of Al in the PNC or "co-deposited nanocomposite" (CNC) is indicated by a subscript, for example $CNC_{30\%}$ indicates a PNC with nominally 30% Al or $v_{f_{Al}}$=0.3.

4.2.2 Characterisation

Dielectric characterisation was performed as previously described in Chapter 3. As well as the as-manufactured properties, the CNC-based capacitors were subjected to heat treatments while the dielectric measurements were carried out:

1. Cyclic heat treatment - the capacitors were subjected to repetitive cycles of heating to 40 ^{0}C constant temperature for ~20 hours and then cooling to 20 ^{0}C, for up to four cycles.

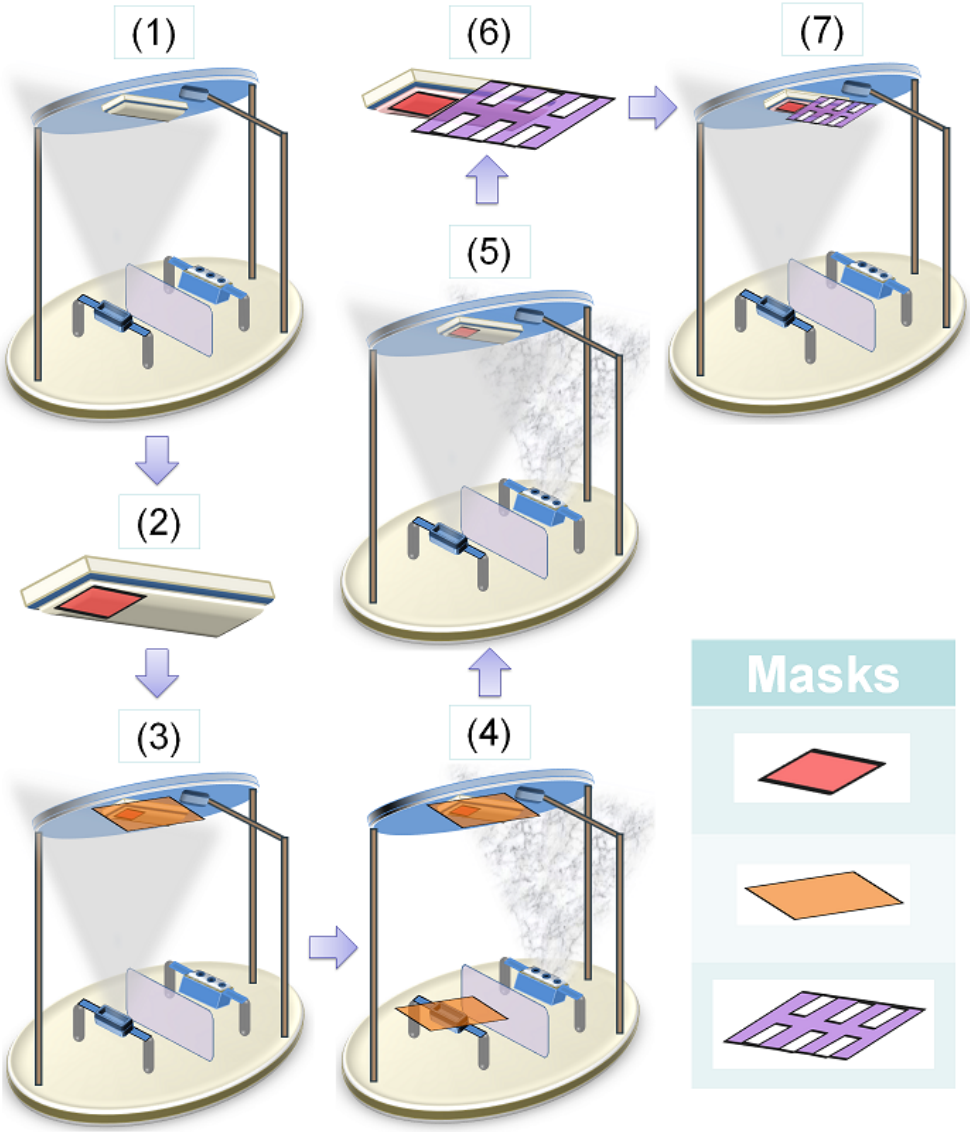


Figure 4.2: A pictorial representation of the steps involved in the co-deposition technique. Please refer to Fig. 4.1 for a description of the various parts of the schematic.

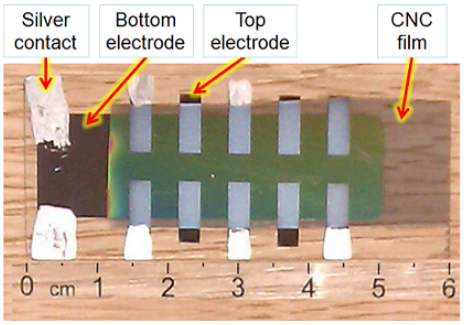


Figure 4.3: Parallel-plate capacitors based on co-deposited nanocomposite (CNC) films as the dielectric material.

2. Water drop treatment - the capacitors were heated from 20 ^{0}C to 40 ^{0}C and the capacitance was measured after every two-degree rise in temperature. The capacitors were then held at 40 ^{0}C for ~67 hours. Then, a small drop of water was put on the capacitor and the instantaneous dielectric response from the capacitor measured. The capacitor was then dried for another 2 hours at 40 ^{0}C.

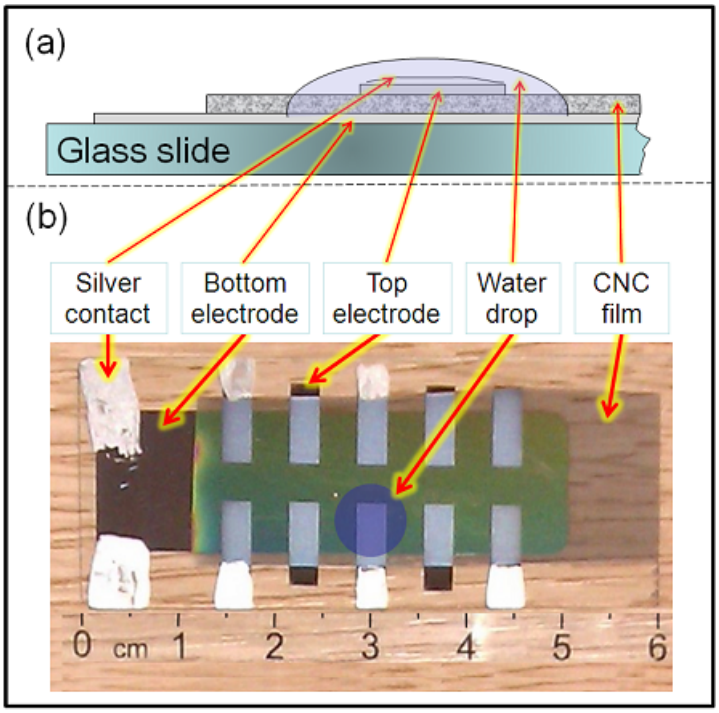


Figure 4.4: (a) A schematic showing the side-view of a capacitor onto which a small drop of water was placed, and (b) a top-view of the array of capacitors with the water drop.

Figure 4.4(a) is a schematic showing the side-view of a capacitor onto which a small drop of water was placed. The water drop was assumed to spread out into a near-circular area, as shown in the top view in Fig. 4.4(b). The spreading of water might have resulted in an increase in the area from which the capacitance was measured by 2-3 times. This error in the measured capacitance needs to be borne in mind while discussing the observed dielectric properties.

3. Constant temperature treatment - the capacitors were dried at 40 ^{0}C for 20 hours in a closed chamber.

All other characterisation procedures have been described in Chapter 3.

4.3 Results and discussion

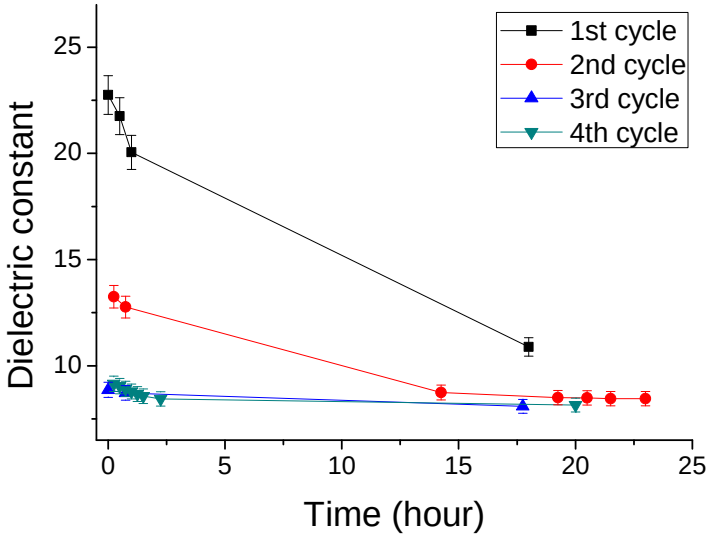


Figure 4.5: Variation of dielectric constant of a $CNC_{30\%}$ based capacitor at 1 kHz and time at 40 ^{0}C over four cycles. The four line-plots correspond to the data obtained from the four cycles of the cyclic heat treatment. The lines connecting the data points are only a guide to the eye.

Figure 4.5 shows the variation of k of a $CNC_{30\%}$ based capacitor at 1 kHz with time at 40 ^{0}C over four cycles. This particular experiment was carried out on a single sample over a period of four days. So the error bars associated with the data points were calculated only from the variation in the measured thickness of the CNC film at different points on the same glass slide and not from the variation in the dielectric constant from different samples.

In the first cycle, k dropped drastically from ~23 as manufactured and heated to 40 ^{0}C at 0 h to about half of initial value after ~18 h at 40 ^{0}C. When the capacitor was cooled to 20 ^{0}C and then re-heated to 40 ^{0}C, k increased slightly

to ~13 and then reduced again, this time to ~9 after 18 h at 40 ^{0}C. On the third cycle, k remained constant at 8-9 over an ~18 h period; the fourth cycle was similar. These observations suggested that the influence of temperature on the effective dielectric constant gradually reduced with an increase in the number of cycles. Any direct degradation of the nylon-6 at 40 ^{0}C was eliminated as an explanation for the fade in k since 40 ^{0}C was similar to the substrate temperature itself during co-deposition.

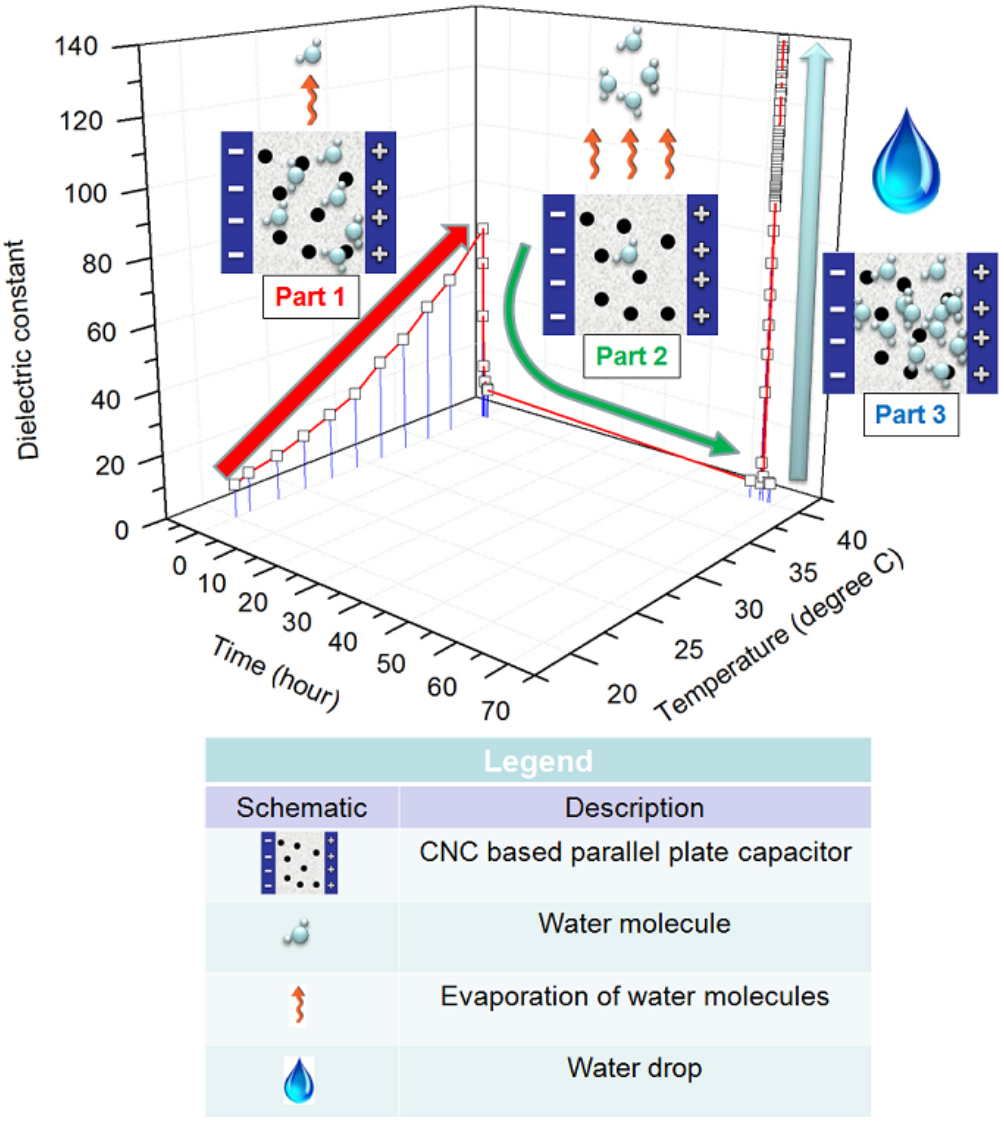


Figure 4.6: The variation of dielectric constant with time and temperature of a $CNC_{30\%}$ based capacitor during a water drop treatment.

Nylon-6 is a hydrophilic polymer that is known to absorb and retain water/water

vapour in amorphous domains[134–136]. Since - at this stage - no particular care was taken to store and test the capacitors in a controlled atmosphere, investigating the effect of any absorbed water on CNC performance was pursued, since given the very thin (<100 nm) nature of the CNC films, absorption of even a small amount of water vapour prior to testing might have a drastic effect on dielectric properties.

Figure 4.6 shows the variation of k with time and temperature for a $CNC_{30\%}$ based capacitor, combined with a schematic representation of the various stages involved in this "water drop treatment". When the temperature initially rose from ~20 ^{0}C to 40 ^{0}C (Part 1), over a relatively short time of 0.1 h, k increased from 10 to 67. In this portion, it is suggested that the increasing temperature and the presence of water molecules (see later) led to increasingly "polarisable entitites" and an increase in their number, because of newly formed, relatively mobile and polarisable polymer-segments[137–139] that arise due to simultaneous effects of water and temperature. The presence of water reduces the glass transition temperature T_g of nylon-6[134,140] ($T_{g_{Ny}}$ is in the range 43-49 ^{0}C), and in the vicinity of T_g, the polymer-segments gain additional mobility leading to enhanced polarisation[141,142]. It has also been suggested elsewhere that the dipole strength (related to the polarisability) of the segments is enhanced on absorption of water. Water also increases ionic conduction, and water itself is comparatively polar. Finally the presence of defective sites in the polymer due to the condensation processing co-deposition and the incorporation of a filler (in this case, Al) may have also helped produce a conducive environment for absorbing and retaining water in the CNC films, which again enhances k. Thus this initial sharp increase in k was primarily due to the combined effect of both temperature and absorbed water that was not removed during this initial fast heating.

During Part 2, the temperature was kept constant at 40 ^{0}C for 67 hours and k dropped from 67 to 5.5, due to the evaporation of most of the water molecules.

Absorbed water can remain in small quantities even after prolonged drying for 100 hours, because it is strongly bound to the polar sites[143,144]. So although "pure" polymers are known to be low-loss dielectrics, the presence of such strongly bound water increases the dielectric loss in "impure" polymers. In the last Part 3, k jumped to 140 when a water drop was put on the CNC at 67 h, and then dropped back to 6.5 within a couple of hours of continuous heating at 40 ^{0}C, confirming that water was responsible for particularly strong elevations in k in this case. Since the increase in k was about 25 times when the water drop was put, the increase in the measured capacitance due to spreading of the water drop leading to an increase the capacitor area by 2-3 times as shown in the Fig. 4.4(b) was unlikely to be the dominant effect in the observed many-fold jump in k.

Subsequently, all CNC based (and other PNC type) capacitors were subjected to a constant temperature treatment, described in section 4.2.2, to negate the effect of water vapour, before any dielectric measurements were made.

The dielectric response of the CNCs *at 40 ^0C* was studied and compared with some of the most popular analytical models from the literature[27,32,33,100]:

Rule of mixtures:

$$\epsilon_{eff} = v_{f_1}\epsilon_1 + v_{f_2}\epsilon_2 \tag{4.1}$$

Lichtenecker logarithmic mixing law:

$$log(\epsilon_{eff}) = v_{f_1}[log(\epsilon_1)] + v_{f_2}[log(\epsilon_2)] \tag{4.2}$$

Maxwell's Equation:

$$\epsilon_{eff} = \epsilon_1 \left(\frac{\epsilon_1 + 2\epsilon_1 - 2(1 - v_{f_1})(\epsilon_1 - \epsilon_2)}{\epsilon_2 + 2\epsilon_1 + (1 - v_{f_1})(\epsilon_1 - \epsilon_2)} \right) \tag{4.3}$$

where the subscripts 1 and 2 represent the two phases; ϵ and v_f represent dielectric constant and volume fraction respectively. The assumed values for ϵ_1

(alumina)[145–147] and ϵ_2 (experimentally deduced dielectric constant of nylon-6 at 40 ^{0}C) were 9 and 4.3 respectively. All expressions in Equations 4.1 to 4.3 assume composite systems with uniformly dispersed, non-conducting particles. The Yamada equation[33] was not used to estimate ϵ_{eff} because the parameter that describes the shape of the particles, n, in this correlation could not be determined reliably from the experimental data. These type of difficulties involved in characterising the Al-based nanoparticles are discussed further later.

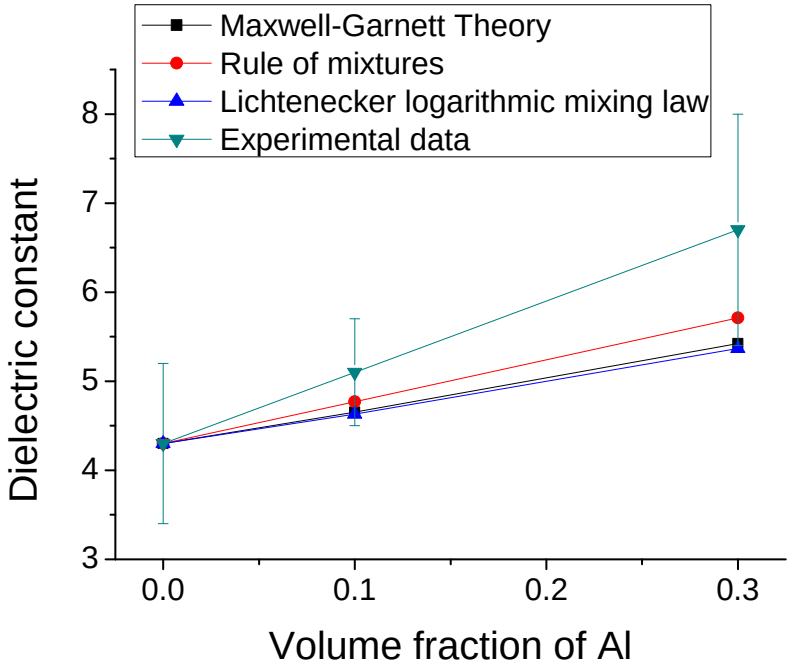


Figure 4.7: A comparison between averaged experimental data at 40 ^{0}C and predictions of dielectric constant as a function of v_f in CNCs at 1 kHz.

Figure 4.7 shows that the experimental data, while not in the "super-k" range usually used to indicate dielectric constants above 9 and notwithstanding the small range of v_f studied, were consistently above those suggested by commonly used expressions because the interface between the filler and the matrix in the CNCs might have had some trapped water, even after drying for 20 h at 40 ^{0}C, that slightly elevated k.

The plots of Equations 4.1 to 4.3 in Fig. 4.7 assumed that all the evaporated Al was in the form of alumina with a "bulk" dielectric constant. The oxidation of Al

might have taken place: (i) during the deposition process when Al reacted with O_2 present in nylon-6 and any residual chamber O_2, or (ii) when the CNCs were taken out of the vacuum chamber and exposed to atmosphere since the thin (up to 200 nm) nylon-6 films were unlikely to be entirely impermeable to atmospheric O_2. The former case was investigated by calculating the amount of O_2 in the chamber (see later), but no practical method for assessing the contribution of any reaction with nylon-6 to oxidation was conceived.

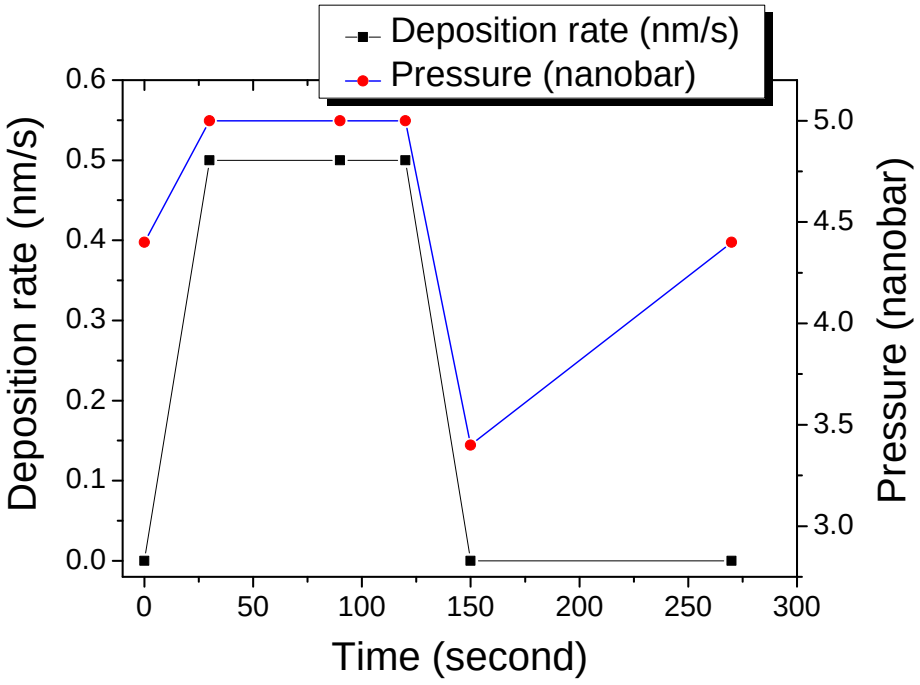


Figure 4.8: The variation of deposition rate and chamber-pressure with time during Al evaporation. Lines connecting the data points are only a guide to the eye.

Figure 4.8 shows a typical variation of deposition rate and chamber-pressure with time during Al evaporation. When the evaporation of Al was started, the chamber-pressure rose from 4.4 nanobar at 0 s and 0 nm/s to 5.0 nanobar at 30 s and 0.5 nm/s, due to the presence of the Al-vapour. When Al-evaporation was stopped at 120 s, the chamber-pressure very quickly reduced to 3.4 nanobar, which was lower than the initial pressure of the chamber, and which might be attributed to gettering of O_2 due to the conversion of gaseous Al (vapour) to solid

alumina or other oxide at deposition/condensation. The chamber-pressure then recovered to 4.4 nanobar within 120 s due to the unavoidable, continuous ingress of small amount of atmospheric air into the chamber (which presumably occurred throughout deposition). The net change in the chamber-pressure at 120 s is given by [(4.4-3.4)/4.4]*100=22.7%, which is reasonable given the concentration of atmospheric O_2 (21%).

It is also possible that the reduction in the chamber pressure was due to the gettering of gas atoms/molecules during the evaporation process by adsorption to the inner surfaces of the chamber, in addition to any chemical reaction. However, this reduction in chamber pressure was not observed during the evaporation of a relatively less reactive metal, Ag, suggesting that gettering by adsorption onto surface of the apparatus was not the primary contributor to pressure reduction.

In order to estimate if the amount of oxygen present in the chamber was sufficient to oxidise all of the evaporated Al, the ideal gas law was used:

$$PV = nRT \tag{4.4}$$

where P is the absolute pressure of the gas=10^{-4} Pa, V is the volume of the gas (in this case, the volume was approximated to be the volume of the chamber)=0.1 m^3, n is the number of moles of the gas, T is the absolute temperature of the gas (T was measured *in-situ* using a thermocouple)=293 K, and R=8.314 $Jmol^{-1}K^{-1}$ is the ideal, or universal, gas constant. The number of moles of O_2 present in the chamber was estimated at ~1 nanomole, which is ~ 10^6 less than the amount of O_2 (~1 millimole) required to oxidise the amount of Al present in the W-boat, 75 mg (even if 50 mg out of 75 mg is assumed to be evaporated), to form stoichiometric Al_2O_3. It was concluded therefore that the majority of Al oxidation took place by reacting with O_2 when the chamber was vented back to atmosphere.

Although experimental findings suggested the oxidation of Al, qualitative post-deposition analysis was pursued in order to confirm the presence of O_2 containing

phases such as alumina (Al_2O_3).

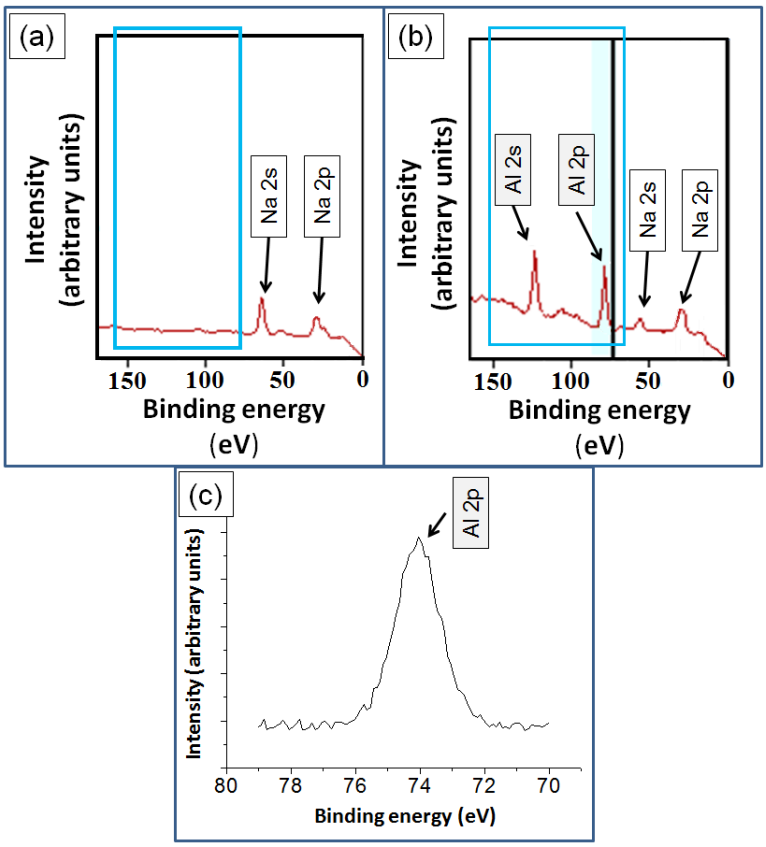


Figure 4.9: X-ray photoelectron spectra of (a) a "pure" nylon-6 film, (b) a $CNC_{30\%}$ film, and (c) $CNC_{30\%}$ film showing detailed scan of the Al 2p peak. The 2p peak in (c) was at 74.04 eV, which is characteristic of Al_2O_3.

X-ray photoelectron spectra from a "pure" nylon-6 film and a $CNC_{30\%}$ film are shown in Figs. 4.9(a) and (b) respectively. Two Al peaks, 2s and 2p, appeared only in Fig. 4.9(b) confirming the presence of Al in the nanocomposite film. In the spectrum from a detailed scan on the same CNC, shown in Fig. 4.9(c), the 2p peak appeared at 74 eV which is characteristic of Al_2O_3 [148]. The characteristic peak of Al alone [148] at 71.8 eV was not observed, again suggesting the complete oxidation of Al.

Figure 4.10 shows cross-sectional secondary electron images of a (a) "pure" nylon-6 film and (b) $CNC_{30\%}$ film. The nylon-6 film appeared similar to the $CNC_{30\%}$ film, and there were no particles visible in the cross-section of the $CNC_{30\%}$ film suggesting that the particles were either too small (<25 nm) or presented an

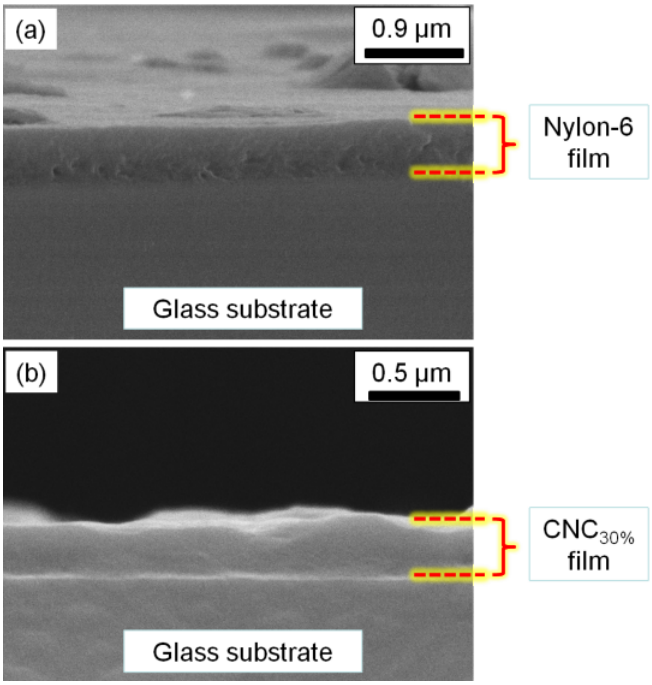


Figure 4.10: Cross-sectional secondary electron images of (a) "pure" nylon-6 film and (b) $CNC_{30\%}$ film.

unresolvable contrast difference from the nylon-6 matrix. A number of specimens at various v_f of Al and thicknesses were prepared but no particles were resolved by SEM in any of the specimens.

Mass-thickness contrast manifested as dark and bright regions in the TEM bright field (BF) image of a $CNC_{30\%}$ film shown in Fig. 4.11(a). The corresponding STEM dark field (DF) image is shown in Fig. 4.11(b). The dark (bright) spots in the BF (DF) image are due the presence of relatively thick regions of nylon-6. An EDS elemental map of Al and a typical EDS spectrum of the $CNC_{30\%}$ film are shown in Figs. 4.11(c) and (d) respectively. Figure 4.11(c) showed a near-homogeneous distribution of Al throughout the sample but no discrete, resolvable particles. Thus, the Al distribution was concluded to comprise a three-dimensional embedding of Al atoms or "clusters" of atoms in the nylon-6 film during the co-deposition process. There was no significant contrast between the arising "alumina" clusters/particles (no firm conclusions can be drawn from the TEM data regarding the chemistry of these tiny Al-rich regions) and the ma-

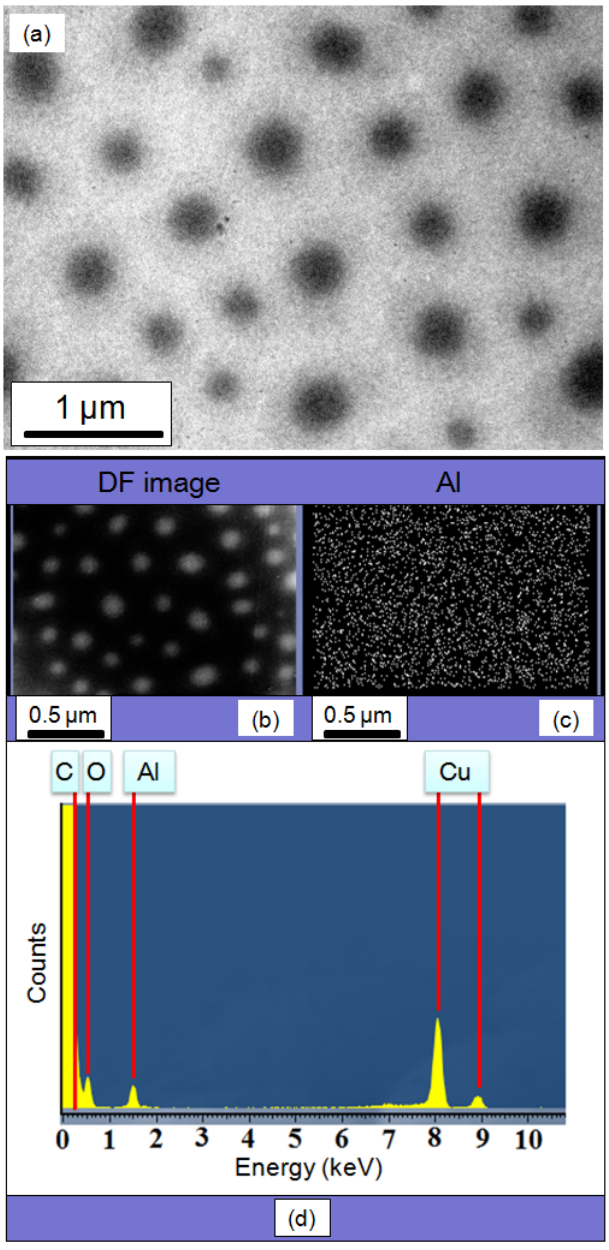


Figure 4.11: (a) TEM-BF image of a $CNC_{30\%}$ film, (b) the corresponding STEM-DF image, (c) the corresponding EDS elemental map of Al, and (d) a typical EDS spectrum.

trix in the TEM BF-image. Although nylon-6 has been reported to be semi-crystalline[136,149], the thin-film matrix of nylon-6 in the CNCs provided no significant diffraction contrast and was assumed to be predominantly amorphous. Any crystalline nature of the Al-rich/oxide clusters was also not detected, and were likely amorphous[146,147], again, due to the lack of diffraction contrast. The very small scale and lack of contrast "camouflaged" any Al-rich/oxide clusters in the nylon-6 matrix. Ultimately, the relatively low deposition rate of Al (< 0.1 nm/s) did not yield any resolvable crystals of Al/alumina in the co-deposited nylon-6 matrix.

4.4 Conclusions

Al and nylon-6 based nanocomposite films were successfully and reproducibly fabricated by a co-deposition technique. Various types of heat treatment showed that absorbed water vapour played a significant role in altering the dielectric properties of the CNCs, which was confirmed through various heat treatments applied to as-fabricated capacitor arrays. XPS studies suggested the presence of Al_2O_3 (or perhaps sub-stoichiometric version) in the CNCs, but the Al_2O_3 particles could not be resolved either in the SEM or TEM images, primarily due to a lack of contrast, which might be emphasised by an amorphous character. Nevertheless, TEM-based EDS elemental mapping showed an even distribution of Al throughout nylon-6 films.

A drop in the chamber-pressure during Al-evaporation was suggested to correspond with evaporated Al reacting with oxygen *in-situ* to form an Al-based oxide, which was supported by XPS spectra. However, a simple estimation suggested that the amount of oxygen present in the chamber was insufficient to oxidise all of the evaporated Al and suggested that a significant amount of Al might have reacted with oxygen present in the nylon-6 and most likely when the vacuum

chamber was vented.

Dielectric studies showed that ultimately the nylon-6 based nanocomposite films fabricated by co-deposition technique did not yield "super-k" behaviour envisaged in Fig. 2.17(d). Nevertheless, this work laid the necessary groundwork for establishing a modified approach to fabricate and study PNC-based capacitors with enhanced dielectric response, described in the following chapters.

Chapter 5

Alternate deposition of Al or Ag and nylon-6

5.1 Introduction

The previous chapter produced thin film polymer-nanocomposite (PNC) based capacitors with dielectric behaviour that was not in the "super-k" regime. It was concluded that this arose because the Al reactive filler fully oxidised when the evaporator chamber was vented to produce a two-phase film of nylon-6 and an Al-rich oxide, likely to be related to amorphous Al_2O_3.

As previously described, researchers and technologists are seeking PNCs with a dielectric constant that is greater than the dielectric constants of either its "parent" or matrix phase or the "filler" phase. Working in this direction, they have exploited the increase in dielectric constant observed around the near-percolation limit i.e. the percolation threshold at which an insulator starts percolating significant current (and which also represents an increasingly "lossy" capacitor), and the properties of discreet, often fine-scale interfaces between the matrix and filler phases in a PNC. The former effect cannot usually be easily controlled, and the difficulties involved in the processing of near-percolation composites has already

been discussed in previous chapters. The alternative interface or "interphase" approach might be expected to gain prominence as the microstructural scale of the PNC decreases to a nano-level, and progressively affect the measured or "effective" physical properties of the material. By controlling the chemistry and structure of large interfacial areas inherent to nanocomposites, interfacial polarisation properties might be promoted. It should be noted that here the interface in practice is not discreet with atomic thickness but is rather a thin region, perhaps nm, that has a *measurably* different crystal structure and/or chemistry, etc to that of either the matrix or the filler - hence "interphase" is sometimes used, rather than interface.

Recently, core-shell particles have emerged as promising fillers because of their suggested and apparent enhanced interfacial polarisation properties, where the outer "shell" fulfils the role of the interphase, and PNCs with k~40 at v_f~0.26 consisting of core-shell particles have been reported[57,150–152].

Some experimental insights[103] and computational studies[88] employing the phase field model[87] have suggested that the shell thickness of the core-shell particle influences their polarisability, along with filler shape, size, and size distribution[9,81,83]. The nature of polarisation has also been researched and the mechanism responsible for high k in these materials has been ascribed broadly to "interfacial polarisation"[103,104,150–152], often referred to as Maxwell-Wagner-Sillars (MWS) polarisation. However, a sound understanding of the shell chemistry and structure in relation to the physics of charge storage is yet to be fully developed based on experimental evidence. A major hurdle to achieving this is the difficulty involved in characterising the extremely thin (often less than a few nm's) shells in their pristine form because examination techniques tend to expose the particles to undesirable agents (chemicals, water, high temperature, etc) that affect their fine-scale structure and chemistry. Convincing resolution of the shell, distinct from any effects of the matrix and the inner core, is also frequently difficult.

To guide the design and fabrication of improved PNC capacitors, knowledge of the chemical and structural arrangement of phases at fine-scale, and their relation to capacitative mechanisms is needed. Based on this understanding, a simple and large-scale processing technique might then be developed, because the difficulties involved in scaling-up chemical-synthesis routes for core-shell particles tends to restrict their production to laboratories only and handling and incorporation into a polymer matrix safely, cleanly and without agglomeration is difficult. *In-situ* formation of the core-shell particles during PNC processing may offer a route to a more practical PNC process.

5.1.1 Alternate deposition technique

This chapter again explores the use of a vacuum based deposition technique to fabricate PNCs consisting of a metal (filler) and a polymer (matrix), but based on the work in previous chapters, an alternate deposition technique rather than the more intuitive co-deposition route is pursued because: (i) the relative volume fraction of the constituent phases can be more easily controlled, even at a nano-scale, by alternately depositing a calculated number of layers of materials as independent control in co-deposition proved impractical; (ii) the size of the particles of the minority phase, for example a metal filler can be controlled by adjusting the "thickness" of the metal layer (noting that a continuous metal layer must be avoided and rather metallic "islands" should be formed, which may or may not then undergo reaction/oxidation); (iii) the spacing between the filler particles in a vertical plane, along the y-direction as shown in the Fig. 5.1, can be controlled by varying the thickness of any intervening polymer layer and in a horizontal plane, along the x-direction in Fig. 5.1, by varying the amount of metal deposited; (iv) one can deposit a few alternating layers, up to hundreds; (v) the deposition of a relatively reactive metal and/or ion-bombardment can be employed to create nucleation sites[153] on the polymer surface prior to deposi-

tion of the filler-metal in an attempt to nucleate a large number of small metallic islands; (vi) the atmosphere of the vacuum chamber can be independently controlled while depositing each of the constituent phases; (vii) in principle, alternate deposition allows three or more phases to be fabricated without the complexity of controlling the relative deposition rates of two or more materials at once; and (viii) the simplicity of alternate deposition makes it a candidate for large-scale processing of PNCs.

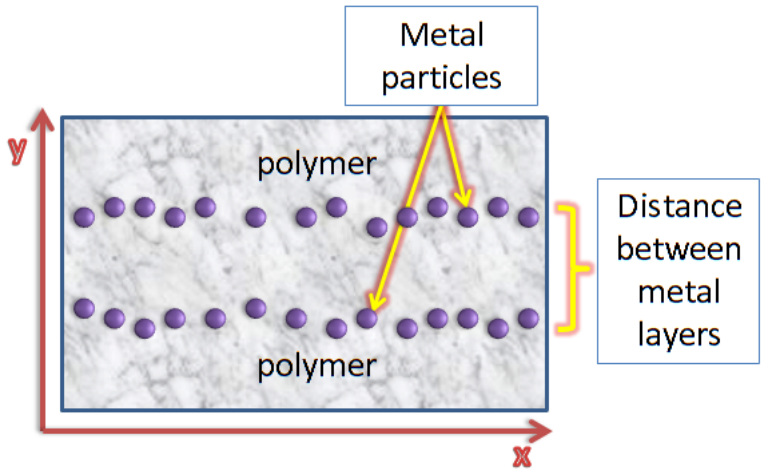


Figure 5.1: A schematic of an alternately deposited composite material with two layers of metal particles in a polymer matrix.

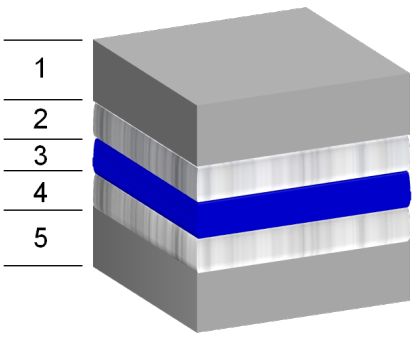
This chapter deals with the fabrication and study of alternately deposited PNCs consisting of Al or Ag and nylon-6. The formation and growth of Al and Ag nanoparticles on the nylon-6 surface and their encapsulation is studied by employing various electron microscopy techniques and the microstructure is correlated with the PNC dielectric response. Based on the importance of the formation of *in-situ* interfacial layers on reactive metals for charge accumulation, different nano-arrangements of Al and Ag are proposed, and the resulting dielectric behaviour is described and compared. In the latter half of the chapter, the variation of k is studied as a function of thickness of a deposited Al-layer sandwiched by the nylon-6, and changes in the Al-based nanostructure are studied using annular dark field (ADF)-scanning transmission electron microscopy (STEM) and

high resolution (HR) TEM. The role played by the evolving core-shell nanoparticle size and structure in enhancing interfacial polarisation while maintaining low loss is revealed.

5.2 Experimental

5.2.1 Fabrication

Alternately-deposited nanocomposite (ANC) films were fabricated by tandem deposition of five individual layers of metal and nylon-6. Al wire and nylon-6 were thermally evaporated alternatively using two different W boats onto a glass slide at a deposition rate $\dot{t}$ of 0.5 nm/s and 0.1 nm/s respectively. A schematic of the five alternate layers deposited during processing is shown in Fig. 5.2. The top and bottom (1st and 5th) layers of Al (40 nm each) formed the electrodes of a simple parallel-plate capacitor. The growth of Al (3rd layer), sandwiched between the nylon-6 layers (2nd and 4th - 20 nm each), was studied at various thicknesses (5, 10, and 15 nm). These samples are referred to as Al-ANC$_{0.5}$ (0.5 represents $\dot{t}_{Al}$=0.5 nm/s). Silver based ANCs (Ag-ANC$_{0.5}$) were fabricated by replacing Al with Ag (99.99% pure, Advent, 0.125 mm diameter) in the W-boat with a similar procedure. Another set of Al-based ANCs were fabricated with a similar procedure but $\dot{t}$ for both Al and nylon-6 was maintained at 0.1 nm/s. These samples are referred to as Al-ANC$_{0.1}$ (0.1 represents $\dot{t}_{Al}$=0.1 nm/s).



Layer	Material	Thickness (nm)
1	Al (electrode)	40
2	Nylon-6	20
3	Ag or Al	Variable
4	Nylon-6	20
5	Al (electrode)	40

Figure 5.2: A schematic of alternate layers of metal and polymer.

5.2.2 Characterisation

Differences/addition to the characterisation approaches describes in previous chapters are:

1. The ANC-based capacitors were dried at 40 ^{0}C for 20 hours to negate any water vapour effects prior to dielectric characterisation.

2. In order to remove the top layer of nylon-6 to probe particle chemistry by XPS, the ANCs were subjected to ion bombardment for 1 minute at 6 kV before acquiring XPS spectra.

3. A new TEM-specimen preparation technique was developed to characterise the Al-particles embedded in the nylon-6 matrix to overcome some inherent problems in the standard techniques. Generally for high magnification examinations, the particles are firstly separated from a polymer matrix by dissolving the polymer in a suitable solvent. This approach has two major drawbacks: (i) the particles of highly-reactive metals such as Al and Ti might react with the solvent, and (ii) the particles might undergo oxidation when exposed to atmosphere. Preparing a cross-section specimen also leads to exposing the particles to atmosphere and heating the specimen to about 60 ^{0}C to cure the epoxy/glue. Techniques based on preparing very thin (~100 nm) slices using an ultratome also involve water coming in contact with the specimen, and water (k~80) is found to have significant effect on the dielectric properties. So special care was taken to characterise the particles in the Al-ANCs.

   Sample preparation technique: The ANC was deposited onto a 200-mesh Cu grid. Initially in the TEM sample, particles were still "sandwiched" in the nylon-6 as fabricated and as shown in the schematic in Fig. 5.3. Then the electron beam was used to carefully ablate the nylon-6 in order to expose the particle-shell and allow imaging of its structure, rather than any

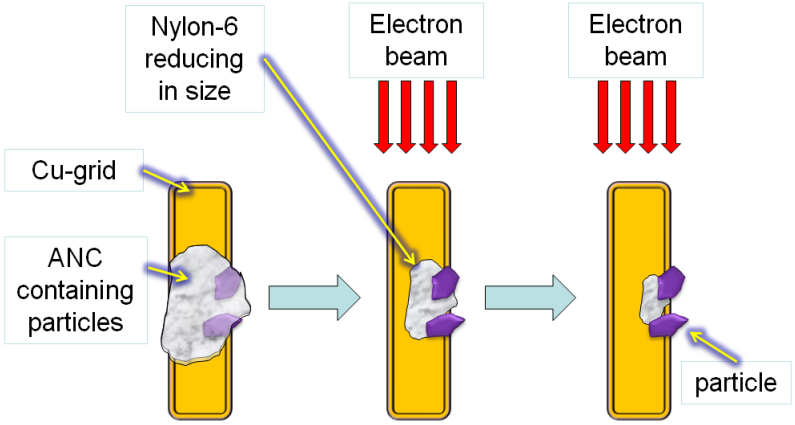


Figure 5.3: A schematic of the Cu-grid containing ANC used for HRTEM studies.

induced structure close to the shell but originating from the nylon-6. The microscope column was maintained at ~10^{-5} Pa throughout and there was no evidence in any images of any evolving *in-situ* oxidation of the particles.

All other characterisation procedures have been described in Chapter 3.

5.3 Results and discussion

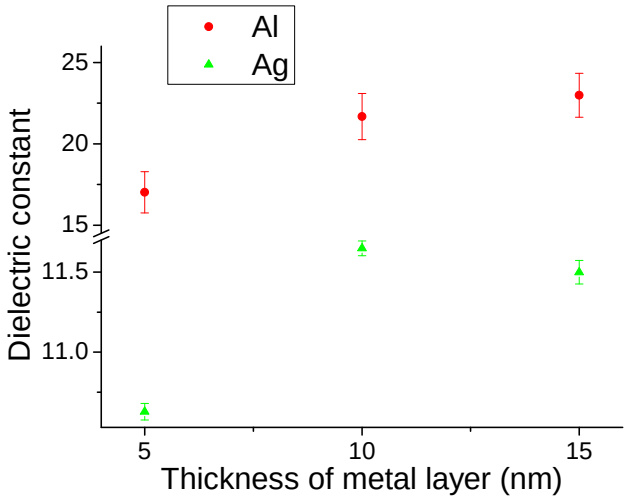


Figure 5.4: Variation of dielectric constant k of Al-ANCs$_{0.5}$ (●) and Ag-ANCs$_{0.5}$ (▲) with thickness t of deposited metal layer at 1 kHz and 40 ^{0}C.

Figures 5.4 and 5.5 show the variation of dielectric constant k and dissipation

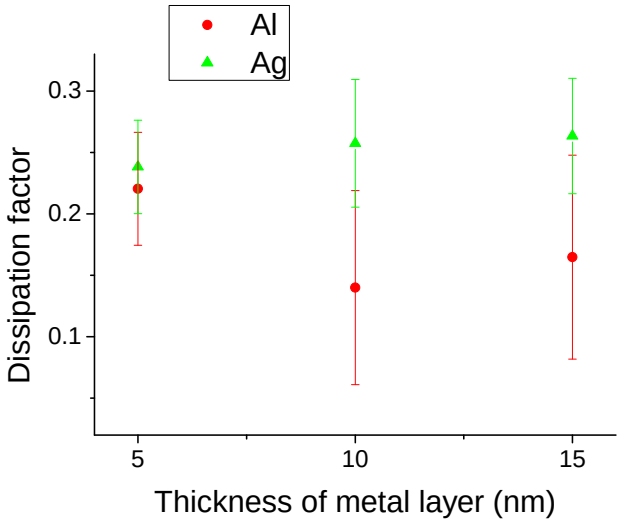


Figure 5.5: Variation of dissipation factor *tan* δ of Al-ANCs$_{0.5}$ (●) and Ag-ANCs$_{0.5}$ (▲) with thickness t of deposited metal layer at 1 kHz and 40 ^{0}C.

factor *tan* δ respectively of Al-ANCs$_{0.5}$ (●) and Ag-ANCs$_{0.5}$ (▲) as a function of the thickness t of deposited metal layer at 1 kHz and 40 ^{0}C. For reference, k and *tan* δ for "pure" deposited nylon-6 were ~4.3 and ~0.19 respectively. At t=15 nm, k of Al-ANCs$_{0.5}$ was approximately twice that of Ag-ANCs$_{0.5}$; the k for both ANCs also increased with increasing t. *Tan* δ of Ag-ANCs$_{0.5}$ was in the range 0.24-0.26 and was higher than that of Al-ANCs$_{0.5}$ (*tan* δ=0.14-0.22) for all t.

Figures 5.6(a), (b), and (c) show bright field (BF)-TEM images of Ag-ANCs$_{0.5}$ at t=5, 10 and 15 nm respectively. Disc or perhaps spherical nano-islands of Ag formed at t=5 nm, and these disc-like (in projection) particles grew and formed inter-connected islands at t=15 nm due to Volmer-Weber growth[(154)]. Noble metals such as Ag and Au are known to grow by Volmer-Weber mode because the interaction between metal atoms is stronger than the interaction between the metal atoms and the polymer surface. This led to the formation of three-dimensional, well-separated Ag-islands in the nylon-6 at t=5 nm.

The annular dark field (ADF)-STEM image in Fig. 5.7(a) of a Ag-ANCs$_{0.5}$ at t=5 nm further confirmed the presence of discrete Ag-islands (bright) in the nylon-6 matrix (dark). The d-spacings measured from the corresponding high resolution

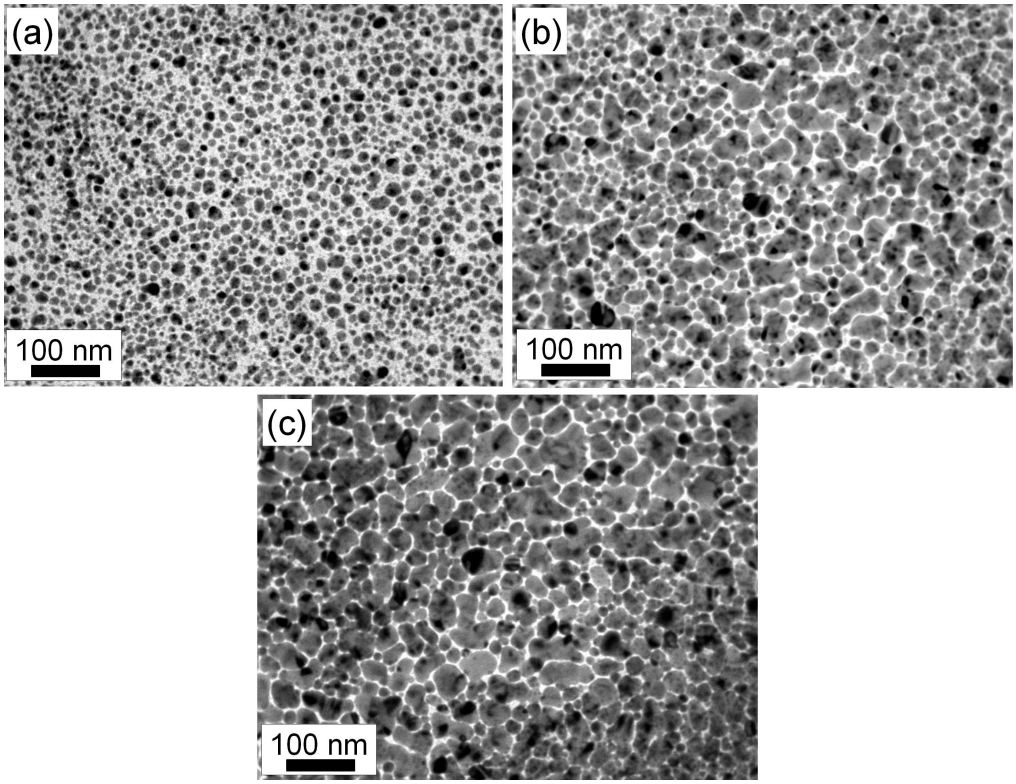


Figure 5.6: BF-TEM images of Ag-ANCs$_{0.5}$ at (a) t=5, (b) t=10, and (c) 15 nm.

transmission electron microscopy (HRTEM) image, Fig. 5.7(b), and the selected area electron diffraction (SAED) pattern, Fig. 5.7(c), closely matched the d-spacings of Ag [measured d-spacings: 0.24 nm (111), 0.21 nm (002), 0.15 nm (022), and 0.12 nm (113)]. The low reactivity of Ag with O_2 due to the unfavourable free energy of formation of Ag-oxide (assuming that Ag formed Ag_2O by attaining its most common oxidation state of +1, ΔG_{Ag_2O}=-11.21 kJ/mol at 25^0C) led to minimal or no oxidation of Ag. Based on these observations, a cross-sectional schematic representation of the Ag-ANC$_{0.5}$ based capacitor at t=5 nm is shown in Fig. 5.7(d). The nano-islands of Ag are shown embedded in the nylon-6 matrix in a nominal 5 nm thick layer.

Interfacial polarisation is known to occur due to piling of charges at the interfaces in heterogeneous materials as previously described in Chapter 2. The new interfacial areas formed by the incorporation of Ag into nylon-6 might therefore provide additional region for charge accumulation resulting in the enhancement

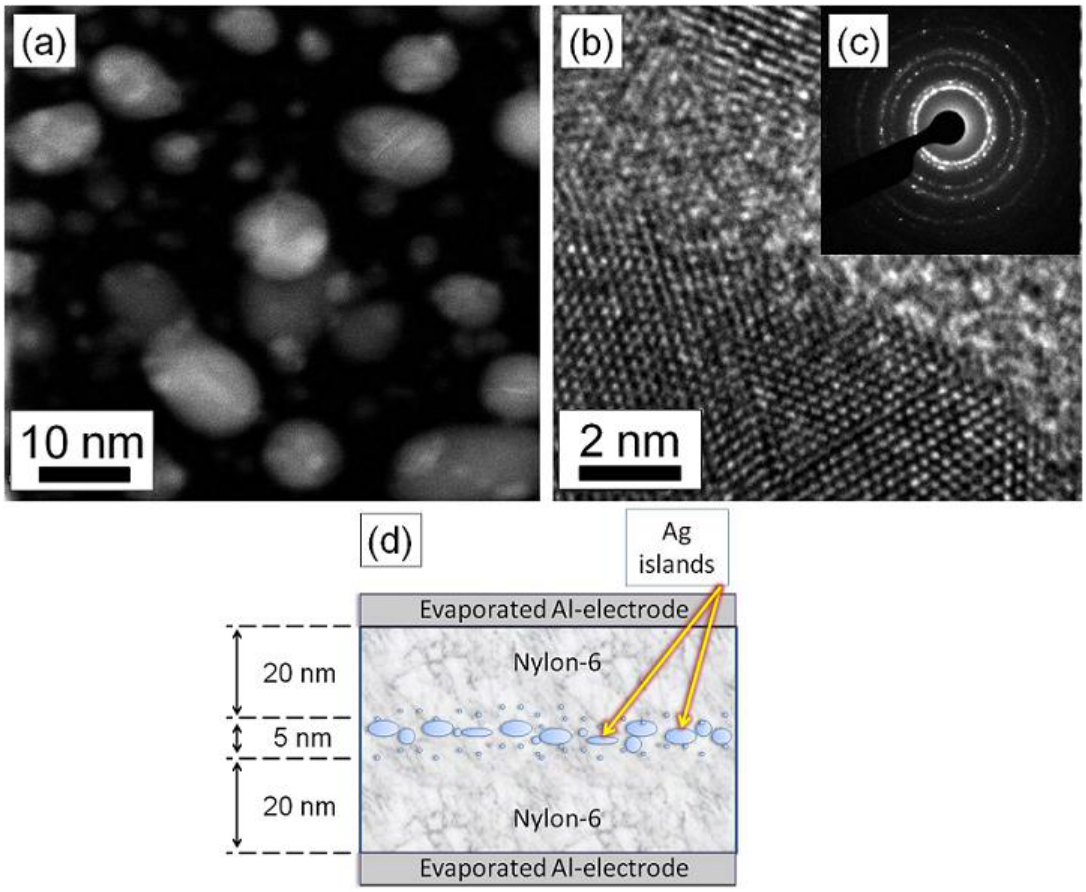


Figure 5.7: (a) ADF-STEM image of Ag-ANCs$_{0.5}$ at t=5 nm, (b) corresponding HRTEM image, (c) corresponding selected area electron diffraction (SAED) pattern, and (d) a cross-sectional schematic representation of Ag-ANC$_{0.5}$ based capacitor at t=5 nm.

in the dielectric properties. The high volume fraction of Ag in the 5 nm thick layer might also lead to the formation of a relatively "lossy", near-percolating network of micro- or nano-capacitors[35,36,49–56] leading to an increase in k of the Ag-layer. Figures 5.4 and 5.5 show that *both* k=10.5-11.5 and *tan* δ=0.24-0.26 for Ag-ANCs$_{0.5}$ was higher than k~4.3 and *tan* δ~0.19 for "pure" nylon-6 at all t. However, the overall enhancement in the dielectric properties was restricted because the Ag-layer is sandwiched between two 20 nm thick nylon-6 layers so that the more polarisable nano-capacitor network is confined to the centre only, rather than throughout the thickness of the ANC film.

The increase in k from ~10.5 at t=5 nm to ~11.5 at t=15 nm might be due to

the increase in the volume fraction of Ag. It was considered likely that t>15 nm would lead to the formation of a continuous layer of Ag, without discrete Ag nano-islands, that acts as an electrode similar to the Al-electrodes of the capacitor.

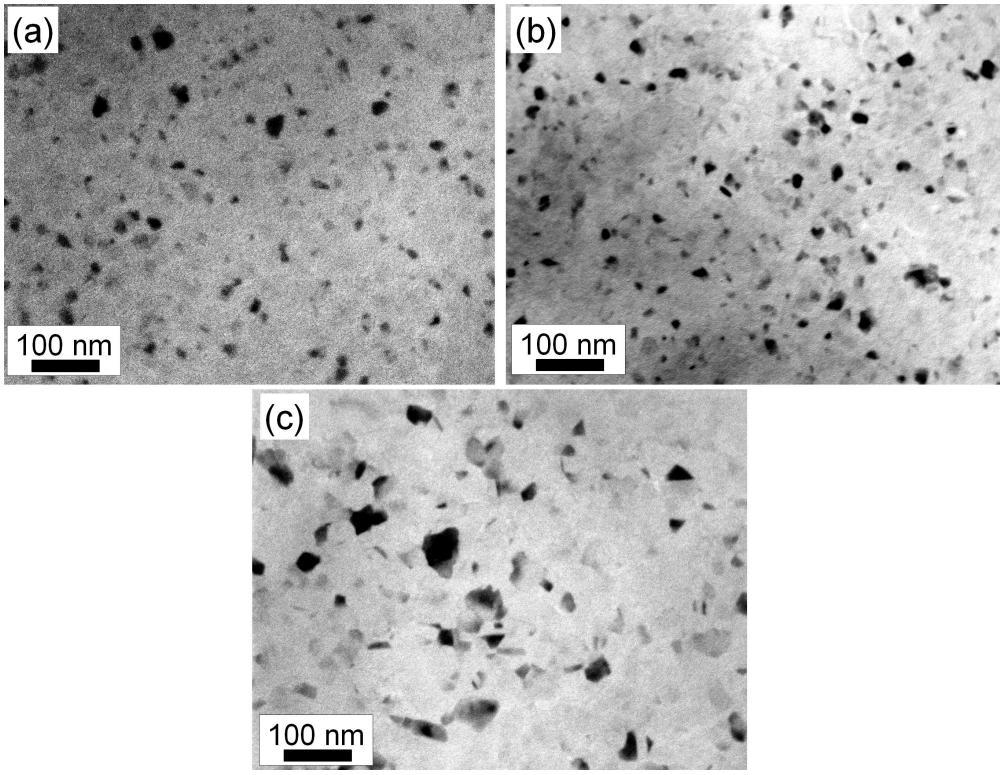


Figure 5.8: Bright field (BF) TEM images of Al-ANCs$_{0.5}$ at (a) t= 5 nm, (b) t=10 nm, and (c) t=15 nm with a bright matrix containing relatively dark nanoparticles.

BF-TEM images of Al-ANCs$_{0.5}$ at t=5, 10, and 15 nm are shown in Figs. 5.8(a), (b), and (c) respectively. The images show dark nanoparticles of 5-60 nm diameter dispersed in a relatively bright matrix. The presence of any Al-oxide shell was not distinguishable from the nylon-6 matrix in the BF-TEM images and both might be expected to be substantially or wholly amorphous. Nonetheless, previous work involving the evaporation of Al[155], the large free energy change for oxidation ($\Delta G_{Al_2O_3}$=-1582.3 kJ/mol at 25^0C) and the pervious nature to O_2 of nylon-6 strongly suggested the oxidation of Al.

A further BF-TEM image of Al-ANC$_{0.5}$ at t=5 nm is shown in Fig. 5.9(a) with the

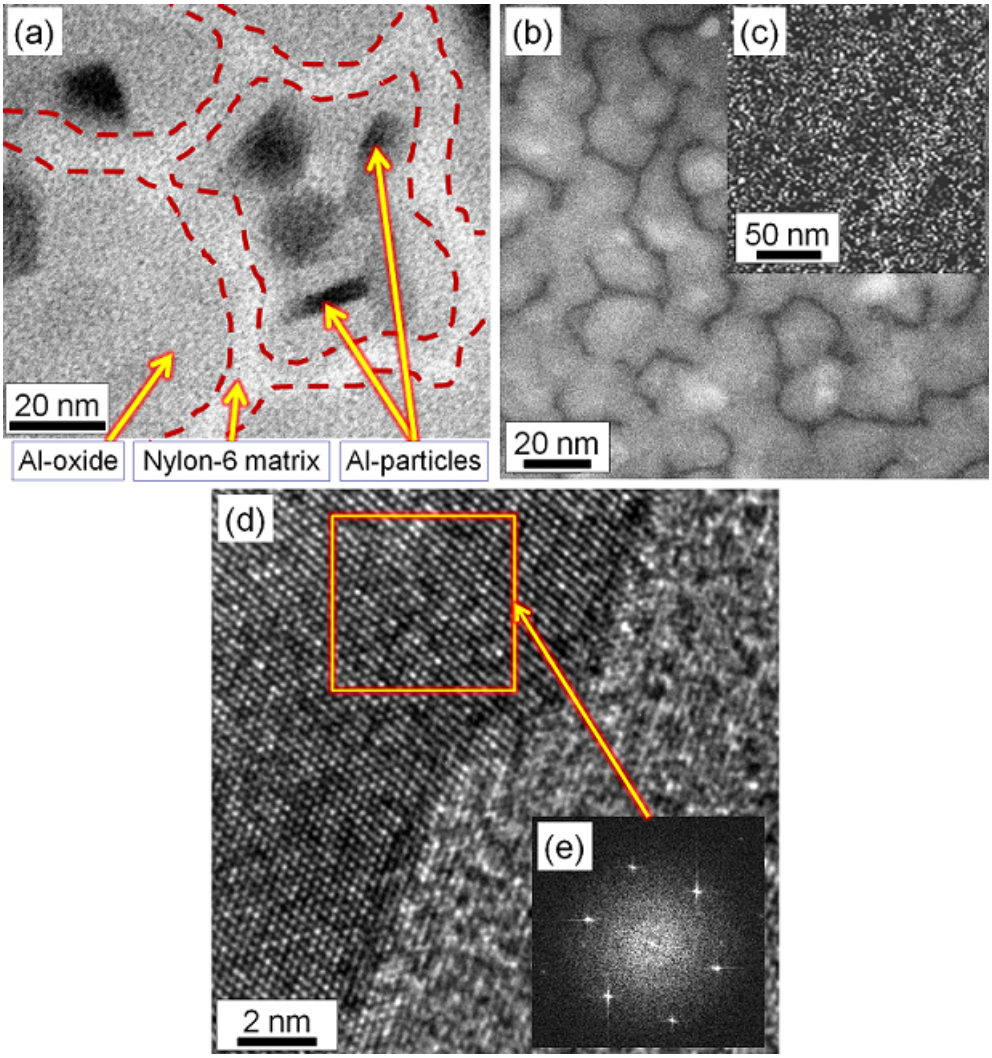


Figure 5.9: (a) A BF-TEM image of Al-ANC$_{0.5}$ at t=5 nm, (b) corresponding ADF-STEM image, (c) corresponding EDS elemental map of Al, (d) a HRTEM image of the Al-ANC$_{0.5}$, and (e) corresponding FFT from highlighted region.

marked region containing nanoparticles. This region was darker than the nylon-6 "matrix", which appeared as a light contrast, branched dendritic continuous phase separating dark regions. The contrast was due to differences in atomic number Z of Al and lighter elements in nylon-6, which is shown more clearly in the ADF-STEM image in Fig. 5.9(b). The crystalline nanoparticles now appeared very bright due to high diffraction contrast. The corresponding EDS elemental map of Al in Fig. 5.9(c) revealed that Al was distributed throughout the film, not only in the nanoparticles, which suggested that the evaporated Al not

only formed discrete, crystalline nanoparticles but was also relatively uniformly deposited as Al-oxide based islands delineated by the branched nylon-6 "matrix", and as previously seen in the co-deposited films in the previous chapter. Figure 5.9(d) shows a HRTEM image of Al-ANC$_{0.5}$ and where d-spacings measured from the HRTEM image and the spots from the fast Fourier transform (FFT) of the image, Fig. 5.9(e), corresponded to Al [d~0.23 nm (111) and d~0.2 nm (002)]. The BF-TEM image in Fig. 5.10(a) is from a cross-section of an Al-ANC$_{0.5}$ and showed a continuous film of Al at t=15 nm. The spots in the electron diffraction pattern, Fig. 5.10(c), from the selected area aperture shown in Fig. 5.10(b) reinforced the presence of crystalline Al. A plan-view of the same sample in STEM dark-field imaging mode in Fig. 5.11 showed a multi-faceted, tiled-structure of poly-crystalline Al.

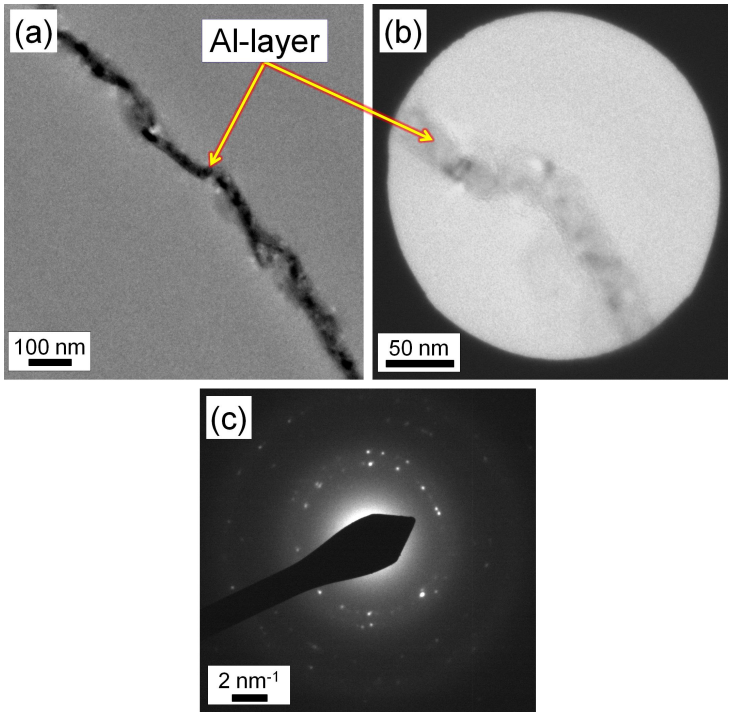


Figure 5.10: (a) A cross-sectional BF-TEM image of the Al-ANC$_{0.5}$ film at t=15 nm, (b) the region where the selected area aperture was placed, and (c) the corresponding SAED pattern.

Considering all the microscopy observations of Al and Ag, the enhancement in k for ANCs containing Al was primarily due to the differences in the oxygen reac-

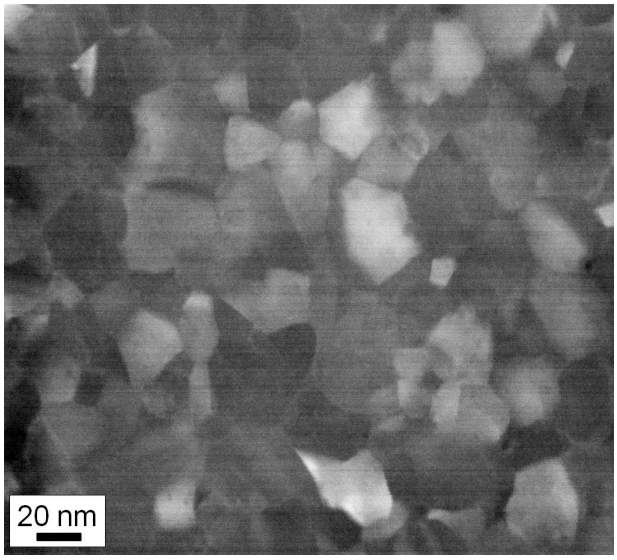


Figure 5.11: A plan-view ADF-STEM image of the Al-ANC$_{0.5}$ film at t=15 nm.

tivity of Al ($\Delta G_{Al_2O_3}$=-1582.3 kJ/mol at 25^{0}C) and Ag (ΔG_{Ag_2O}=-11.21 kJ/mol at 25^{0}C) and the formation of Al based oxides. Although the ANCs were processed in vacuum, as previously seen, Al will nonetheless undergo some oxidation either *in-situ*[155] or on removal from vacuum. In this case, the highly-reactive Al particles or islands were expected to form Al (core) - Al-oxide (shell) particles, which enhance the interfacial polarisation leading to high k. However, similar to many reports in the literature[16,20,22,57,59], this claim needed to be bolstered by further experimental evidence.

5.3.1 The formation of core-shell nanoparticles

In order to investigate the very first stage of the formation of the Al-nanoparticles and its influence on the dielectric properties of the ANCs, the thickness of the Al-layer had to be reduced so that the earliest stages of the particle evolution might be captured. However, achieving an Al thickness of 2 nm was extremely difficult at a deposition rate of 0.5 nm/s. Therefore a modified approach to achieve a deposition rate of 0.1 nm/s was developed, which offered greater control of the deposition of the Al-layer and thus facilitated a systematic study of the growth

of the Al-layer in the range t=2 to 20 nm, sandwiched between nylon-6 layers of nominal thickness 20 nm.

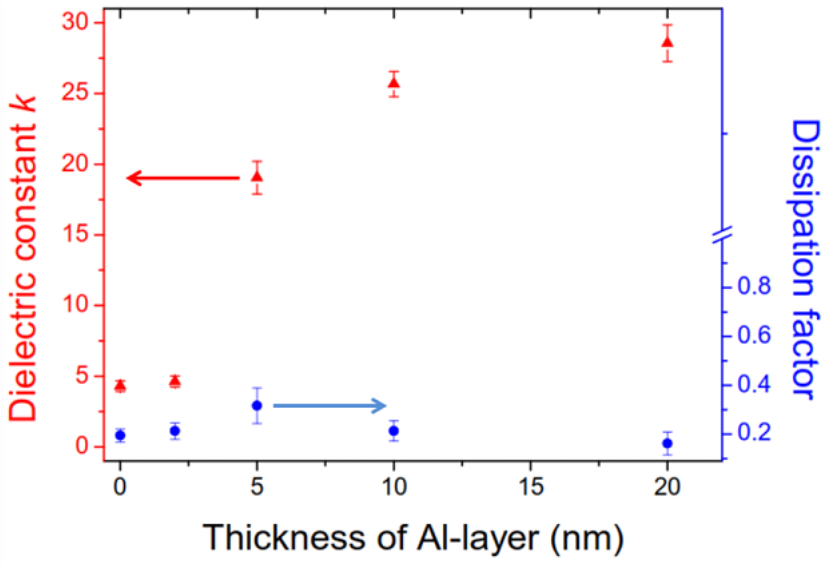


Figure 5.12: Variation of dielectric constant (▲) and dissipation factor (•) of the Al-ANCs$_{0.1}$ with thickness of the deposited Al layer at 1 kHz and 40 ^{0}C.

Figure 5.12 shows the variation of the dielectric constant (▲) and dissipation factor (•) with thickness t of deposited Al layer at 1 kHz and 40 ^{0}C. The dielectric constant increased slightly from 4.3±0.5 for nylon-6 only to 4.5±0.5 at t=2 nm and then dramatically to 19±1 at t=5 nm. For t>10 nm, k then remained in the elevated range 26-29. The dissipation factor *tan* δ, related to the dielectric loss, was in the range 0.16-0.31 for all thicknesses, and was comparable with *tan* δ~0.19 for nylon-6 alone.

ADF-STEM images of the Al-ANCs$_{0.1}$ at t=2, 5, 10 and 20 nm are shown in Figs. 5.13(a), (c), (e), and (g) respectively. The corresponding selected area electron diffraction (SAED) patterns are shown in Figs. 5.13(b), (d), (f) and (h) respectively. Al covered the pre-deposited nylon-6 surface with good uniformity to form inter-connected Al containing islands at the thinnest layer thickness of t=2 nm, suggesting that the Al wetted the nylon-6 well, and in contrast to the evaporated Ag previously described that had poor wettability and tended to "ball up" to form isolated particles[156]. The corresponding SAED pattern in

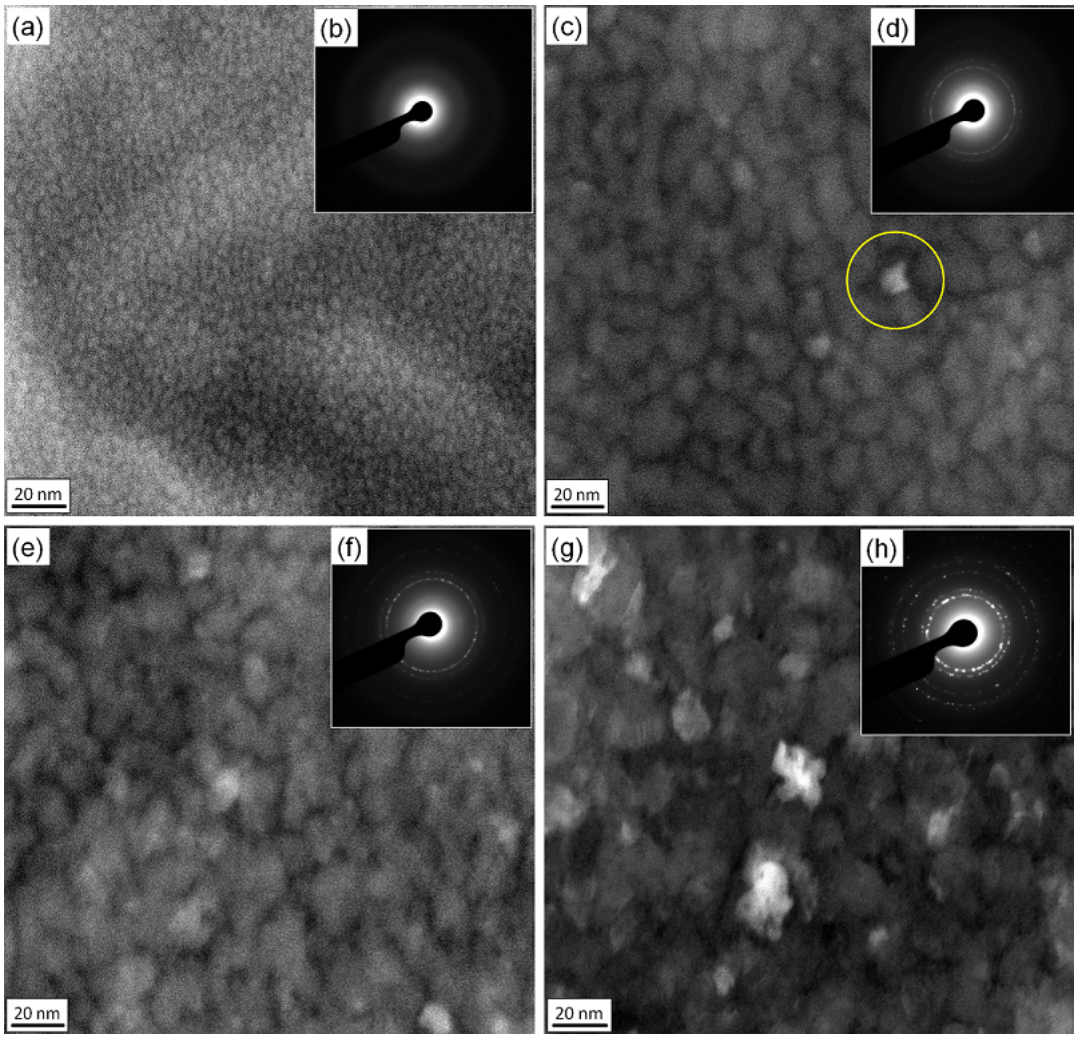


Figure 5.13: Annular dark field (ADF)-scanning transmission electron microscopy (STEM) images [(a), (c), (e), and (g)] and the corresponding selected area electron diffraction (SAED) patterns [(b), (d), (f), and (h)] of Al-ANCs$_{0.1}$ at t=2, 5, 10 and 20 nm respectively. The highlighted region in (c) is a highly diffracting, angular Al-crystal.

Fig. 5.13(b) from the brighter, ~3 nm "islands" in Fig. 5.13(a) did not show any diffraction information, suggesting the islands were essentially amorphous within the resolution of the technique. Assuming that any metallic Al would be crystalline, even at these thicknesses, it was inferred that the Al islands had been completely oxidised[155] to form a near-continuous thin layer of amorphous AlO_x. The formation of AlO_x explained the low k~4.5 at t=2 nm since bulk crystalline aluminium oxide (Al_2O_3) has k~9, and a simple rule of mixtures with v_f=0.05 (based on the relative thicknesses of nylon-6 and Al layers) suggested k~4.3 for this composite film. It is likely the oxide here is none of the bulk polymorphs of Al_2O_3 and thus may have had increased polarisability over bulk values, but in any case, the net effect of the Al based oxide on the overall dielectric behaviour was negligible.

However, k~19 at t=5 nm and v_f ~0.11 in Fig. 5.12 cannot be rationalised using any rule of mixtures or effective medium expressions since the composite dielectric constant was now higher than the dielectric constant of either AlO_x (assuming Al_2O_3) or nylon-6. In Fig. 5.13(c) at t=5 nm, the islands had grown to ~12 nm diameter and Z-contrast (based on atomic number) was more pronounced. Some regions circled in Fig. 5.13(c) were brighter still than the AlO_x islands and were more angular in morphology: these regions increased in number with increasing t as shown in Figs. 5.13(e) and 5.13(g). The angular regions appeared particularly bright due to diffraction contrast and were crystalline. The corresponding SAED patterns in Figs. 5.13(d), (f), and (h) revealed d-spacings pertaining to Al [calculated d-spacings: 0.23 nm (111), 0.20 nm (002), 0.14 nm (022), and 0.12 nm (113)], while the continuous diffraction rings in Fig. 5.13(d) suggested many randomly-oriented, tiny crystals. These crystals grew in size (probably in certain crystallographic directions) and in number as t increased, shown by the diffraction spots and now largely discontinuous rings in Fig. 5.13(h) at t=20 nm. HRTEM provided greater insight into these crystals and a HRTEM image of the

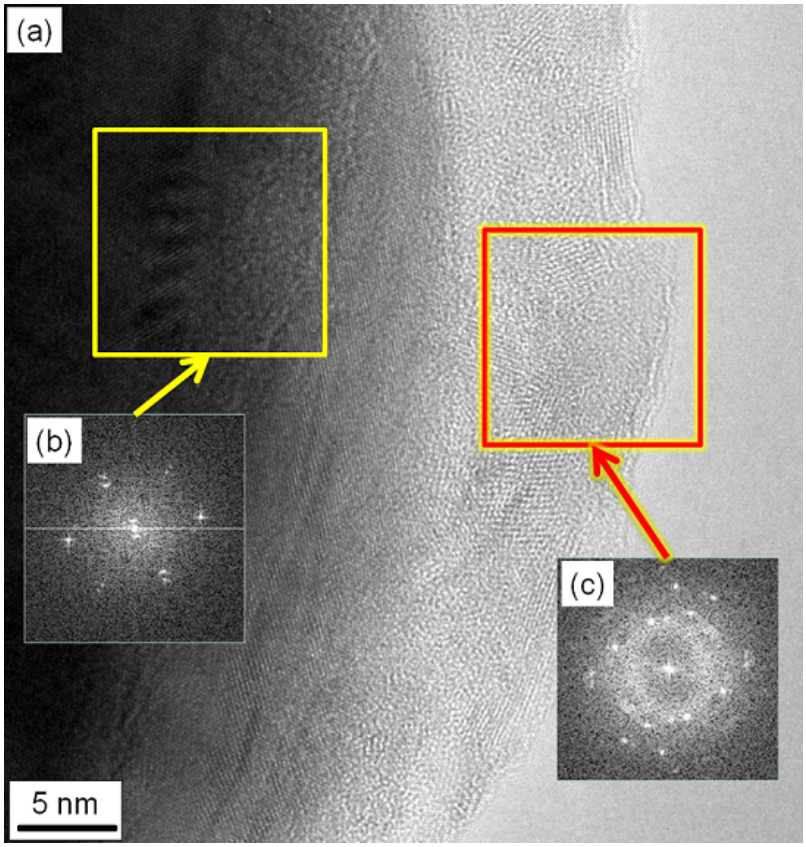


Figure 5.14: (a) HRTEM image of an Al-particle showing a crystalline core and an amorphous/semi-crystalline shell. The corresponding FFTs of the core and shell regions are shown in (b) and (c) respectively.

edge of an Al-crystal from a PNC at t=20 nm is shown in Fig. 5.14(a). There were two distinct regions - a crystalline core and an amorphous/semi-crystalline shell whose corresponding fast Fourier transforms (FFTs) are shown in Figs. 5.14(b) and (c) respectively. The FFT from the centre of the Al-particle in Fig. 5.14(b) had spots corresponding to (111) and (002) Al lattice planes. The presence of *both* Al and its oxide in these particles was confirmed further by XPS data. A curve-fitted X-ray photoelectron spectrum from the Al-ANC$_{0.1}$ for t=20 nm is shown in Fig. 5.15 with peaks at 74.4 and 71.9 eV, corresponding to the 2p peaks of Al_2O_3 and Al-metal respectively[148]. However, confirmation of any amorphous character in the Al-oxide shell with regions of only short-range crystalline order required resolution of its structure and chemistry on the nano-scale.

Figure 5.16 shows a HRTEM image of the oxide shell and a small portion of the

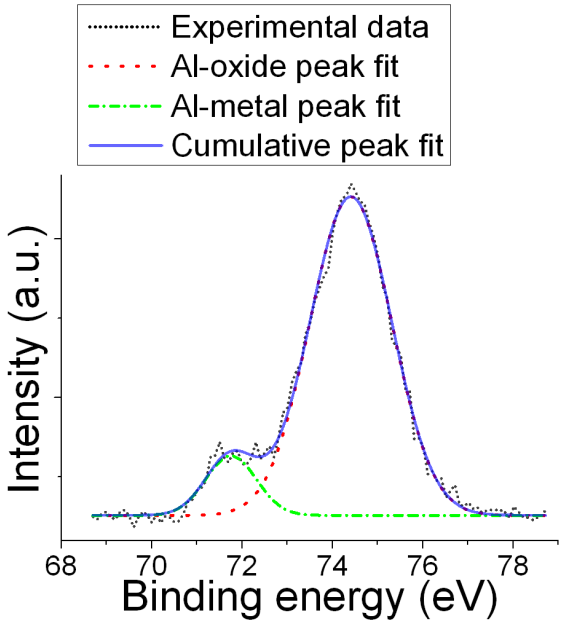


Figure 5.15: X-ray photoelectron spectrum of a Al-ANC$_{0.1}$ with t=20 nm. Curve fitting of the spectra showed two peaks at 74.4 and 71.9 eV.

Al-core. The superimposed line AA' in Fig. 5.16 is an approximate, indicative boundary between the Al-metal (core) and Al-oxide (shell). The shell comprised short-range crystalline order and amorphous regions. The highly-defective and strained nature of the oxide shell is highlighted in box B in Fig. 5.16 where the d-spacing varied from ~0.3 to ~0.16 nm in the y direction, and was inconsistent with either Al or Al_2O_3, suggesting both high residual strain associated with small radius of curvature of the particle and that the Al-oxide in the shell does not conform to Al_2O_3 (hence "AlO_x").

Based on these detailed observations, the enhanced interfacial polarisation in the PNCs for t≥5 nm when the core-shell structure first developed may be understood to involve charge separation in the non-stoichiometric AlO_x because of the high concentration of lattice defects and relatively mobile charge carriers[103,104,150,152]. The oxide-shell consisting of defects (such as vacancies, interstitials and impurity centres[157]), the electron-rich Al-core and certain ionised species in the nylon-6 are potential sources of charge carriers (or space charges) that might gain mobility on the application of an external electric field. Critically, the defects in the AlO_x

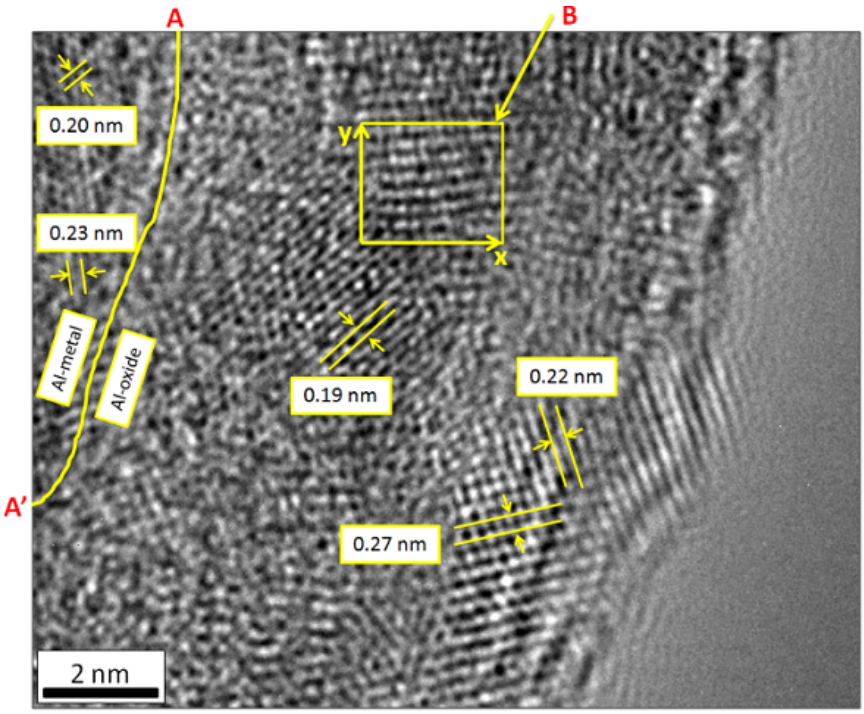


Figure 5.16: HRTEM image of the Al-oxide (shell) and a small portion of the Al-metal (core). The superimposed line AA' is an approximate, indicative boundary between the Al-metal (core) and Al-oxide (shell). The highly-defective and strained nature of the oxide shell is highlighted in box B.

shell will also create intermediate or defect energy E_d levels between the Fermi level E_F of the electron rich Al-core and the conduction band edge CB of the nylon-6 matrix - between which the charge carriers are relatively mobile [158]. A schematic representation of the energy levels is shown in Fig. 5.17.

This mobility facilitates charge separation [150] to the nylon-6/AlO_x and Al/AlO_x interfaces leading to piling up of the charges, which in turn may induce an image charge force that consists of electrically opposite charges as shown in Fig. 5.17. These interfaces enclose a region that can be called an "interphase" [104] which is chemically and structurally distinct from Al, Al_2O_3 or nylon-6. The presence of a new interface - Al/AlO_x, which was absent in Al-ANCs$_{0.1}$ at t=2 nm, acted as an additional region for charge accumulation. Charge accumulation may also take place by "trapping" of charge carriers [157] in the defects of the oxide-shell, leading to an increase in the charge-concentration around the particles, as previously

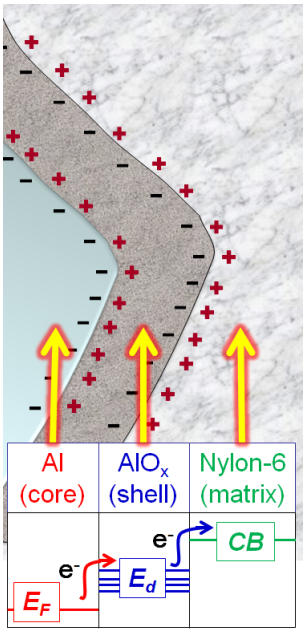


Figure 5.17: Schematic of the charge separation at the nylon-6/AlO_x and Al/AlO_x interfaces, and charge transfer between the energy levels - E_F,E_d and CB.

observed for Ge (core)-GeO_2 (shell) particles[107]. The accumulation of these mutually opposing charges at the interfaces leads to interfacial polarisation (also known as space charge or MWS polarisation). When the electric field is reversed, the charges rearrange accordingly but take a certain amount of time. So in the presence of an alternating electric field, the whole process involving tunnelling, trapping/detrapping, migration, induction and rearrangement of charges is out-of-phase with respect to the applied electric field, and this type of polarisation is predominantly effective at low frequencies ($\leq$ 1 kHz, which is the frequency at which dielectric characterisation of the PNCs was carried out).

The increase in angularity of the core-shell particles compared with AlO_x only particles also increased the surface area to volume ratio and therefore may have also contributed to an enhanced surface charge storage capacity. Any opposition to the transfer and rearrangement of the charges that results in the dissipation of heat while altering the direction of the applied electric field contributes to the dielectric loss, but in these cases, differences in loss behaviour could not be resolved, and were low at all thicknesses and controlled by the intrinsic loss of

the majority nylon-6 matrix.

The dramatic jump in k from ~4.5 to ~19 in Fig. 5.12 occurred only when a significant fraction of core-shell particles formed, and the subsequent less dramatic rise for t=5 nm to t=20 nm arose from the more gradual increase in the number fraction of core-shell particles. A cross-sectional schematic representation of the growth of the Al-layer on nylon-6 with an increase in t is shown in Fig. 5.18.

5.4 Conclusions

Dielectric materials consisting of Al or Ag in nylon-6 films were fabricated by an alternate vacuum deposition technique. Electron microscopy studies revealed that the deposition of Al led to the formation of Al (core)-AlO_x (shell) nanoparticles, a branched nylon-6 matrix with fine-scale AlO_x "islands". On the other hand, because Ag was much less-reactive with ambient gases (especially oxygen) and wetted nylon-6 less well, it formed well-separated Ag-nanoparticles. STEM proved to be a powerful tool to study the growth of Al on nylon-6 and the formation of Al (core)-AlO_x(shell) particles, which was critical in understanding the enhanced dielectric behaviour of the PNCs. A detailed study on the structure and chemistry of core-shell particles on a nano-scale revealed a highly-defective, strained and non-stoichiometric Al-oxide shell. The high-k behaviour was attributed to the various physical phenomena that are promoted in the presence of this type of core-shell particles, based on the idea of enhanced interfacial polarisation. The effect of interfacial polarisation was less pronounced in Ag-ANCs due to the absence of relatively polarisable core-shell particles, and hence $k_{Ag-ANCs}<k_{Al-ANCs}$. This chapter upheld the utility and reproducibility of alternate deposition as a fabrication technique for PNCs, and may point the way to a larger scale processing based on already available "web" processing of polymers, if sufficient fine scale control of deposition rates could be achieved.

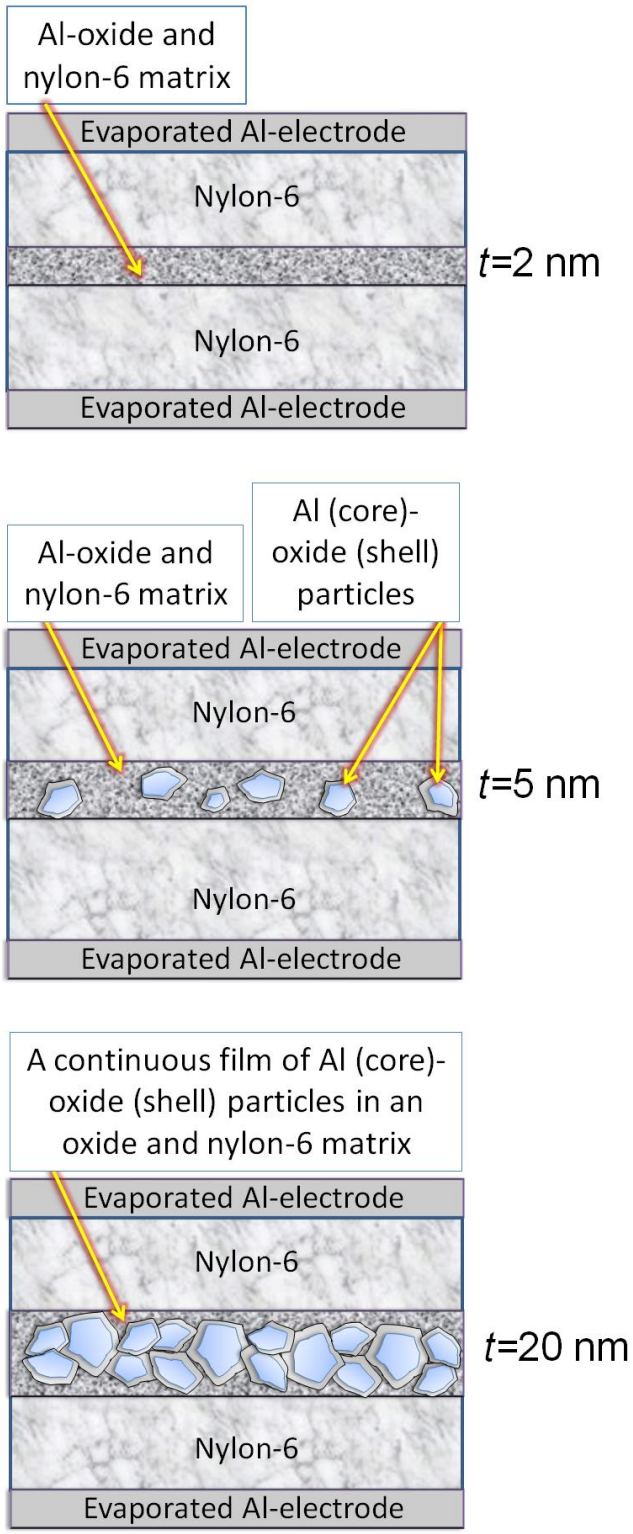


Figure 5.18: A cross-sectional schematic representation of the growth of the Al-layer on nylon-6 with an increase in Al deposited thickness t.

Chapter 6

Engineering nanocomposite capacitors consisting of Ti, Ag+Ti and nylon-6

6.1 Introduction

This chapter builds on the vacuum deposition of PNCs described in the previous chapter to investigate if rational choices of materials and processing approaches can be used to engineer the structure of the PNCs on a nano-scale in order to boost their effective dielectric properties. The previous chapter employed an alternate deposition technique to produce PNCs containing metal (core)-oxide (shell) particles in a polymer matrix by controlling the thickness of the deposited metal layer. Since the dielectric constant of the shell affects the bulk dielectric properties[88], and a semiconducting shell is suggested to enhance interfacial polarisation[150], the choice of the metal that undergoes oxidation to form the oxide-shell is crucial. Based on the above therefore a rational choice of metal would be a highly-reactive metal that naturally forms a semiconducting, high-k oxide-shell. Titanium is one such reactive metals where TiO_2 is, in bulk at least,

semiconducting and highly-polarisable with k of amorphous TiO_2 and crystalline TiO_2 (anatase and rutile, both tetragonal) in the range 12-114[48,159–163].

In the alternately-deposited dielectric films explored so far, the overall or effective k of the tri-layer material between the capacitor plates was likely limited because the more-polarisable layer containing core-shell nanoparticles was sandwiched between low-k polymer layers. Complete removal of these polymer layers to enhance capacitance is clearly not viable because they are needed to ensure no short-circuiting of the capacitor should the Al-electrodes come in contact with the core-shell rich layer; nonetheless, the thickness of the nylon-6 layers should be minimised.

Other approaches to enhance the effective k of the dielectric material would be to replace some or all of the low-k polymer with a high-k polymer such as a ferroelectric polymer[48]. However, the cost and particularly the vacuum processibilty of this type of polymers is restrictive, with changes in the polymer composition and structure on evaporation-condensation undermining their inherent polarisability.

An alternative to reducing the undermining effect of the poor dielectric response of the nylon-6 layer explored in this chapter was instead to incorporate a *conducting* secondary phase into the polymer. If the volume fraction of the metallic filler can be controlled, there might be an additional and virtuous contribution to the effective k of the device via the near-percolation micro-capacitor network effect[35] previously seen for the Ag in nylon-6 films in the previous chapter.

In this approach, the volume fraction of the conducting phase needs to be well-controlled and just below the percolation threshold, not least to restrict losses to an acceptable level, and the process of incorporation of the conducting phase should be compatible with the alternate deposition technique so that devices can be built in a single operation. Although relatively cheap conductive fillers such as carbon black[164], Ni[165], and Mo[35] could be used, the experience already gained by the deposition of Ag in the previous chapter encouraged the choice of

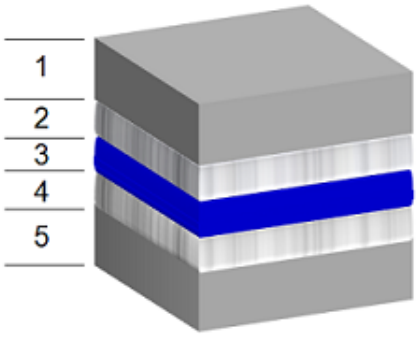
Ag.

This chapter deals with the fabrication and study of alternately deposited nanocomposite (ANC) films consisting of Ti in nylon-6, and then both Ti and Ag in nylon-6. The dielectric properties are studied as a function of the Ti deposition rate and layer thickness. STEM, SAED and HRTEM are again used extensively to study the structure and chemistry of the resulting nanocomposite films. The dielectric properties are correlated to the microstructure and are explained with the help of schematics that suggest the likely nano-arrangement of Ti and Ti+Ag based particles in the nylon-6 matrix.

6.2 Experimental Procedure

6.2.1 Fabrication

All experimental approaches were similar to those already described in Chapter 5 and only the significant additions or modifications are mentioned here.



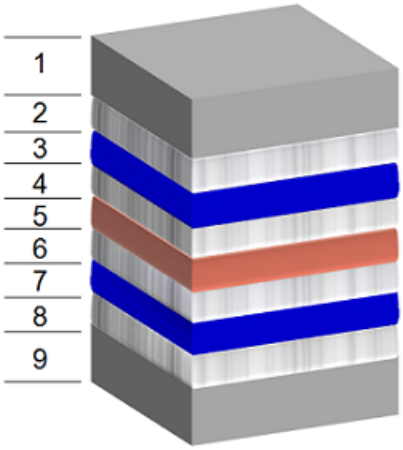
Layer	Material	t (nm)	$\dot{t}$ (nm/s)
1	Al (electrode)	40	0.5
2	Nylon-6	Variable	0.1
3	Ti	Variable	Variable
4	Nylon-6	Variable	0.1
5	Al (electrode)	40	0.5

Figure 6.1: A schematic of alternate layers of metal and polymer.

Ti and Nylon-6 based capacitors were fabricated by sequential deposition of five individual layers of the metal(s) and nylon-6 in the Edwards Auto 306 Cryo evaporator as previously described. Titanium wire (99.7% pure, Alfa Aesar, 0.25 mm diameter) and nylon-6 (Aldrich) were thermally evaporated onto a glass slide, alternatively using two different W boats. The deposition rate of nylon-6 $\dot{t}_{Ny}$ was maintained at 0.1 nm/s in all experiments. A schematic of the five alternate

layers formed during evaporation is shown in Fig. 6.1. The top and bottom (1st and 5th) layers of Al (40 nm each) formed the electrodes of a simple parallel-plate capacitor. The growth of Ti (3rd layer), sandwiched between the nylon-6 layers (2nd and 4th), was studied at various thicknesses. These samples are referred to as $Ti_{\dot{t}}$-Ny_t where the subscripts $\dot{t}$ and t are variables which denote the deposition rate of Ti and the final thickness of the nylon-6 layer respectively.

Ag, Ti and nylon-6 based capacitors were fabricated by tandem deposition of nine individual layers as shown in the Fig. 6.2. These samples are referred to as Ag-$Ti_{\dot{t}}$-Ny_t.



Layer	Material	t (nm)	$\dot{t}$ (nm/s)
1	Al (electrode)	40	0.5
2	Nylon-6	Variable	0.1
3	Ag	5	0.1
4	Nylon-6	Variable	0.1
5	Ti	Variable	Variable
6	Nylon-6	Variable	0.1
7	Ag	5	0.1
8	Nylon-6	Variable	0.1
9	Al (electrode)	40	0.5

Figure 6.2: A schematic of alternate layers of metal and polymer.

6.3 Results and discussion

Figure 6.3 shows the variation of dielectric constant (▲) and dissipation factor (•) of the $Ti_{0.5}$-Ny_{20} ANCs as a function of thickness t of the deposited Ti layer at 1 kHz and 40 ^{0}C. The dielectric constant increased dramatically from ~4 for nylon-6 only to ~26 at t=5 nm and then to ~38 at t=10 nm. The dissipation factor $tan\ \delta$ increased slightly from ~0.19 for nylon-6 only to ~0.32 for both Ti-ANCs. Both k and $tan\ \delta$ of Ti-ANCs were higher than those of Al-ANCs discussed in the previous chapter at all thicknesses of the metal layer, presumably due to the

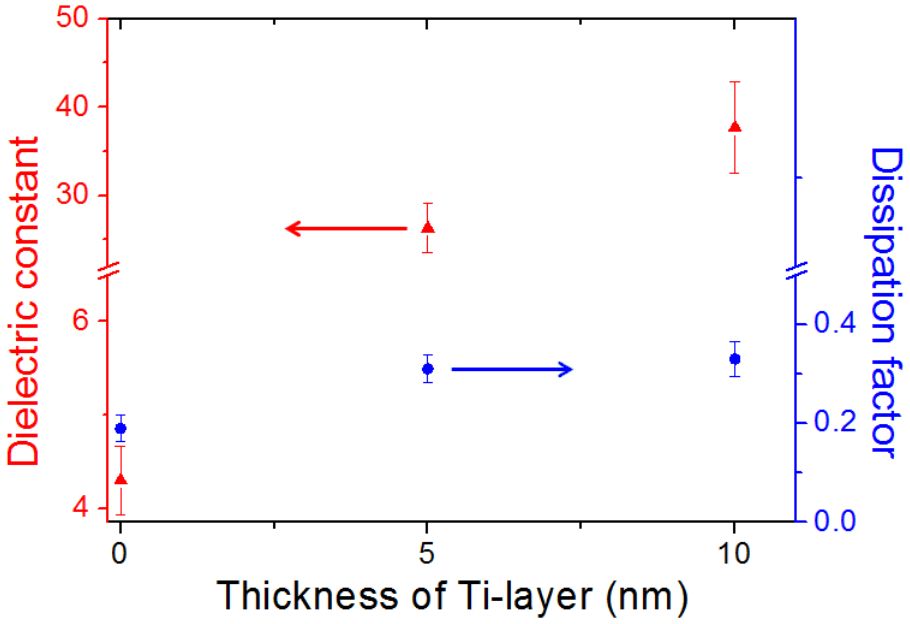


Figure 6.3: Variation of dielectric constant (▲) and dissipation factor (●) of the $Ti_{0.5}$-Ny_{20} ANCs with thickness of the deposited Ti layer at 1 kHz and 40 ^{0}C.

formation of a semiconducting and higher k Ti-based oxide.

Annular dark field (ADF)-STEM images of the $Ti_{0.5}$-Ny_{20} ANCs at t=5 and 10 nm are shown in Figs. 6.4(a) and (b) respectively. The corresponding selected area electron diffraction (SAED) patterns are shown in Figs. 6.4(c) and (d) respectively. The rings in the SAED patterns were more apparent in the corresponding enhanced images shown in Figs. 6.4(e) and (f). In general, Ti showed "wetting" properties similar to Al and covered the nylon-6 surface with good uniformity as seen in Figs. 6.4(a) and (b). The SAED patterns in Figs. 6.4(c) and (d) at t=5 and 10 nm showed diffraction rings due to crystalline phases, highlighted in Fig. 6.4(a) and (b). The rings were continuous and relatively thick, suggesting the presence of many randomly oriented, tiny crystals, and resulted in a wide range of estimated d-spacings. The measured d-spacing from the first ring in Fig. 6.4(f) was in the range 0.35-0.36 nm and is suggested to correspond to the (101) plane of TiO_2-anatase with a d-spacing of ~0.351 nm[166] rather than the (110) plane of TiO_2-rutile with a d-spacing of ~0.325 nm[167]. The measured d-spacings from the second and third rings were in the range 0.24-0.21 nm and 0.15-0.13 nm re-

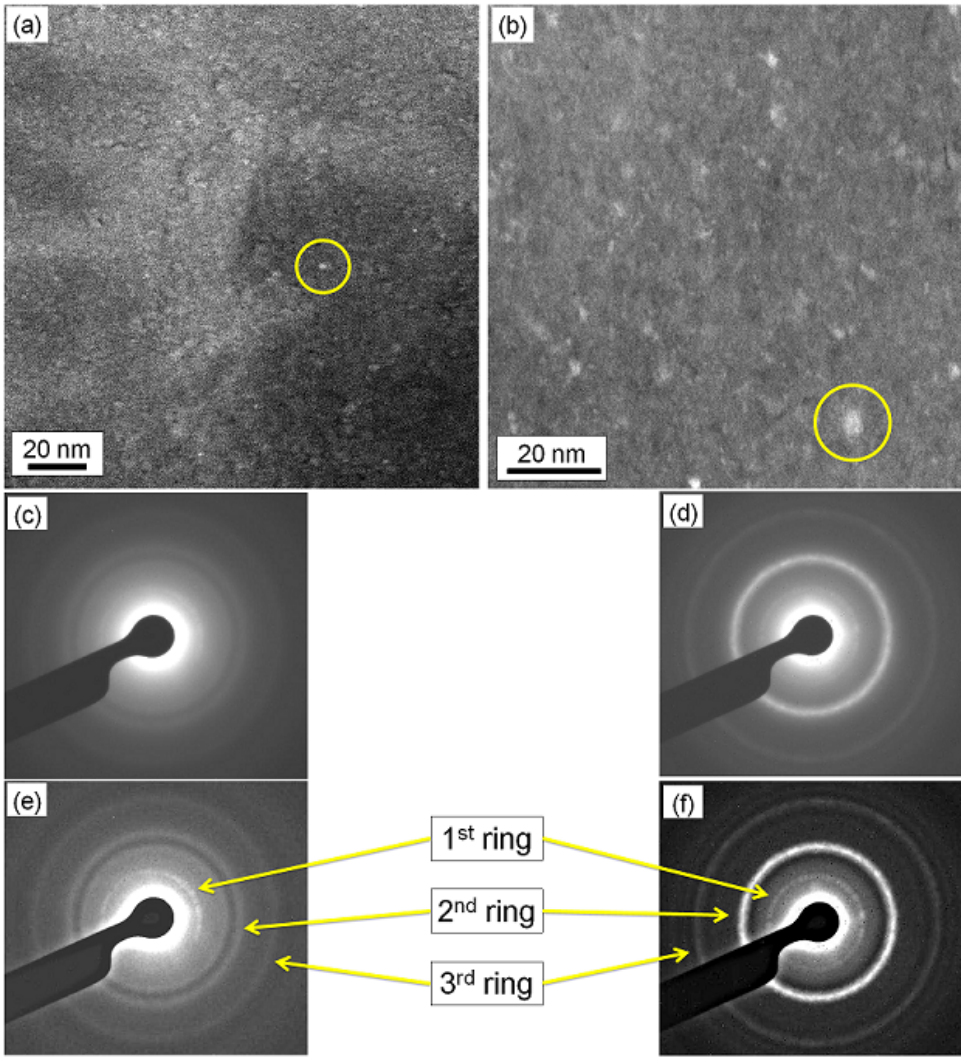


Figure 6.4: ADF-STEM images [(a) and (b)] and the corresponding SAED patterns [(c) and (d)] of $Ti_{0.5}$-Ny_{20} ANCs at t=5 and 10 nm respectively. (e) and (f) are the enhanced images of the SAED patterns, (c) and (d). The highlighted regions in (a) and (b) are highly diffracting Ti-metal or Ti-oxide crystals.

spectively, and may relate to anatase [reported d-spacings[168]: 0.242 nm (103), 0.237 nm (004), 0.187 nm (200), 0.169 nm (105), 0.166 nm (211), 0.148 nm (204), 0.136 nm (116), 0.134 nm (220), and 0.126 nm (215)], and also to Ti [reported d-spacings[169]: 0.256 nm $(01\bar{1}0)$, 0.234 nm (0002), 0.224 nm $(01\bar{1}1)$, 0.173 nm $(01\bar{1}2)$, 0.148 nm $(11\bar{2}0)$, 0.141 nm $(11\bar{2}1)$, 0.133 $(01\bar{1}3)$, 0.128 $(02\bar{2}0)$, and 0.125 nm $(11\bar{2}2)$]. The overlapping of the diffraction rings limited any further meaningful analysis of the SAED patterns that might yield information pertaining to the chemistry and the structure of the crystals. Nonetheless, from this initial

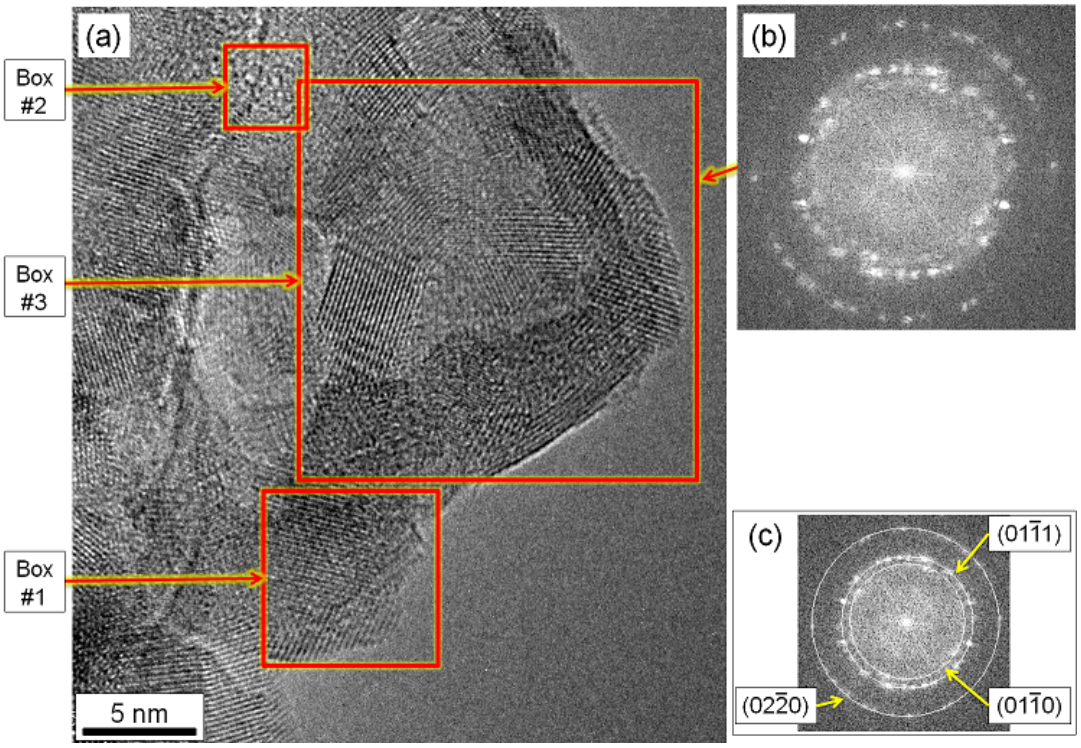


Figure 6.5: (a) HRTEM image of polycrystalline "Ti" nanoparticles, (b) the corresponding FFT from the highlighted square region, and (c) analysed FFT showing the three circles along which most of the spots lie.

information, the formation of both a Ti-based oxide and some residual metallic Ti at both t=5 and 10 nm was suggested, and therefore qualitatively similar to Al based ANCs.

A HRTEM image of Ti-based nanoparticles and the corresponding FFT are shown in Figs. 6.5(a) and (b) respectively. Figure 6.5(a) shows a cluster of polycrystalline nanoparticles and small amorphous regions, highlighted in the boxes #1 and #2 respectively. The resolvable crystallographic planes terminated at the surface of some of the nanoparticles protruding into vacuum, highlighted in box #3, with no clear evidence of significant amorphous surface oxide. A majority of the spots in the FFT in Fig. 6.5(b) were along three circles indicated in Fig. 6.5(c). These spots corresponded to (01$\bar{1}$0), (01$\bar{1}$1), and (02$\bar{2}$0) Ti lattice planes. So the polycrystalline nanoparticles were predominantly comprised of Ti. However, a FFT from a small crystalline region of ~60 nm^2 (box #1) shown in Fig. 6.6(a)

had spots corresponding to (004), (200), and (211) anatase lattice planes (the corresponding measured d-spacings are 0.235 nm, 0.190 nm and 0.164 nm respectively). A magnification of the FFT in Fig. 6.6(c) is shown in Fig. 6.6(d), showing two spots corresponding to the $(01\bar{1}1)$ and (103) lattice planes of Ti and anatase respectively. These findings further supported the previous SAED information for the co-existence of Ti and anatase in the ANCs. The Ti-nanoparticles that appeared to have metallic Ti-crystalline planes terminating at the surface suggested that these Ti-nanoparticles were generally well-encapsulated in the nylon-6 and did not oxidise excessively in the microscope column when the nylon-6 was ablated by the electron beam. However, the occurrence of metallic Ti-nanoparticles in the nylon-6 was comparatively rare, and most Ti-rich particles were either oxides or showed significant surface oxide formation.

Figure 6.7(a) is a HRTEM image of a Ti-nanoparticle protruding into the vacuum. The corresponding FFT from the highlighted region is shown in Fig. 6.7(b). An analysis of the FFT in Fig. 6.7(b) showed that most of the spots were traced by three circles as shown in Fig. 6.7(c) and corresponded to $(01\bar{1}0)$, $(01\bar{1}1)$, and $(02\bar{2}0)$ Ti lattice planes. Unlike the nanoparticle in Fig. 6.5(a), the Ti-nanoparticle in Fig. 6.7(a) showed amorphous regions near its edge/surface. Such Ti-nanoparticles were considered qualitatively similar to the Al-nanoparticles that oxidised to form an oxide-shell around the metal-core in the previous chapter. A HRTEM image of one such nanoparticle taken from a region near its edge is shown in Fig. 6.8. The measured d-spacings from the crystalline region were 0.25 nm and 0.22 nm and corresponded to $(01\bar{1}0)$ and $(01\bar{1}1)$ lattice planes of Ti respectively. The superimposed line AA' is an approximate, indicative boundary between the Ti-metal (core) and Ti-oxide (shell). A typical highly-defective nanostructure in the shell region is highlighted in box B, in the region where the structure makes a transition from the crystalline Ti-metal to the amorphous Ti-oxide.

Figure 6.9 is a HRTEM image of another Ti(core)-oxide (shell) nanoparticle with

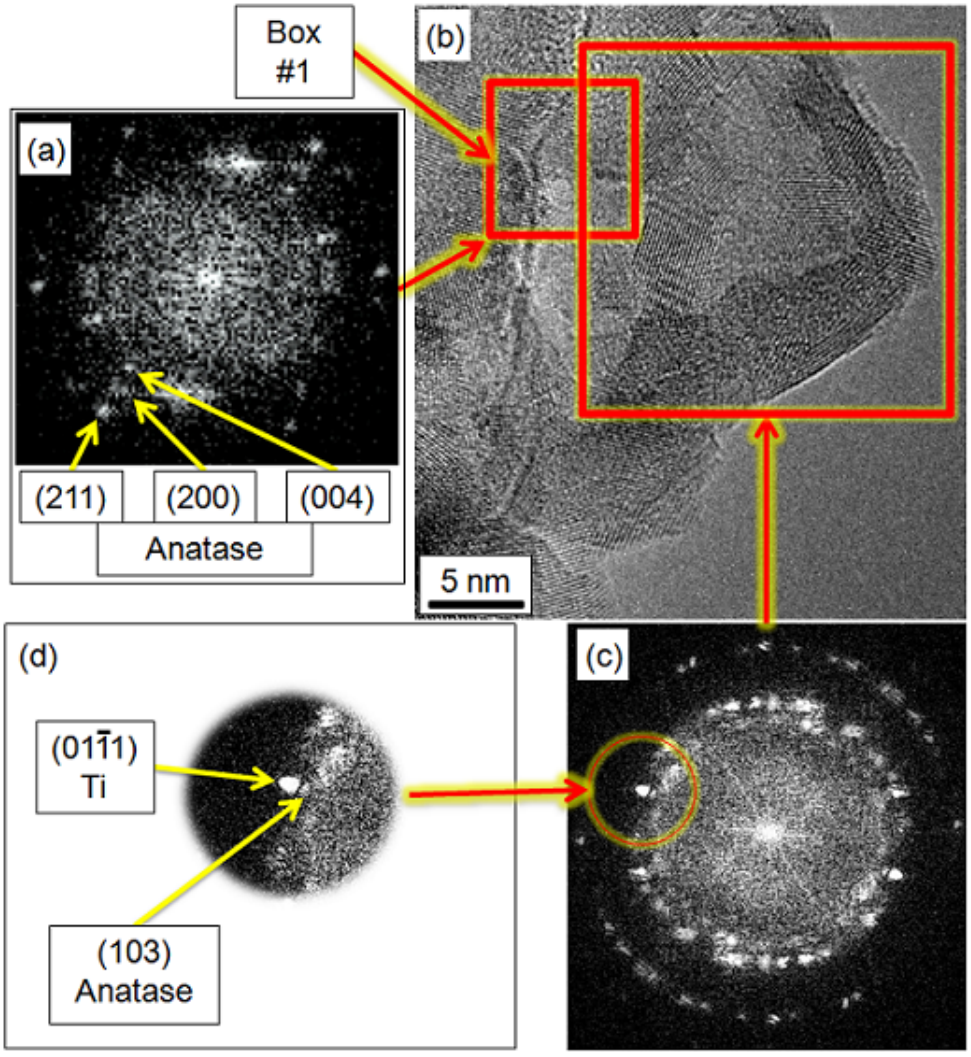


Figure 6.6: (a) and (c) are FFTs corresponding to the highlighted square regions in the HRTEM image of polycrystalline "Ti" nanoparticles, (b). A circular region of the FFT in (c) is magnified in (d).

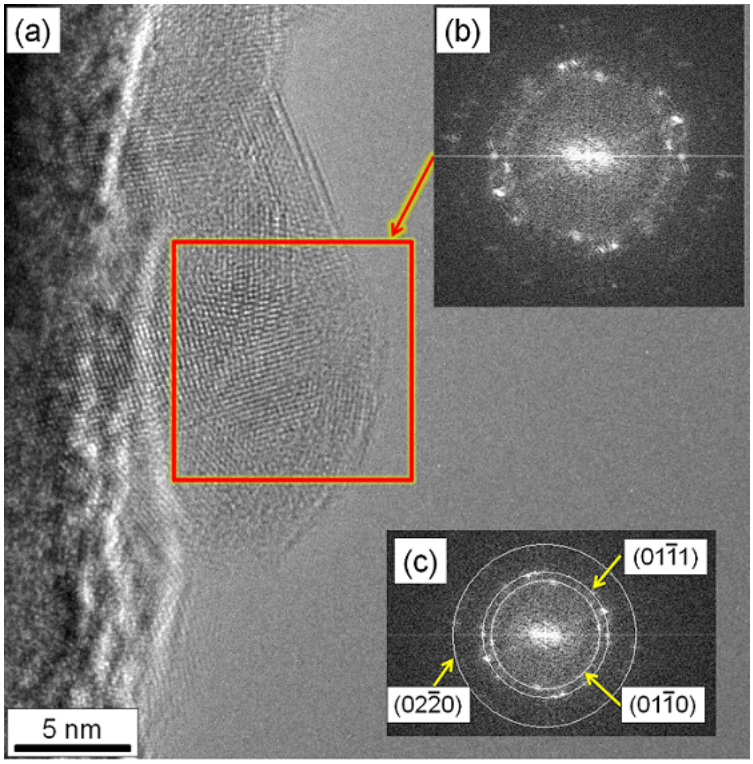


Figure 6.7: (a) HRTEM image of a Ti-nanoparticle protruding into the vacuum, (b) the corresponding FFT from the highlighted square region, and (c) analysed FFT showing the three circles along which most of the spots lie.

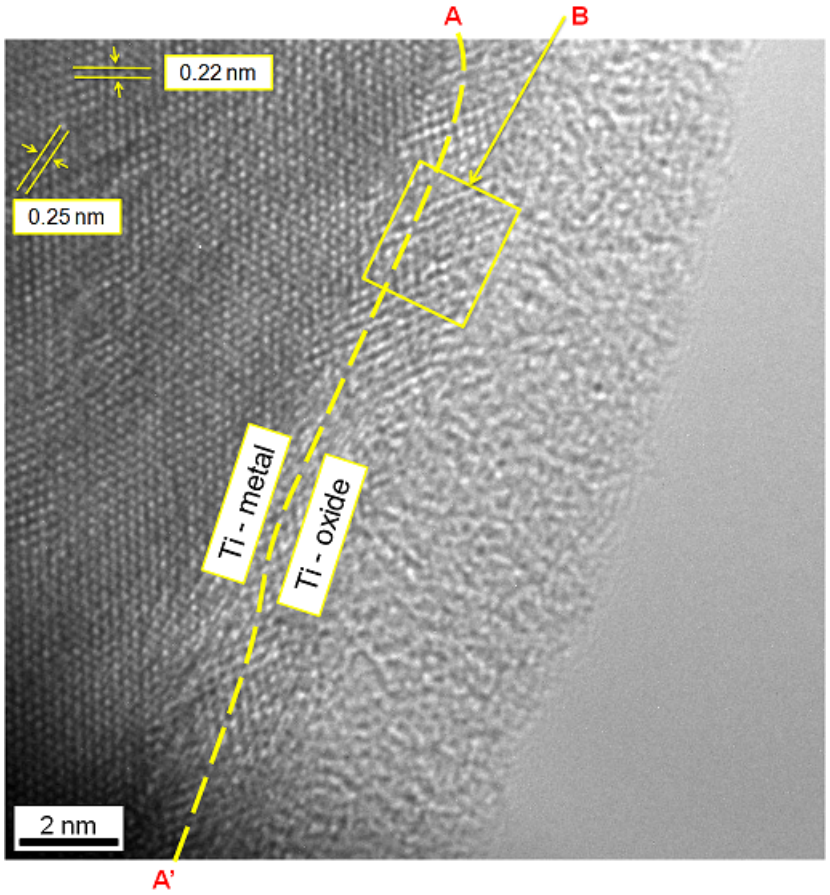


Figure 6.8: HRTEM image of a Ti-nanoparticle showing a Ti-oxide (shell) and a Ti-metal (core). The superimposed line AA' is an approximate, indicative boundary between the Ti-metal (core) and Ti-oxide (shell). A highly-defective nanostructure, highlighted in box B, coincided with the indicative boundary, where the phase-transition takes place from crystalline metal to amorphous oxide.

again a superimposed line AA' as an approximate, indicative boundary between the metal and its oxide shell. In this case, there were regions of short-range order (for example in the highlighted box B) within the otherwise defective and amorphous-like oxide-shell. Since the Ti-oxide shell is qualitatively similar to the AlO_x shell observed in the previous chapter, Ti-oxide was likely to be non-stoichiometric and is hence referred to as TiO_x.

Taking the microscopy-based observations as a whole, with typical examples shown in Figs. 6.6, 6.8, and 6.9, suggested that some metallic Ti nanoparticles co-existed with crystalline anatase nanoparticles, and some Ti-nanoparticles had metallic cores enclosed in oxide-shells that comprised amorphous, highly-defective and semi-crystalline regions.

Returning to the high k behaviour in Fig. 6.3, once Ti was introduced into the polymer, the elevation in k cannot be attributed to the presence of a volume fraction of anatase with k=47[48] through a law of mixtures approach, because in order to attain k~38 under these conditions, the volume fraction of anatase would have to be ~0.8, whereas it was (assuming all Ti transformed to anatase) ~0.2 at t=10 nm. Even when the full range of reported dielectric constants for anatase and amorphous Ti-oxide are considered[48,159–162] and which lie in the range 40-48 and 12-18 respectively, there is no support for a simple mixing rule to explain the measured dielectric constant. Therefore, and consistent with Al-ANC behaviour, the enhancement in k in Fig. 6.3 was ascribed again to the presence of relatively polarisable Ti (core)-oxide (shell) nanoparticles.

The various physical phenomena that might be promoted due to core-shell nanoparticles have already been described in section 5.3.1 for Al/AlO_x core-shell nanoparticles. In addition to these, a defective semiconducting Ti-based oxide may contain more discrete energy levels than a more insulating oxide such as those based on Al-oxide, between which charge carriers can move between the extremes of the conducting (Ti) and insulating (nylon-6) phases.

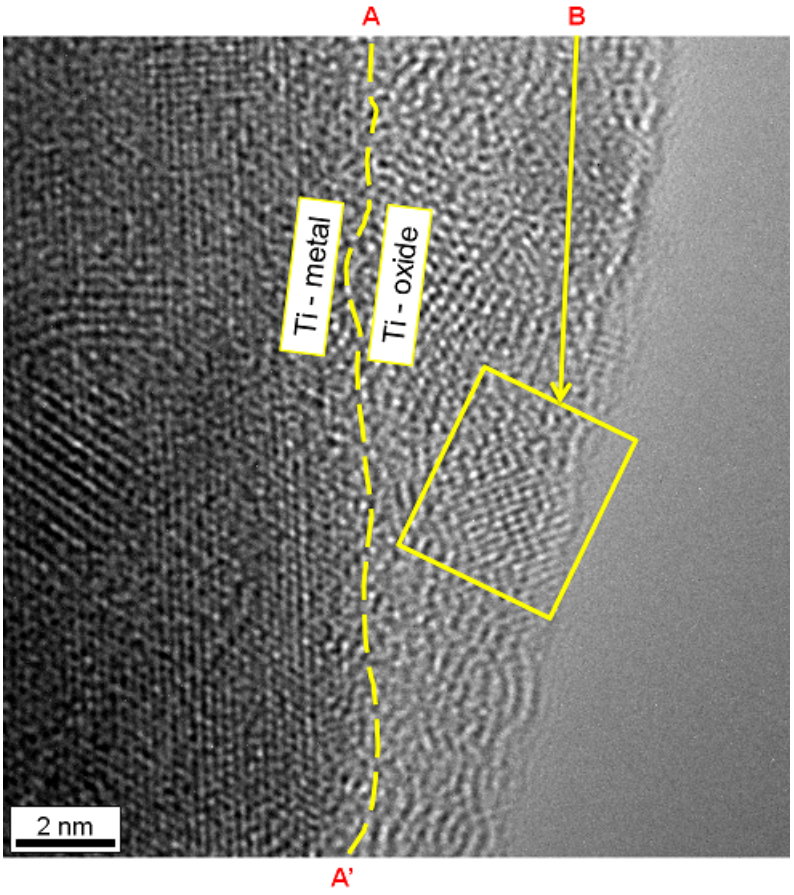


Figure 6.9: HRTEM image of the edge of a Ti (core)-oxide (shell) nanoparticle. The superimposed line AA' is an approximate, indicative boundary between the Ti-metal (core) and Ti-oxide (shell). A region of short-range order in the amorphous oxide shell is highlighted in box B.

6.3.1 Effect of adding Ag nanoparticles and the Ti deposition rate

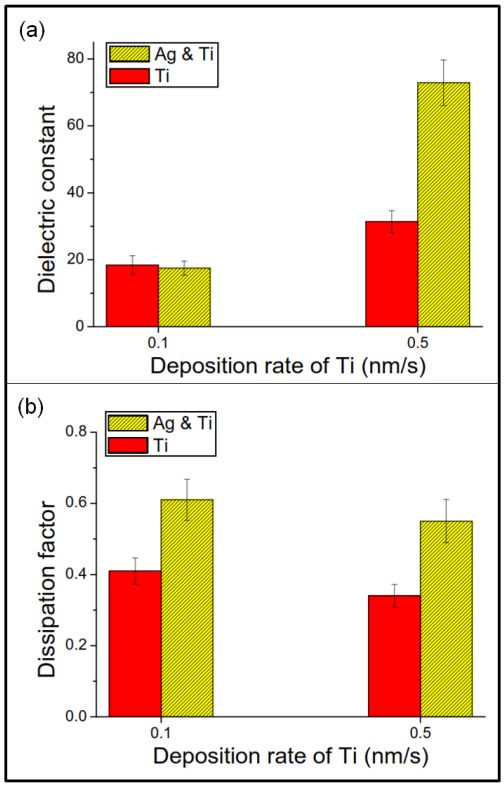


Figure 6.10: The variation of (a) dielectric constant and (b) dissipation factor of Ti-ANCs and Ag-Ti-ANCs with deposition rate of Ti at 1 kHz and 40 ^{0}C. The thicknesses of the deposited Ti, nylon-6 and Ag layers in all the ANCs were 10, 10 and 5 nm respectively.

Figure 6.10 shows the variation of (a) dielectric constant and (b) dissipation factor of Ti-ANCs and Ag-Ti-ANCs as a function of the deposition rate of Ti at 1 kHz and 40 ^{0}C. The thickesses of the deposited Ti, nylon-6 and Ag layers in all the ANCs were 10, 10 and 5 nm respectively. Ti-ANCs at $\dot{t}_{Ti}$=0.5 nm/s gave k~31 and was significantly higher than k~18.5 for Ti-ANCs at $\dot{t}_{Ti}$=0.1 nm/s, although the dissipation factor was similar in the range 0.34-0.41.

Ag-Ti-ANCs at $\dot{t}_{Ti}$=0.1 nm/s gave k~17.5, which was comparable with k~18.5 of Ti-ANCs at the same $\dot{t}_{Ti}$. However, there was a dramatic increase to k~73 for Ag-Ti-ANCs at $\dot{t}_{Ti}$=0.5 nm/s which represented a 2.5 times increase over Ti-ANCs at the same $\dot{t}_{Ti}$. However, as might be expected with an increased metallic com-

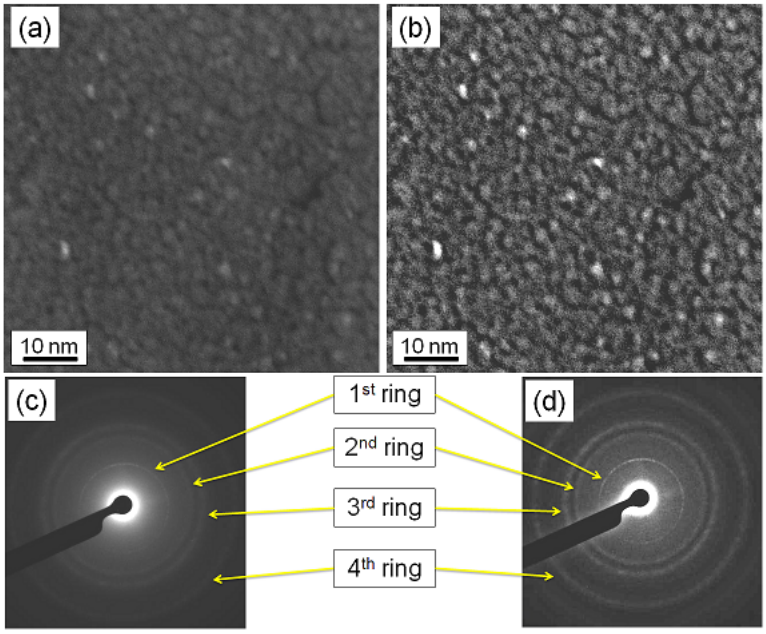


Figure 6.11: (a) ADF-STEM image and (c) the corresponding SAED pattern of a $Ti_{0.1}$-Ny_{10} ANC film; (b) and (d) are the enhanced images of (a) and (c) respectively.

Ring #	***d*-spacing (nm)**	**Anatase (hkl)**	**Ti (hkil)**
1	~0.36	(101)	X
2	0.23-0.25	(103), (004), (112)	$(01\bar{1}0)$
3	0.20-0.22	(200)	$(01\bar{1}1)$
4	0.14-0.15	(211), (105)	$(11\bar{2}0)$

Table 6.1: The measured d-spacings from the SAED pattern in Fig. 6.11 and the closest matches from anatase and Ti.

ponent, both Ag-Ti-ANCs were more "lossy" with $tan\ \delta$ approximately doubling to lie the range 0.55-0.61.

Figures 6.11(a) and (c) show the ADF-STEM image and the corresponding SAED pattern of a $Ti_{0.1}$-Ny_{10} ANC film respectively. Figures 6.11(b) and (d) are the enhanced images of Figs. 6.11(a) and (c) respectively. The ADF-STEM image shows bright Ti-islands in a dark nylon-6 matrix. The measured d-spacings from the SAED and the closest matches are shown in the Table 6.1. Therefore, once again, both anatase-like TiO_x and crystalline Ti were present in $Ti_{0.1}$-Ny_{10}-ANCs. Figures 6.12(a) and (b) show the SAED patterns of Ti-ANCs at $\dot{t}_{Ti}$=0.5 and

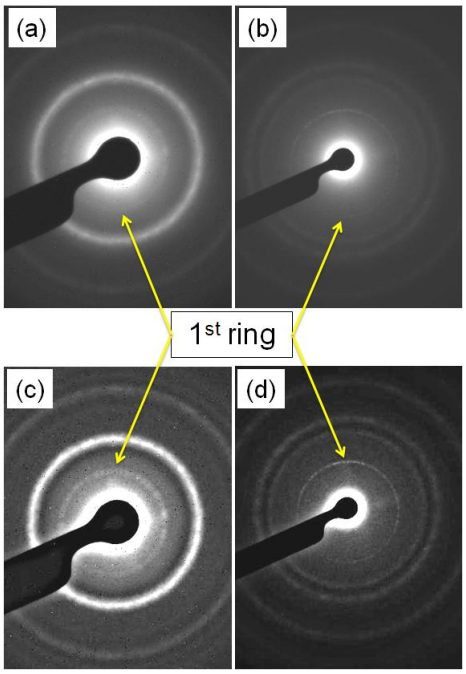


Figure 6.12: SAED patterns of Ti-ANCs at $\dot{t}_{Ti}$= (a) 0.5 nm/s and (b) 0.1 nm/s. (c) and (d) are the corresponding enhanced images of (a) and (b) respectively.

0.1 nm/s respectively, and Figs. 6.12(c) and (d) are the corresponding enhanced images. The first diffraction ring in Fig. 6.12(a) was wider than that in Fig. 6.12(b), suggesting that the TiO_x crystals formed at $\dot{t}_{Ti}$=0.1 nm/s corresponding to Fig. 6.12(b) were larger than those formed at $\dot{t}_{Ti}$=0.5 nm/s. Since the thickness and overall fraction of Ti deposited was the same at t=10 nm for both deposition rates, one tentative conclusion is that the fraction Ti transformed to TiO_x was increased at the lower deposition rate. Moreover, since the formation of TiO_x was, at least initially, an *in-situ* reaction with the limited O_2 in the chamber, the slow leakage of ambient O_2 into the deposition chamber over longer deposition times (lower deposition rates) facilitated a greater fraction of transformed TiO_x. The SAED patterns in Fig. 6.12 suggested that a greater proportion of deposited Ti at $\dot{t}_{Ti}$=0.1 nm/s formed anatase crystals whereas at $\dot{t}_{Ti}$=0.5 nm/s, there were primarily metallic Ti crystals that then later oxidised at the surface to form the core-shell nanoparticles. In other words, a Ti-ANC film at $\dot{t}_{Ti}$=0.5 nm/s contained a relatively high volume fraction of more polarisable Ti (core)-oxide

(shell) nanoparticles than a film at $\dot{t}_{Ti}$=0.1 nm/s that contained a relatively high fraction of oxide particles, for a nominally constant Ti fraction.

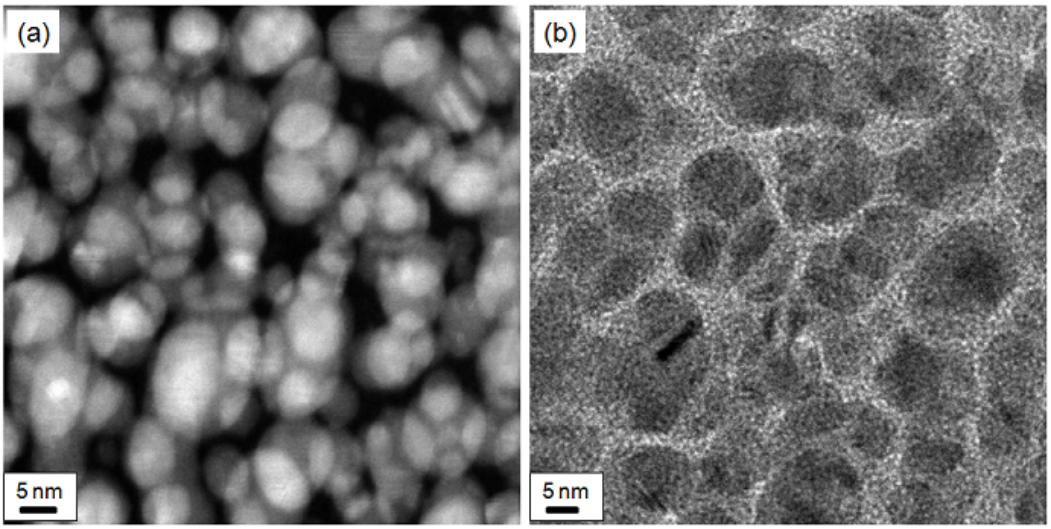


Figure 6.13: Plan-view (a) ADF-STEM image and (b) HRTEM image of a Ag-$Ti_{0.5}$-Ny_{10} ANC film.

Figures 6.13(a) and (b) show ADF-STEM and HRTEM plan-view images of a "three-phase" Ag-$Ti_{0.5}$-Ny_{10} ANC film respectively, with Ag nanoparticles or nano-islands "sitting" over one another, with the intervening layers of nylon-6 and the Ti-layer in the centre of the device, between the two Ag layers.

Figure 6.14(a) is a TEM image of a Ag-$Ti_{0.5}$-Ny_{10} ANC film and 6.14(b) is the corresponding SAED pattern. Figure 6.14(c) is a enhanced image of Fig. 6.14(b) and Fig. 6.14(d) is the magnified region from the highlighted square shown in Fig. 6.14(c). The measured *d*-spacings from the rings in the SAED pattern were: 0.24, 0.21, 0.15, and 0.12 nm corresponding to (111), (002), (022), and (113) lattice planes of Ag[170]. Any evidence of the presence of Ti or its oxide was not obvious from the unprocessed SAED pattern. Figure 6.14(d) shows two faint rings which are marked as "first" and "second" rings. The measured *d*-spacings from these rings were ~0.36 and ~0.17 nm respectively, which did not belong to Ag, but may offer a match with TiO_2-anatase (101)=0.351 nm, (105)=0.1699 nm, and (211)=0.1655, or Ti $(01\bar{1}2)$=0.1726 nm, suggesting the

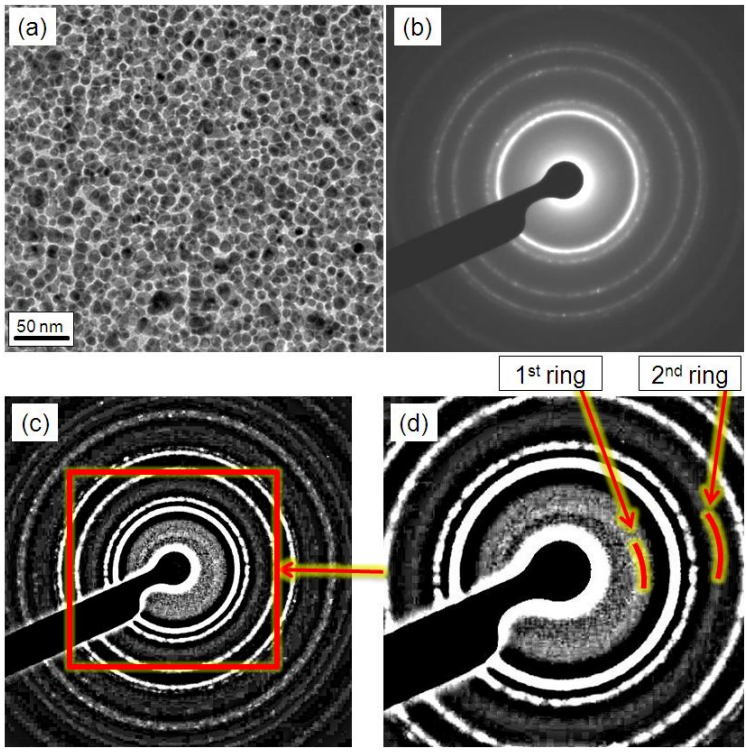


Figure 6.14: (a) TEM image of a Ag-$Ti_{0.5}$-Ny_{10} ANC film, (b) the corresponding SAED pattern, (c) enhanced image of (b), and (d) magnified region from the highlighted square shown in (c).

(somewhat discrete) presence of both metallic and oxidised Ti, along with the Ag nano-islands. Although d=0.17 nm was close to Ag_2O (220)=0.168 nm[171], the absence of a ring corresponding to Ag_2O (110)=0.337 nm[171] undermined the case for the presence of Ag_2O, and anatase-like TiO_x was considered more likely, especially in terms of the previous results for Ag-only and Ti-only containing films.

During the deposition of a metal on a polymer, the metal atoms that impinge onto a polymer surface can "dissolve" in the polymer leading to the embedding of metal particles inside the polymer. This "solubility" of metal atoms is promoted at temperatures above the polymer glass-transition temperature, where the polymer chains become mobile over a comparatively long-range[172,173]. The measured temperature of the glass substrate during metal deposition of ~40 ^{0}C was close to the glass transition temperature (T_g) of nylon-6 (reported in the

range 43-49 ^{0}C[140]), although metal embedding has also been observed at temperatures below the glass-transition temperature[174]. The constant temperature heat-treatment of the Ag-$Ti_{0.5}$-Ny_{10} ANC films to remove water-vapour effects was also at ~40 ^{0}C for 20 hours prior to dielectric measurement, and might have assisted in the embedding or mobility of metal atoms: predominantly the metallic Ag atoms/nano-clusters as a majority of the Ti clusters would be oxidised by this stage. Moreover, the initial deposited layer of nylon-6 onto which the Ag, Al or Ti is then deposited can never be atomically flat. Overall therefore the incoming Ag, Al and Ti atoms will form nano-islands and nanoparticles at varying "heights" or "thicknesses" across the cross-section of the nylon-6 film, and consistent with the TEM observations.

Based on these observations, a proposed cross-sectional schematic representation of the Ag-$Ti_{0.5}$-Ny_{10} ANC based capacitor is shown in the Fig. 6.15. The Ag, Ti (core)-oxide (shell), and Ti-oxide nanoclusters are embedded/formed at different thicknesses across the cross-section of the nylon-6 film.

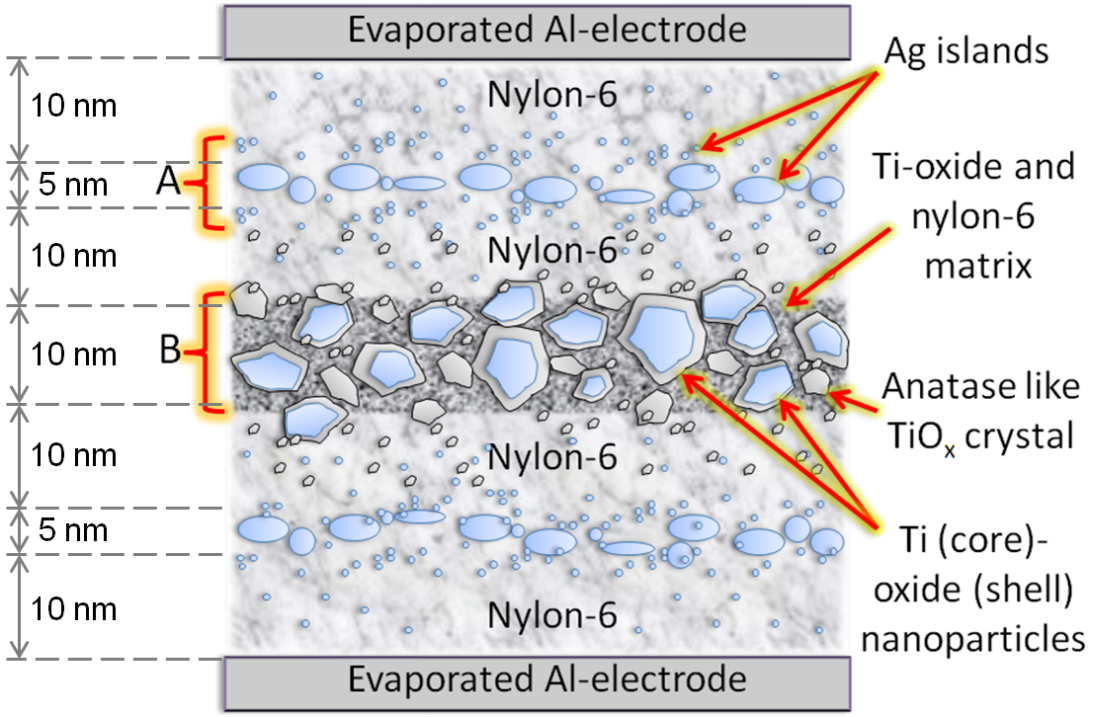


Figure 6.15: A cross-sectional schematic representation of a Ag-$Ti_{0.5}$-Ny_{10} ANC based capacitor showing the nominal thickness of each layer of the dielectric.

The majority of the Ag and Ti nano-clusters are within comparatively narrow layers, identified in Fig. 6.15 as A and B respectively. The Ti-layer (B) has Ti (core)-oxide (shell) nanoparticles dispersed in a matrix that is comprised of *both* Ti-oxide (anatase-like TiO_x and amorphous TiO_x) as the majority phase and nylon-6 as the minority phase. Thus any two neighbouring nanoparticles with metallic Ti cores are separated by a thin layer of dielectric, either nylon-6 or Ti-oxide, or both. Such an arrangement results in the formation of an "internal boundary layer capacitor" (IBLC)[175] as shown in Fig. 6.16. The two metallic Ti nano-cores act as the electrodes and the TiO_x shell layers between them (at the boundary) constitutes the dielectric of a nano-scale capacitor. IBLCs are qualitatively similar to the micro-/nano-capacitors that Ag particles form when separated by an intervening layer of dielectric, as described for Ag-ANCs in the previous chapter and in the section 2.3.2.

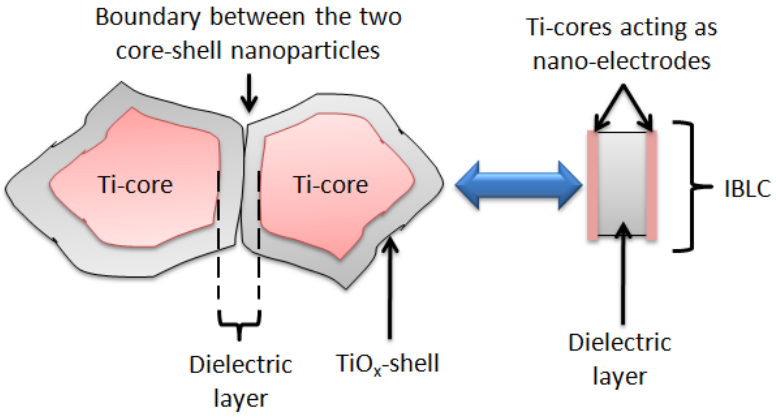


Figure 6.16: Schematic representation of two Ti (core)-oxide (shell) nanoparticles forming an "internal boundary layer capacitor" (IBLC).

Since the intervening layer of any dielectric between metallic electrodes is of the order of a few nanometers and a majority of the dielectric material in layer B is relatively high-k core-shell nanoparticles, an array of "nano-capacitors" or IBLCs that network randomly in series and parallel configurations is formed. This network, which is similar to a near-percolation network[35,36,49–56] of conducting particles in an insulating matrix and previously described for Ag in the previous

chapter, in combination with the relatively high polarisability of the core-shell particles, increases the effective k of the Ti-layer.

The Ag layer (A) forms Ag nano-islands that function as metallic nano-electrodes with the nylon-6 (k~4)[112] as the dielectric between them. The Ag-network is a similar arrangement to the network of conducting particles in near-percolating composites[35,36,49–56] but with a gradient of thicknesses of the intervening dielectric layer between the Ag-clusters across the cross-section of the film because the local volume fraction of Ag changes. The thickness of the dielectric (nylon-6) separating Ag-clusters in the nanocomposite is the lowest in the Ag-layer, and the dielectric thickness increases (as the volume fraction of Ag-clusters decreases) away from the Ag-layer. As seen in the previous chapter, the lack of either core-shell particles or a high-k oxide in the Ag-layer makes it less polarisable. Note that the nylon-6 layers sandwiching the Ag layer were reduced from 20 nm in Fig. 5.7(d) in the previous chapter to ~10 nm in Fig. 6.15 in this chapter. This leads to an increase in the effective volume fraction of Ag in this region, enhancing the nano-capacitor network effect.

As explained earlier, there will always be a small fraction of Ag based clusters outside the narrow Ag-layers and these tiny, *conducting* clusters extend the region in which the nano-capacitor effect operates. In the current case where the nylon-6 layers were only 10 nm thick, the nano-capacitor network might be extended from the Ag-layer (A) to the top Al-electrode, making all of the material between the Ag-layer and the Al-electrode a near-percolating nanocomposite. Similarly, a downward extension of the network by the tiny Ag-clusters makes the material between the Ag-layer (A) and Ti-layer (B) a near-percolating nanocomposite. Since the bottom half of the dielectric film is the mirror image of the top half, the nano-capacitor network is now extended *throughout the entire cross-section* of the film from the top Al-electrode to the bottom one.

Therefore a key distinction must be made at this point. While so far the ex-

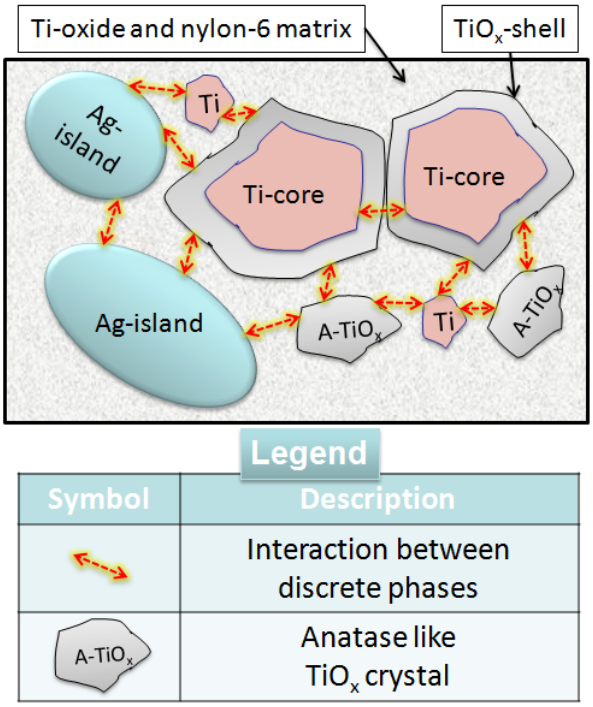


Figure 6.17: Schematic representation of the various types of nano-capacitor interactions between the discrete phases of an Ag-$Ti_{0.5}$-Ny_{10} ANC based dielectric.

planation of dielectric response of the capacitors has involved descriptions and measurements of an implicitly discrete layer of particles between nylon-6 layers (as seen in the previous chapter), here, given that the nylon-6 layers are now only 10 nm, and that the arrangement of metal-based islands is clearly not "planar" in a well-defined layer, the material between the Al-electrodes of the capacitor should now be considered a single effective medium consisting of an inter-connected nano-capacitor network. In this dielectric medium based on nylon-6, there are Ag nano-islands and Ti-based oxides, core-shell nanoparticles, and perhaps metallic Ti. These are close enough and sufficiently intermingled that as well as the "discrete" Ag nano-capacitor network and Ti-based core-shell nanoparticle contributions previously described, there are additional nano-capacitor interactions between all the discrete phases as shown in Fig. 6.17.

Thus, practically all of the material between the Al-electrodes might now make some contribution to the elevation of k over "pure" nylon-6 as a single, near-

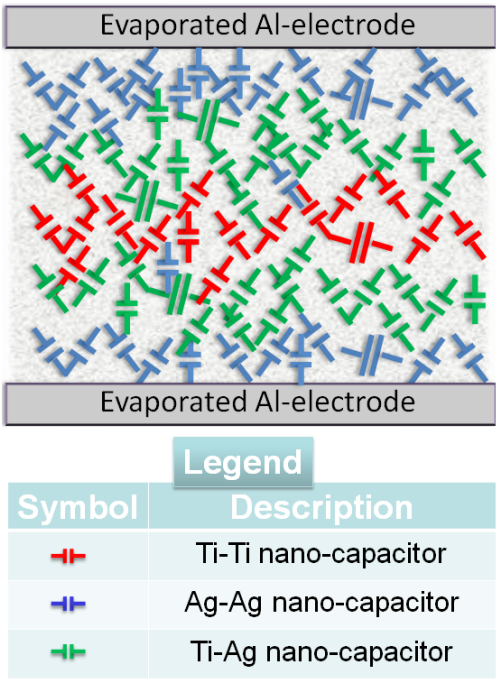


Figure 6.18: A cross-sectional schematic representation of a Ag-$Ti_{0.5}$-Ny_{10} ANC based capacitor showing a network of different types of nano-capacitors.

percolating nanocomposite. A cross-sectional schematic representation of an Ag-$Ti_{0.5}$-Ny_{10} ANC based capacitor with an interconnected network of different types of nano-capacitors is shown in Fig. 6.18, which allowed the dielectric response to reach as high as k~73. The loss increased in this composite dielectric medium because of the larger contribution of the more lossy conductor based nano-capacitor network, with $tan\ \delta$ rising from ~0.34 for Ti only ANCs to ~0.55 for Ti+Ag ANCs. If the structure shown in Fig. 6.19(a) is considered to be consisting of capacitors connected in series as shown in Fig. 6.19(d) due to considerably discrete alternating layers of nylon-6 and metal (Ag/Ti) [see Fig. 6.19(b)], then there would have been a significant reduction in the observed k and $tan\ \delta$ as the insulating nylon-6 layers would not allow the formation of a nano-capacitor network throughout the cross-section of the film. In the series connection of capacitors, the effective capacitance of the ANC would not exceed the capacitance of the nylon-6 layer, thereby limiting the overall enhancement in k. However, the formation of an inter-connected nano-capacitor network throughout the cross-section, as seen in

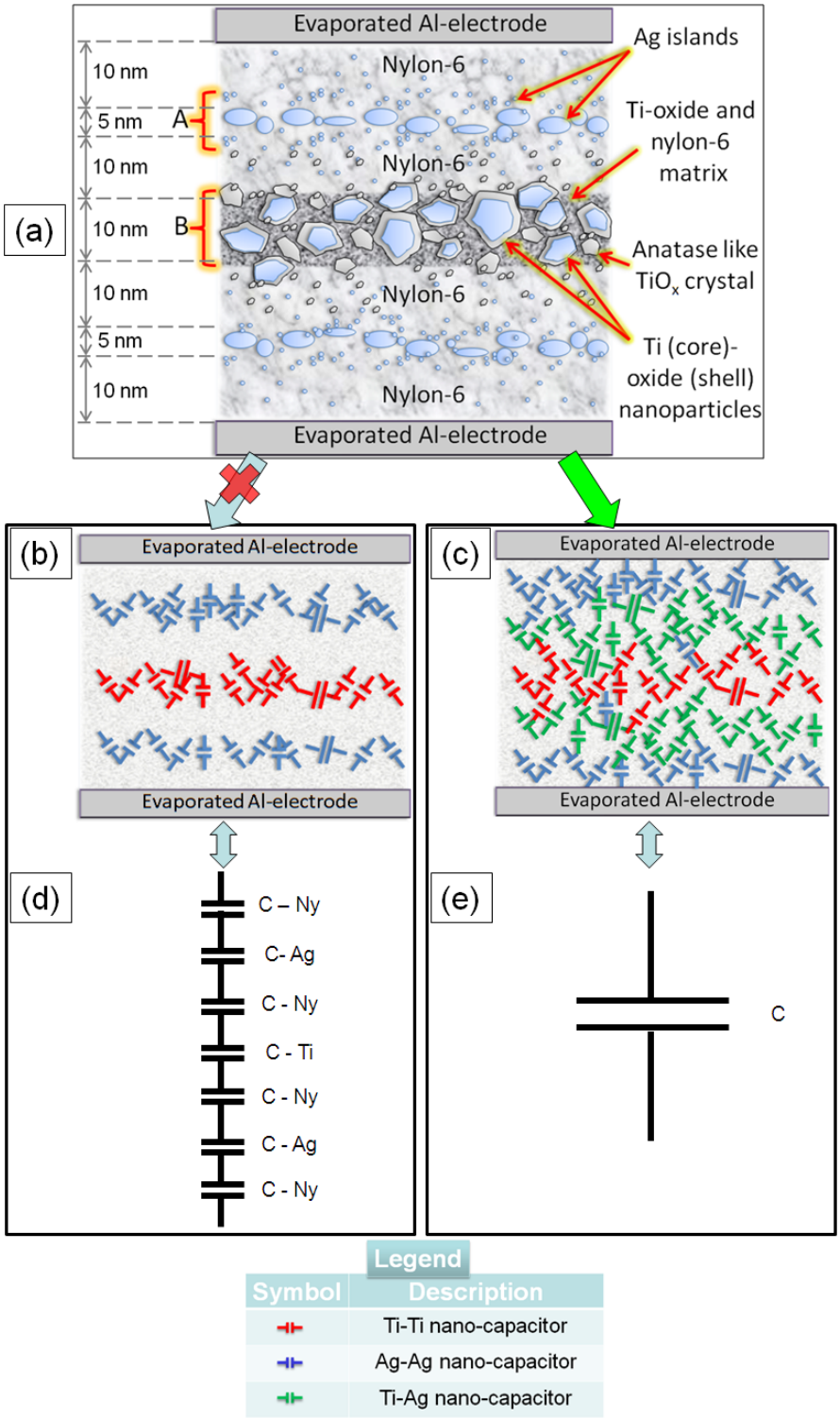


Figure 6.19: A cross-sectional schematic representation of a Ag-$Ti_{0.5}$-Ny_{10} ANC based capacitor showing a network of different types of nano-capacitors.

6.19(c), enables the treatment of the ANC as a single, nanocomposite structure that can be represented by a single capacitor [see Fig. 6.19(e)] with high k.

The k~17.5 of the Ag-Ti-ANCs at $\dot{t}_{Ti}$=0.1 nm/s was relatively low because, as previously described for Al, the Ti-layer had a greater proportion of anatase than relatively polarisable Ti (core)-oxide (shell) particles when compared with a Ti-layer at $\dot{t}_{Ti}$=0.5 nm/s.

6.3.2 Effect of the nylon-6 layer thickness

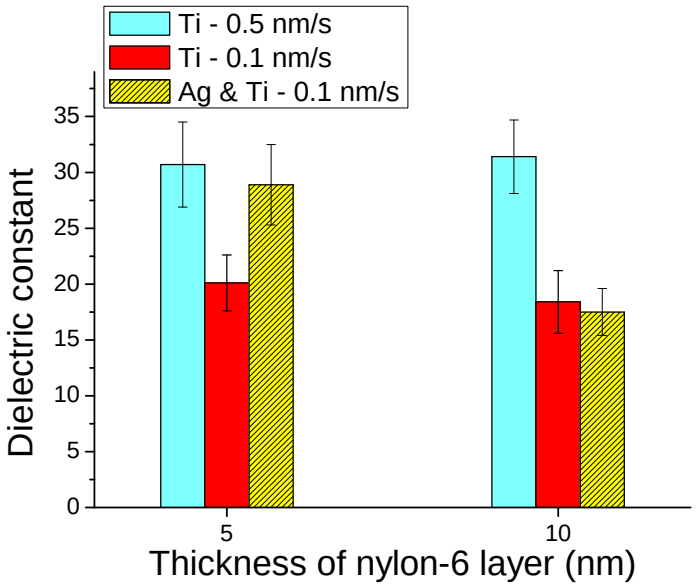


Figure 6.20: The variation of dielectric constant with thickness t of the deposited nylon-6 layer in Ti-ANC and Ag-Ti-ANC based capacitors at 1 kHz and 40 ^{0}C. The thickesses of the deposited Ti and Ag layers in all ANCs are 10 and 5 nm respectively.

Figures 6.20 and 6.21 show the variation of dielectric constant and capacitance per unit volume with thickness t of the deposited nylon-6 layer in Ti-ANC and Ag-Ti-ANC based capacitors at 1 kHz and 40 ^{0}C respectively. The thickesses of the deposited Ti and Ag layers in all ANCs were 10 and 5 nm respectively.

In Fig. 6.20, k for Ti-ANCs with t_{Ny}=5 and 10 nm was almost the same at k~31 for $\dot{t}_{Ti}$=0.5 nm/s. There was a similar weak effect on nylon-6 layer thickness for Ti-ANCs with $\dot{t}_{Ti}$=0.1 nm/s. However, k~29 of Ag-Ti-ANC at t=5 nm of nylon-6

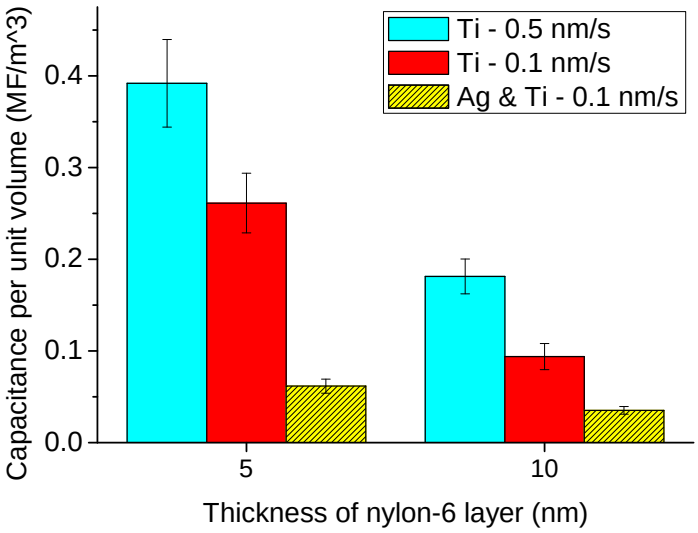


Figure 6.21: The variation of capacitance per unit volume with thickness t of the deposited nylon-6 layer in Ti-ANC and Ag-Ti-ANC based capacitors at 1 kHz and 40 ^{0}C. The thickesses of the deposited Ti and Ag layers in all ANCs are 10 and 5 nm respectively.

was significantly greater than k~17.5 for Ag-Ti-ANCs at t=10 nm, because local volume fraction of Ag at t_{Ny}=5 nm was higher than at t_{Ny}=10 nm.

These results further support the proposed explanation for the enhanced k that is due to the formation of a single, near-percolating nanocomposite, described in section 6.3.1. Figure 6.22 is a schematic representation of the cross-sections of ANC films showing the relative positions of the region, R, in which the near-percolation effect operates at various thicknesses of the nylon-6 layer. The nominal thickness of the deposited Ag in all ANCs is 5 nm.

At t_{Ny}=20 nm in Fig. 6.22(a), R is relatively far from the Al-electrode and the v_f of Ag in the 20 nm thick nylon-6 layer might be so small (or nil) so that it may be considered as a discrete, insulating layer, thereby limiting the overall enhancement in k, as seen in the previous chapter. When t_{Ny} is reduced to 10 nm or 5 nm, the region R becomes sufficiently close to the Al-electrode to form a near-percolating network, as seen in Fig. 6.22(b) or (c). At these thicknesses, the nylon-6 layer ceases to be a discrete, insulating layer that separates the Al-

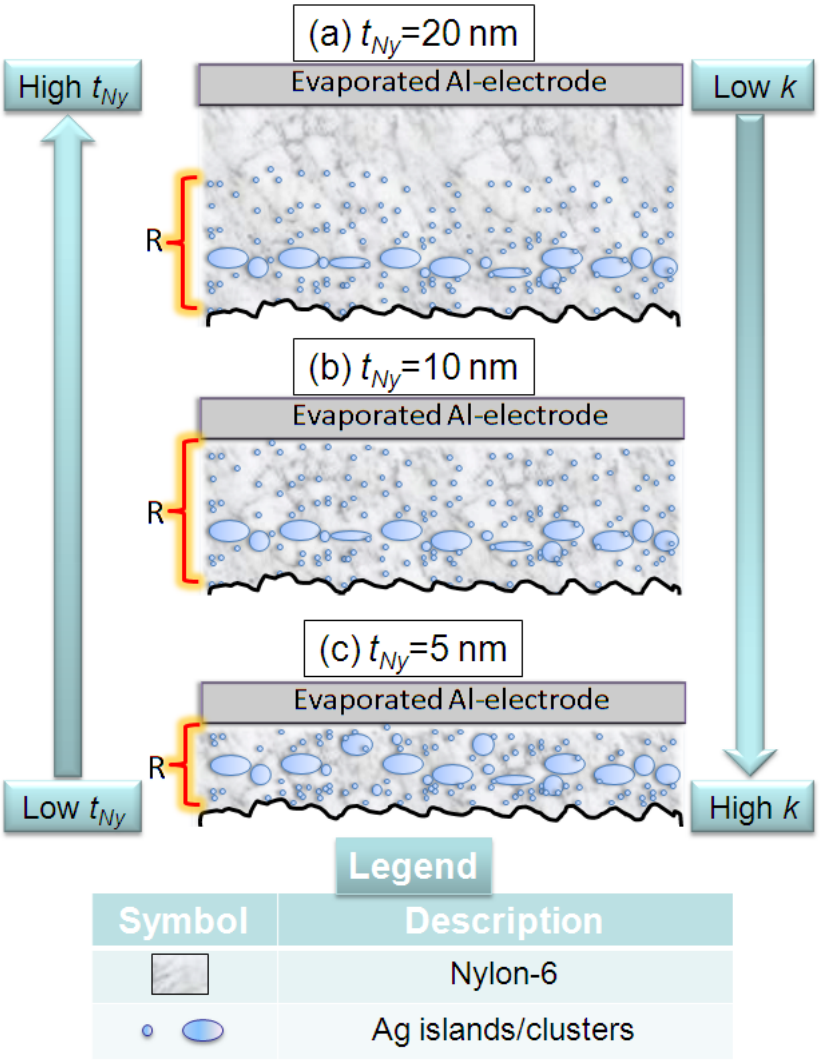


Figure 6.22: A schematic representation of the cross-sections of ANC films showing the relative positions of the region, R, in which the near-percolation effect operates at various thicknesses of the nylon-6 layer. (a) t_{Ny}=20 nm, (b) t_{Ny}=10 nm, and (c) t_{Ny}=5 nm. The thickness of the deposited Ag in all ANCs is 5 nm.

electrode from the rest of the ANC film. Therefore, the thickness of the nylon-6 layer and the percolative nature of the nanocomposite film are in an inverse relationship. It is important to note that the thickness of the nylon-6 layer should not be reduced to such an extent that the dielectric starts percolating, in which case the dielectric loss will be relatively and eventually unacceptably high. Based on the nature of the application, the nylon-6 layer thickness may be carefully controlled to obtain a dielectric with an optimised trade-off between dielectric constant and dielectric loss.

Although Fig. 6.20 suggested that the effect of Ag might be useful for increasing dielectric constant, especially at a nylon-6 thickness of 5 nm, it should be recalled that the Ag-containing capacitor variants involved more nominally discrete layers, including additional layers of nylon-6 (compare Figs. 6.1 and 6.2). To normalise the resulting change in thickness of the device when Ag is deposited as well as Ti, Fig. 6.21 shows a plot of the capacitance per unit volume of dielectric material. The Ag-Ti-ANCs had lower energy densities when compared with Ti-ANCs due to the relatively high t of the many-layered Ag-Ti-ANCs. Nevertheless, an energy density of ~0.4 MFm^{-3} of $Ti_{0.5}$-Ny_5 ANCs was at least 4 times higher than those reported for various metal-insulator-metal (MIM) capacitors fabricated via complex, multiple processes involving etching, photolithography and nanoporous templates[176–181].

6.4 Conclusions

An alternate deposition technique was used to fabricate Ti or Ti+Ag and nylon-6 based high-k capacitors. Studies involving STEM, in-depth analysis of SAED patterns and FFTs from HRTEM images showed that the deposited Ti oxidised partially on the surface to form Ti (core)-oxide (shell) nanoparticles and in some cases, oxidised completely to form anatase nanoparticles. The occurrence of

metallic Ti particles well-encapsulated in nylon-6 was comparatively rare. The Ti-oxide shell showed both amorphous and semi-crystalline regions, and was studded with defective regions. The high k of Ti-ANCs arose due to the combined contribution of the enhanced polarisability of core-shell and anatase nanoparticles. If a low Ti deposition rate was used, a relatively high volume fraction of anatase particles were formed in lower k-ANCs, suggesting that the enhancement in k was predominantly due to core-shell nanoparticles.

Incorporating Ag nanoparticles and reducing the nylon-6 thickness to 10 nm resulted in a dielectric medium of inter-mingled Ag and Ti-based oxides and core-shell nanoparticles throughout the nylon-6 matrix. This k~73 was due to the combined effects of the polarisable Ti-based core-shell nanoparticles and a nano-capacitor network based on not only Ag nano-islands, but interactions between all the discrete phases that created an inter-connected nano-capacitor network. A decrease in the thickness of the nylon-6 layers from 10 to 5 nm in Ti-ANCs had little effect on k, but increased k of Ag-Ti-ANCs significantly due to an increase in the effective volume fraction of Ag in the 5 nm thick nylon-6 layer, enhancing the nano-capacitor network effect, but also increasing dielectric loss. In effect, the volume fraction that controls the dielectric properties could be engineered in the ANCs simply by varying the thickness of the insulating nylon-6 layer.

The Ti-based ANCs showed higher dielectric constants than their Al-based equivalents because the anatase-like oxide in Ti-based ANCs was inherently more polarisable. However, like Al-ANCs, the strongest elevation in k occurred only when core (metal)-shell (oxide) particles were present, and if entirely or largely oxide particles dominated the nanostructure, dielectric response reduced. Together with the earlier work on Al, this chapter has produced strong evidence to support the critical role of interfacial polarisation effects in super-k behaviour in dielectrics containing core-shell particles.

Chapter 7

Conclusions and Future Work

7.1 Conclusions

This thesis has concerned the investigation of the dielectric properties of polymer-nanocomposite (PNC) based capacitors fabricated by vacuum based co-deposition and alternate deposition techniques. A range of PNCs containing reactive metals (Al and Ti) and a noble metal (Ag) in a matrix of nylon-6 were processed and their dielectric response was related to the micro/nano-structures which were studied using advanced microscopy techniques.

Al-PNCs processed via the co-deposition technique had a comparatively low $k<9$ because of complete oxidation of Al into Al-oxide at relatively low deposition rates $<<$ 0.1 nm/s. However, the PNCs absorbed water vapour in varying amounts that had a profound effect on dielectric response. Therefore, a constant temperature heat-treatment was developed and this method was then applied to all PNC studies. The dielectric constant of the Al-based PNCs after heat-treatment agreed broadly with popular analytical expressions from the literature built on various mixing assumptions.

An alternate deposition variant was developed that operated at metal deposition rates that were in the range of 0.1 to 0.5 nm/s, compared with nylon-6 rates of

0.1 nm/s. The higher deposition rates resulted in PNCs consisting of metal based clusters embedded in a nylon-6 matrix. At a deposited metal layer thickness of 5 nm, Ag, being a noble metal, formed a nano-capacitor network and enhanced interfacial polarisation leading to an increase to k~10. However, the 20 nm thick nylon-6 layers that sandwiched the Ag-layer limited the overall enhancement in dielectric response.

At a deposition rate of $\dot{t}_{Al}$=0.1 nm/s and deposited layer thickness of t=2 nm, Al formed Al-oxide with k~4.5. Al (core)-oxide (shell) particles formed at $t \geq 5$ nm and k~19. TEM studies revealed a highly defective, strained and non-stoichiometric oxide-shell around the Al-core that enhanced interfacial polarisation.

Using a similar approach of alternate deposition, PNCs consisting of Ti and nylon-6 were produced. At a Ti thickness of 10 nm deposited at 0.5 nm/s, Ti (core)-oxide (shell) nanoparticles and Ti-oxide nanoparticles were formed, and k~38. The formation of a defective, non-stoichiometric and (presumably) semi-conducting Ti-oxide shell around the metallic nano-cores of Ti again lead to enhanced interfacial polarisation. A lower Ti deposition rate of 0.1 nm/s produced a relatively large volume fraction of Ti-oxide (anatase) phase, which were less polarisable than the core-shell particles, resulting in a relatively low k~18.5 at a Ti deposited thickness of 10 nm.

Finally, the nano-capacitor network effect based on conducting Ag nano-islands and the enhanced polarisability of a core-shell particle containing layer in nylon-6 were combined. Incorporating Ag nanoparticles and reducing the nylon-6 thickness to 10 nm resulted in a dielectric medium of inter-mingled Ag and Ti-based oxides and core-shell nanoparticles throughout the nylon-6 matrix. This k~73 was due to the combined effects of the polarisable Ti-based core-shell nanoparticles and a nano-capacitor network based on not only Ag nano-islands, but interactions between all the discrete phases that created an inter-connected nano-capacitor network. A decrease in the thickness of the nylon-6 layer from 10 nm to 5 nm in

such Ag-Ti-ANCs increased k from ~17.5 to ~29 due to an overall increase in the volume fraction of Ag in the 5 nm nylon-6 layer.

Figure 7.1 shows a summary plot comparing the dielectric constants of ANCs with various filler metals at 1 kHz and 40 ^{0}C. The deposition rate $\dot{t}$ and thickness t of Ag in the Ag-Ti-ANC were 0.1 nm/s and 5 nm respectively. The $\dot{t}$ and t of Al, Ag, and Ti in all other cases were 0.5 nm/s and 10 nm respectively.

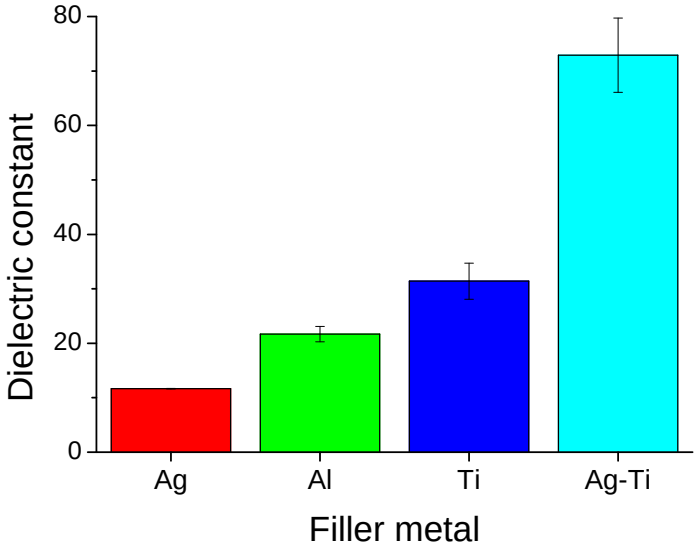


Figure 7.1: A column graph comparing the dielectric constants of ANCs with various filler metals at 1 kHz and 40 ^{0}C. The deposition rate $\dot{t}$ and thickness t of Ag in the Ag-Ti-ANC were 0.1 nm/s and 5 nm respectively. The $\dot{t}$ and t of Al, Ag, and Ti in all other cases were 0.5 nm/s and 10 nm respectively.

HRTEM in combination with low-angle and high-angle DF-STEM was used extensively to study the evolution and structure of metal-based islands in nylon-6 matrix. A technique involving the ablation of nylon-6 under the electron beam was developed to characterise nanoparticles in their pristine form, which enabled the study of the oxide-shell, independent of the nylon-6 matrix, on a nano-scale. The use of various TEM techniques and XPS helped to understand the micro-/nano-structure of the PNCs and relate them to the observed dielectric response, which lead to the conceptualisation of different nano-arrangements of the metal-based islands in the nylon-6 matrix.

This thesis has successfully demonstrated that alternate deposition can be used to fabricate high-k PNCs containing a range of filler metals. Alternate deposition is a simple technique that, after careful optimisation and development, offers sufficient control over polymer and metallic layer thicknesses at the nano-scale. The relative thicknesses and the deposition rates of the various layers have been shown to play a key role in dictating the chemistry and micro-/nano-structure of the resulting composite, multi-layer film. The alternate deposition technique reduced the complexities involved in trying to control relative deposition rates and effective volume fraction of minority phases in the PNCs.

7.2 Future Work

This section recommends possible directions for future work in the area of polymer based composites for dielectric and capacitor applications.

- The current work did not explore frequency effects on dielectric response, and this could be pursued in subsequent studies, together with the effect of temperature - both of which are important practical considerations of power conditioning capacitors in practice. The use of lower intrinsic loss polymers should also be considered since in some configurations, dielectric loss in the PNCs became unusually high. Finally, experiments might be contrived to try to control and measure the proportion of core-shell particles versus largely oxide or metallic particles. Although core-shell particles could be manufactured outside the polymer matrix with increased control, achieving such fine-scale dispersion as the current work will likely be difficult, but greater understanding of the benefits and disadvantages of *in-situ* and extrinsic core-shell particles in PNCs might be developed.

- Deposition of the reactive metals in a controlled O_2 partial pressure might be explored in order to gain control over the extent of core-shell particles

formation, and might help to engineer the thickness and chemistry of the oxide.

- Measuring the dielectric breakdown voltage of the PNCs is important to quantify energy density and to make sure that the enhancement in the dielectric properties has not had a negative effect on the breakdown voltage.
- Increasing the number of alternating layers in the PNCs to make thick dielectric films, and scaling up of the alternate deposition technique from a lab-scale evaporator to a roll-to-roll coater[113–119].

References

[1] M. Howse, "All-electric aircraft," *Power Engineer*, vol. 17, no. 4, p. 35, 2003.

[2] Federal Aviation Administration, U.S.A., *Hydraulic and Pneumatic Power Systems*. Aviation Maintenance Technician Handbook - Airframe: Chapter 12.

[3] J. A. Weimer, "The role of electric machines and drives in the more electric aircraft," in *IEEE IEMDC'03: IEEE International Electric Machines and Drives Conference, Vols 1-3*, p. 11, 2003. IEEE International Electronic Machines and Drives Conference, Madison, WI, 01-04 June, 2003.

[4] L. Faleiro, "Beyond the more electric aircraft," *Aerospace America*, vol. 43, no. 9, p. 35, 2005.

[5] Webpage, "http://www.epcos.com."

[6] J. A. Rosero, J. A. Ortega, E. Aldabas, and L. Romeral, "Moving towards a more electric aircraft," *IEEE Aerospace and Electronic Systems Magazine*, vol. 22, no. 3, p. 3, 2007.

[7] J. S. Cloyd, "Status of the United States air force's more electric aircraft initiative," *IEEE Aerospace and Electronic Systems Magazine*, vol. 13, no. 4, p. 17, 1998.

[8] Webpage, "http://www.rubycon.com."

[9] H. Tang, Y. Lin, C. Andrews, and H. A. Sodano, "Nanocomposites with increased energy density through high aspect ratio PZT nanowires," *Nanotechnology*, vol. 22, no. 1, p. 015702, 2011.

[10] R. Waser, ed., *Nanoelectronics and Information Technology*. Wiley, 3 ed., 2012. Figure 2.2 is reprinted from *Nanoelectronics and Information Technology*, R. Waser (ed.), 3rd edition, Copyright (2012), with permission from John Wiley and Sons.

[11] B. Brown, D. Hess, V. Desai, and M. J. Deen, "Dielectric science and technology," *The Electrochemical Society - Interface*, p. 28, 2006.

[12] N. Wang, F. C. Lu, and H. M. Li, "Analytical processing of on-line monitored dissipation factor based on morphological filter," *IEEE Transactions on Dielectrics and Electrical Insulation*, vol. 11, no. 5, SI, p. 840, 2004.

[13] T.-C. Mo, H.-W. Wang, S.-Y. Chen, and Y.-C. Yeh, "Synthesis and dielectric properties of polyaniline/titanium dioxide nanocomposites," *Ceramics International*, vol. 34, no. 7, p. 1767, 2008.

[14] S. Fujisaki, H. Ishiwara, and Y. Fujisaki, "Low-voltage operation of ferroelectric poly(vinylidene fluoride-trifluoroethylene) copolymer capacitors and metal-ferroelectric-insulator-semiconductor diodes," *Applied Physics Letters*, vol. 90, no. 16, 2007.

[15] Y. Zhou, H. Wang, F. Xiang, H. Zhang, K. Yu, and L. Chen, "A poly(vinylidene fluoride) composite with added self-passivated microaluminum and nanoaluminum particles for enhanced thermal conductivity," *Applied Physics Letters*, vol. 98, no. 18, 2011.

[16] J. W. Xu and C. P. Wong, "Effect of the polymer matrices on the dielectric behavior of a percolative high-k polymer composite for embedded capacitor applications," *Journal of Electronic Materials*, vol. 35, no. 5, p. 1087, 2006.

[17] P. Barber, S. Balasubramanian, Y. Anguchamy, S. Gong, A. Wibowo, H. Gao, H. Ploehn, and H. Loye, "Polymer Composite and Nanocompos-

ite Dielectric Materials for Pulse Power Energy Storage," *Materials*, vol. 2, p. 1697, 2009.

[18] D. L. Ma, T. A. Hugener, R. W. Siegel, A. Christerson, E. Martensson, C. Onneby, and L. S. Schadler, "Influence of nanoparticle surface modification on the electrical behaviour of polyethylene nanocomposites," *Nanotechnology*, vol. 16, no. 6, p. 724, 2005.

[19] Y. Y. Sun, Z. Q. Zhang, and C. P. Wong, "Influence of interphase and moisture on the dielectric spectroscopy of epoxy/silica composites," *Polymer*, vol. 46, no. 7, p. 2297, 2005.

[20] J. W. Xu, K. S. Moon, C. Tison, and C. P. Wong, "A novel aluminum-filled composite dielectric for embedded passive applications," *IEEE Transactions on Advanced Packaging*, vol. 29, no. 2, p. 295, 2006.

[21] J. Lu and C. P. Wong, "Polymer nanocomposites with high dielectric strength and high frequency performance for emdedded passive applications," in *2008 IEEE Conference on Polymers and Adhesives in Microelectronics and Photonics and 2008 IEEE Interdisciplinary Conference on Portable Information Devices*, p. 171, 2008. IEEE Conference on Polymers and Adhesives in Microelectronics and Photonics/IEEE Interdisciplinary Conference on Portable Information Devices, Garmisch Partenkirchen, Germany, 17-20 August, 2008.

[22] J. Xu and C. P. Wong, "Characterization and properties of an organic-inorganic dielectric nanocomposite for embedded decoupling capacitor applications," *Composites Part A-Applied Science and Manufacturing*, vol. 38, no. 1, p. 13, 2007.

[23] T. J. Lewis, "Interfaces are the dominant feature of dielectrics at the nano-

metric level," *IEEE Transactions on Dielectrics and Electrical Insulation*, vol. 11, no. 5, SI, p. 739, 2004.

[24] G. C. Montanari, D. Fabiani, and F. Palmieri, "Modification of electrical properties and performance of EVA and PP insulation through nanostructure by organophilic silicates," *IEEE Transactions on Dielectrics and Electrical Insulation*, vol. 11, no. 5, SI, p. 754, 2004.

[25] J. Li, J. Claude, L. E. Norena-Franco, S. Il Seok, and Q. Wang, "Electrical energy storage in ferroelectric polymer nanocomposites containing surface-functionalized BaTiO(3) nanoparticles," *Chemistry of Materials*, vol. 20, no. 20, p. 6304, 2008.

[26] M. K. Kilaru, J. Heikenfeld, G. Lin, and J. E. Mark, "Strong charge trapping and bistable electrowetting on nanocomposite fluoropolymer : BaTiO3 dielectrics," *Applied Physics Letters*, vol. 90, no. 21, 2007.

[27] Y. G. Wu, X. H. Zhao, F. Li, and Z. G. Fan, "Evaluation of mixing rules for dielectric constants of composite dielectrics by MC-FEM calculation on 3D cubic lattice," *Journal of Electroceramics*, vol. 11, no. 3, p. 227, 2003.

[28] C. Brosseau, "Modelling and simulation of dielectric heterostructures: a physical survey from an historical perspective," *Journal of Physics D-Applied Physics*, vol. 39, no. 7, p. 1277, 2006. Conference on Modelling Simulation and Design of Dielectrics, Homerton Coll, Cambridge, ENGLAND, APR, 2005.

[29] V. Myroshnychenko and C. Brosseau, "Finite-element modeling method for the prediction of the complex effective permittivity of two-phase random statistically isotropic heterostructures," *Journal of Applied Physics*, vol. 97, no. 4, p. 044101, 2005.

[30] Y. Rao, J. M. Qu, T. Marinis, and C. P. Wong, "A precise numerical prediction of effective dielectric constant for polymer-ceramic composite based on effective-medium theory," *IEEE Transactions on Components and Packaging Technologies*, vol. 23, no. 4, p. 680, 2000.

[31] K.-L. Ying and T.-E. Hsieh, "Sintering behaviors and dielectric properties of nanocrystalline barium titanate," *Materials Science and Engineering B-Solid State Materials for Advanced Technology*, vol. 138, no. 3, p. 241, 2007.

[32] D. H. Yoon, J. P. Zhang, and B. I. Lee, "Dielectric constant and mixing model of BaTiO3 composite thick films," *Materials Research Bulletin*, vol. 38, no. 5, p. 765, 2003.

[33] T. Yamada, T. Ueda, and T. Kitayama, "Piezoelectricity of a high-content lead zirconate titanate polymer composite," *Journal of Applied Physics*, vol. 53, no. 6, p. 4328, 1982.

[34] D. Stauffe and A. Aharony, *Introduction to percolation theory*. Taylor and Francis, 1994.

[35] C. Pecharroman and J. S. Moya, "Experimental evidence of a giant capacitance in insulator-conductor composites at the percolation threshold," *Advanced Materials*, vol. 12, no. 4, p. 294, 2000.

[36] X. Huang, P. Jiang, and L. Xie, "Ferroelectric polymer/silver nanocomposites with high dielectric constant and high thermal conductivity," *Applied Physics Letters*, vol. 95, no. 24, p. 242901, 2009. Figure 2.6 is reprinted from *Applied Physics Letters*, 95, Huang *et al.*, "Ferroelectric polymer/silver nanocomposites with high dielectric constant and high thermal conductivity", 242901, Copyright (2009), with permission from AIP Publishing LLC.

[37] Y. Rao and C. P. Wong, "Material characterization of a high-dielectric-

constant polymer-ceramic composite for embedded capacitor for RF applications," *Journal of Applied Polymer Science*, vol. 92, no. 4, p. 2228, 2004.

[38] S. Ogitani, S. A. Bidstrup-Allen, and P. A. Kohl, "Factors influencing the permittivity of polymer/ceramic composites for embedded capacitors," *IEEE Transactions on Advanced Packaging*, vol. 23, no. 2, p. 313, 2000.

[39] S. D. Cho and K. W. Paik, "Relationships between suspension formulations and the properties of BaTiO3/epoxy composite films for integral capacitors," in *51st Electronic Components & Technology Conference*, Electronic Components and Technology Conference, p. 1418, 2001. 51st Electronic Components and Technology Conference (ECTC), Orlando, FL, 29 May-01 June, 2001.

[40] A. J. Bell, "Grain size effects on barium titanate-revisted," in *9th IEEE Int. Symp. Appl. Ferroelectrics*, p. 14, 1994.

[41] G. R. D. Hennings, "Temperature stable dielectrics based on chemically inhomogeneous barium titanate," *Journal of American Ceramic Society*, vol. 67, no. 4, p. 249, 1984.

[42] S. L. Swartz, "Topics in electronic ceramics," *IEEE Transactions on Electrical Insulation*, vol. 25, no. 5, p. 935, 1990.

[43] W. R. Buessem, L. E. Cross, and A. K. Goswami, "Effect of 2-dimensional pressure on the permittivity of fine-grained and coarse-grained barium-titanate," *Journal of the American Ceramic Society*, vol. 75, no. 11, p. 2926, 1992.

[44] Y. Rao, C. P. Wong, J. M. Qu, and T. Marinis, "Effective dielectric constant prediction of polymer-ceramic composite based on self-consistent theory," in *50th Electronic Components & Technology Conference - 2000 Proceedings*,

Electronic Components and Technology Conference, p. 615, 2000. 50th Electronic Components & Technology Conference (ECTC 01), Las Vegas, NV, 21-24 May, 2000.

[45] P. Thomas, S. Satapathy, K. Dwarakanath, and K. B. R. Varma, "Dielectric properties of poly(vinylidene fluoride)/CaCu(3)Ti(4)O(12) nanocrystal composite thick films," *Express Polymer Letters*, vol. 4, no. 10, p. 632, 2010.

[46] K. W. Paik, S. D. Cho, J. G. Hyun, S. Lee, H. Kim, and J. Kim, "Epoxy/BaTiO(3) (SrTiO(3)) composite films for high dielectric constant and low tolerance embedded capacitors fabrication in organic substrates," in *2005 10th International Symposium on Advanced Packaging Materials: Processes, Properties and Interfaces*, p. 227, 2005. 10th International Symposium on Advanced Packaging Materials, Irvine, CA, 16-18 March, 2005.

[47] S. George, P. S. Anjana, M. T. Sebastian, J. Krupka, S. Uma, and J. Philip, "Dielectric, mechanical, and thermal properties of low-permittivity polymer-ceramic composites for microelectronic applications," *International Journal of Applied Ceramic Technology*, vol. 7, no. 4, p. 461, 2010.

[48] J. Li, S. I. Seok, B. Chu, F. Dogan, Q. Zhang, and Q. Wang, "Nanocomposites of ferroelectric polymers with TiO(2) nanoparticles exhibiting significantly enhanced electrical energy density," *Advanced Materials*, vol. 21, no. 2, p. 217, 2009.

[49] F. He, S. Lau, H. L. Chan, and J. Fan, "High dielectric permittivity and low percolation threshold in nanocomposites based on poly(vinylidene fluoride) and exfoliated graphite nanoplates," *Advanced Materials*, vol. 21, no. 6, p. 710, 2009. Figures 2.8 and 2.9 are reprinted from *Advanced Materials*, 21, He *et al.*, "High Dielectric Permittivity and Low Percolation Thresh-

old in Nanocomposites Based on Poly(vinylidene fluoride) and Exfoliated Graphite Nanoplates", 710, Copyright (2008), with permission from John Wiley and Sons.

[50] Z. M. Dang, Y. H. Lin, and C. W. Nan, "Novel ferroelectric polymer composites with high dielectric constants," *Advanced Materials*, vol. 15, no. 19, p. 1625, 2003.

[51] C. Huang, Q. M. Zhang, and J. Su, "High-dielectric-constant all-polymer percolative composites," *Applied Physics Letters*, vol. 82, no. 20, pp. 3502–3504, 2003.

[52] Y. Song, T. W. Noh, S. Lee, and J. R. Gaines, "Experimental study of the three-dimensional ac conductivity and dielectric constant of a conductor-insulator composite near the percolation threshold," *Physical Review B*, vol. 33, no. 2, p. 904, 1986.

[53] D. T. D.M. Grannan, J.C. Garland, "Critical behaviour of the dielectric constant of a random composite near the percolation threshold," *Physical Review Letters*, vol. 46, no. 5, p. 375, 1981.

[54] J. X. Lu, K. S. Moon, J. W. Xu, and C. P. Wong, "Synthesis and dielectric properties of novel high-K polymer composites containing in-situ formed silver nanoparticles for embedded capacitor applications," *Journal of Materials Chemistry*, vol. 16, no. 16, p. 1543, 2006.

[55] Y. Shen, Y. Lin, M. Li, and C.-W. Nan, "High dielectric performance of polymer composite films induced by a percolating interparticle barrier layer," *Advanced Materials*, vol. 19, no. 10, p. 1418, 2007.

[56] X. Zhao, A. A. Koos, B. T. T. Chu, C. Johnston, N. Grobert, and P. S. Grant, "Spray deposited fluoropolymer/multi-walled carbon nanotube com-

posite films with high dielectric permittivity at low percolation threshold," *Carbon*, vol. 47, no. 3, p. 561, 2009. Figures 2.10 and 2.16 are reprinted from *Carbon*, Volume 47, Issue 3, Zhao *et. al.*,"Spray deposited fluoropolymer/multi-walled carbon nanotube composite films with high dielectric permittivity at low percolation threshold", 561, Copyright (2009), with permission from Elsevier.

[57] T. Wei, C. Q. Jin, W. Zhong, and J. M. Liu, "High permittivity polymer embedded with Co/ZnO core/shell nanoparticles modified by organophosphorus acid," *Applied Physics Letters*, vol. 91, no. 22, p. 222907, 2007.

[58] J. W. Xu and C. P. Wong, "Low-loss percolative dielectric composite," *Applied Physics Letters*, vol. 87, no. 8, p. 082907, 2005. Figure 2.11 is reprinted from *Applied Physics Letters*, 87, Xu *et al.*, "Low-loss percolative dielectric composite", 082907, Copyright (2005), with permission from AIP Publishing LLC.

[59] J. W. Xu and C. P. Wong, "Development of a novel aluminum-filled composite for embedded passive applications," in *53rd Electronic Components & Technology Conference, 2003 Proceedings*, p. 173, 2003. 53rd Electronic Components and Technology Conference, New Orleans, LA, 27-30 May, 2003.

[60] X. Huang, P. Jiang, C. Kim, Q. Ke, and G. Wang, "Preparation, microstructure and properties of polyethylene aluminum nanocomposite dielectrics," *Composites Science and Technology*, vol. 68, no. 9, p. 2134, 2008.

[61] P. R. Emtage and W. Tantraporn, "Schottky emission through thin insulating films," *Physical Review Letters*, vol. 8, no. 7, p. 267, 1962.

[62] T. E. Hartman and J. S. Chivian, "Electron tunneling through thin alu-

minum oxide films," *Physical Review A-General Physics*, vol. 134, no. 4A, p. 1094, 1964.

[63] C. D. Bond, C. S. Guenzer, and C. A. Carosella, "Intermodulation generation by electron-tunneling through aluminum-oxide films," *Proceedings of the IEEE*, vol. 67, no. 12, p. 1643, 1979.

[64] G. G. Paulus, F. Zacher, H. Walther, A. Lohr, W. Becker, and M. Kleber, "Above-threshold ionization by an elliptically polarized field: quantum tunneling interferences and classical dodging," *Physical Review Letters*, vol. 80, p. 484, 1998.

[65] J. Ruseckas, "Possibility of tunneling time determination," *Physical Review A*, vol. 63, p. 052107, 2001.

[66] M. Uiberacker, T. Uphues, M. Schultze, A. J. Verhoef, V. Yakovlev, M. F. Kling, J. Rauschenberger, N. M. Kabachnik, H. Schroeder, M. Lezius, K. L. Kompa, H. G. Muller, M. J. J. Vrakking, S. Hendel, U. Kleineberg, U. Heinzmann, M. Drescher, and F. Krausz, "Attosecond real-time observation of electron tunnelling in atoms," *Nature*, vol. 446, no. 7136, p. 627, 2007.

[67] L. A. MacColl, "Note on the Transmission and Reflection of Wave Packets by Potential Barriers," *Physical Review*, vol. 40, p. 621, 1932.

[68] H. G. Winful, "The meaning of group delay in barrier tunnelling: a re-examination of superluminal group velocities," *New Journal of Physics*, vol. 8, p. 101, 2006.

[69] T. J. Lewis, "Interfaces and nanodielectrics are synonymous," in *Proceedings of the 2004 IEEE International Conference on Solid Dielectrics*, p. 792, IEEE, 2004. 8th IEEE International Conference on Solid Dielectrics, Toulouse, France, 05-09 July, 2004.

[70] J. K. Nelson and Y. Hu, "Nanocomposite dielectrics - properties and implications," *Journal of Physics D-Applied Physics*, vol. 38, no. 2, p. 213, 2005.

[71] D.-W. Kim, D.-H. Lee, B.-K. Kim, H.-J. Je, and J.-G. Park, "Direct assembly of BaTA-poly(methyl methacrylate) nanocomposite films," *Macromolecular Rapid Communications*, vol. 27, no. 21, p. 1821, 2006.

[72] N. G. Devaraju and B. I. Lee, "Dielectric behavior of three phase polyimide percolative nanocomposites," *Journal of Applied Polymer Science*, vol. 99, no. 6, p. 3018, 2006.

[73] L. Qi, B. I. Lee, W. D. Samuels, G. J. Exarhos, and S. G. Parler, Jr., "Three-phase percolative silver-BaTiO3-epoxy nanocomposites with high dielectric constants," *Journal of Applied Polymer Science*, vol. 102, no. 2, p. 967, 2006.

[74] L. Li, A. Takahashi, J. J. Hao, R. Kikuchi, T. Hayakawa, T. A. Tsurumi, and M. A. Kakimoto, "Novel polymer-ceramic nanocomposite based on new concepts for embedded capacitor application (I)," *IEEE Transactions on Components and Packaging Technologies*, vol. 28, no. 4, p. 754, 2005.

[75] Z. M. Dang, L. Z. Fan, Y. Shen, and C. W. Nan, "Study on dielectric behavior of a three-phase CF/(PVDF+BaTiO3) composite," *Chemical Physics Letters*, vol. 369, no. 1-2, p. 95, 2003.

[76] C. Yang, Y. Lin, and C. W. Nan, "Modified carbon nanotube composites with high dielectric constant, low dielectric loss and large energy density," *Carbon*, vol. 47, no. 4, p. 1096, 2009.

[77] P. Kim, S. C. Jones, P. J. Hotchkiss, J. N. Haddock, B. Kippelen, S. R. Marder, and J. W. Perry, "Phosphonic acid-modiried barium titanate poly-

mer nanocomposites with high permittivity and dielectric strength," *Advanced Materials*, vol. 19, no. 7, p. 1001, 2007.

[78] L. Xie, X. Huang, C. Wu, and P. Jiang, "Core-shell structured poly(methyl methacrylate)/BaTiO(3) nanocomposites prepared by in situ atom transfer radical polymerization: a route to high dielectric constant materials with the inherent low loss of the base polymer," *Journal of Materials Chemistry*, vol. 21, no. 16, p. 5897, 2011.

[79] X. Huang, C. Kim, P. Jiang, Y. Yin, and Z. Li, "Influence of aluminum nanoparticle surface treatment on the electrical properties of polyethylene composites," *Journal of Applied Physics*, vol. 105, no. 1, p. 014105, 2009.

[80] L. F. Hakim, J. L. Portman, M. D. Casper, and A. W. Weimer, "Aggregation behavior of nanoparticles in fluidized beds," *Powder Technology*, vol. 160, no. 3, p. 149, 2005.

[81] A. Rasul, J. Zhang, D. Gamota, M. Singh, and C. Takoudis, "Flexible high capacitance nanocomposite gate insulator for printed organic field-effect transistors," *Thin Solid Films*, vol. 518, no. 23, p. 7024, 2010. Figure 2.12 is reprinted from *Thin Solid Films*, Volume 518, Issue 23, Rasul *et. al.*,"Flexible high capacitance nanocomposite gate insulator for printed organic field-effect transistors", 7024, Copyright (2010), with permission from Elsevier.

[82] S. B. Jones and S. P. Friedman, "Particle shape effects on the effective permittivity of anisotropic or isotropic media consisting of aligned or randomly oriented ellipsoidal particles," *Water Resources Research*, vol. 36, no. 10, p. 2821, 2000.

[83] P. Xu and Z. Y. Li, "Effect of particle shape on the effective dielectric

response of nanocomposite close to the percolation threshold," *Physica B-Condensed Matter*, vol. 348, no. 1-4, p. 101, 2004.

[84] K. W. Whites and F. Wu, "Effects of particle shape on the effective permittivity of composite materials with measurements for lattices of cubes," *IEEE Transactions on Microwave Theory and Techniques*, vol. 50, no. 7, p. 1723, 2002.

[85] A. Sihvola, "Dielectric polarization and particle shape effects," *Journal of Nanomaterials*, no. 1, p. 45090, 2007.

[86] Y. U. Wang and D. Q. Tan, "Computational study of filler microstructure and effective property relations in dielectric composites," *Journal of Applied Physics*, vol. 109, no. 10, SI, p. 104102, 2011. Figures 2.13 and 2.14 are reprinted from *Journal of Applied Physics*, 109, Wang *et al.*, "Computational study of filler microstructure and effective property relations in dielectric composites", 104102, Copyright (2011), with permission from AIP Publishing LLC.

[87] Y. U. Wang, "Phase field model of dielectric and magnetic composites," *Applied Physics Letters*, vol. 96, no. 23, p. 232901, 2010.

[88] Y. U. Wang, D. Q. Tan, and J. Krahn, "Computational study of dielectric composites with core-shell filler particles," *Journal of Applied Physics*, vol. 110, no. 4, p. 044103, 2011.

[89] W D Callister, Jr., *Materials Science And Engineering - An Introduction*. John Wiley & Sons, Inc., 2002.

[90] L A Dissado and J C Fothergill, *Electrical Degradation and Breakdown in Polymers*. Peter Peregrinus Ltd., London, United Kingdom, 1992.

[91] Ohki, Y. and Fuse, N. and Arai, T., "Band gap energies and localized states in several insulating polymers estimated by optical measurements," *Annual Report Conference on Electrical Insulation and Dielectric Phenomena (CEIDP)* , p. 1, 2010.

[92] K. Sreelatha and P. Predeep, "Iodine doped, semi-conducting nylon 6 polymers," *Journal of Plastic Film & Sheeting*, vol. 29, no. 2, p. 127, 2013.

[93] J. Artbauer, "Electric strength of polymers," *Journal of Physics D-Applied Physics*, vol. 29, no. 2, p. 446, 1996.

[94] A. E. Job, N. Alves, M. Zanin, and M. M. Ueki, "Increasing the dielectric breakdown strength of poly(ethylene terephthalate) films using a coated polyaniline layer," *Journal of Physics D-Applied Physics*, vol. 36, no. 12, p. 1414, 2003.

[95] I. L. Hosier, A. S. Vaughan, and S. G. Swingler, "The effects of measuring technique and sample preparation on the breakdown strength of polyethlyene," *IEEE Transactions on Dielectrics and Electrical Insulation*, vol. 9, no. 3, p. 353, 2002.

[96] A. Schneuwly, P. Groning, and L. Schlapbach, "Breakdown behavior of oil-impregnated polypropylene as dielectric in film capacitors," *IEEE Transactions on Dielectrics and Electrical Insulation*, vol. 5, no. 6, p. 862, 1998.

[97] V. A. Zakrevskii, N. T. Sudar, A. Zaopo, and Y. A. Dubitsky, "Mechanism of electrical degradation and breakdown of insulating polymers," *Journal of Applied Physics*, vol. 93, no. 4, p. 2135, 2003.

[98] X. Zhao, C. Hinchliffe, C. Johnston, P. J. Dobson, and P. S. Grant, "Spray deposition of polymer nanocomposite films for dielectric applications," *Materials Science and Engineering B-Advanced Functional Solid-State Materials*, vol. 151, no. 2, p. 140, 2008.

[99] J. I. Hong, P. Winberg, L. S. Schadler, and R. W. Siegel, "Dielectric properties of zinc oxide/low density polyethylene nanocomposites," *Materials Letters*, vol. 59, no. 4, p. 473, 2005.

[100] X. Zhao, *Spray Deposition of Nanostructured Materials for Energy Storage*. PhD thesis, University of Oxford, Oxford, UK, 2009.

[101] M. G. Todd and F. G. Shi, "Complex permittivity of composite systems: A comprehensive interphase approach," *IEEE Transactions on Dielectrics and Electrical Insulation*, vol. 12, no. 3, p. 601, 2005.

[102] P. Murugaraj, D. Mainwaring, and N. Mora-Huertas, "Dielectric enhancement in polymer-nanoparticle composites through interphase polarizability," *Journal of Applied Physics*, vol. 98, no. 5, p. 054304, 2005.

[103] Z.-M. Dang, S.-S. You, J.-W. Zha, H.-T. Song, and S.-T. Li, "Effect of shell-layer thickness on dielectric properties in Ag@TiO2 core@shell nanoparticles filled ferroelectric poly(vinylidene fluoride) composites," *Physica Status Solidi A - Applications and Materials Science*, vol. 207, no. 3, SI, p. 739, 2010.

[104] M. Rahimabady, M. S. Mirshekarloo, K. Yao, and L. Lu, "Dielectric behaviors and high energy storage density of nanocomposites with core-shell BaTiO3@TiO2 in poly(vinylidene fluoride-hexafluoropropylene)," *Physical Chemistry Chemical Physics*, vol. 15, no. 38, p. 16242, 2013.

[105] D. M. Taylor, "Space charges and traps in polymer electronics," *IEEE Transactions on Dielectrics and Electrical Insulation*, vol. 13, no. 5, p. 1063, 2006.

[106] Z. Chiguvare, "Electric field induced transition from electron-only to hole-only conduction in polymer-fullerene metal-insulator-metal devices," *Journal of Applied Physics*, vol. 112, no. 10, p. 104508, 2012.

[107] C. L. Yuan and P. S. Lee, "Enhanced charge storage capability of Ge/GeO(2) core/shell nanostructure," *Nanotechnology*, vol. 19, no. 35, p. 355206, 2008.

[108] D. K. Ray, A. K. Hirnanshu, and T. P. Sinha, "Structural and low frequency dielectric studies of conducting polymer nanocomposites," *Indian Journal of Pure & Applied Physics*, vol. 45, no. 8, p. 692, 2007.

[109] C. Zou, J. C. Fothergill, and S. W. Rowe, "The effect of water absorption on the dielectric properties of epoxy nanocomposites," *IEEE Transactions on Dielectrics and Electrical Insulation*, vol. 15, no. 1, p. 106, 2008.

[110] S. P. Bodhane and V. S. Shirodkar, "Change in crystallinity of poly(vinylidene fluoride) due to thermal evaporation," *Journal of Applied Polymer Science*, vol. 64, no. 2, p. 225, 1997.

[111] A. Kubono and N. Okui, "Polymer thin-films prepared by vapor-deposition," *Progress in Polymer Science*, vol. 19, no. 3, p. 389, 1994.

[112] H. Takele, H. Greve, C. Pochstein, V. Zaporojtchenko, and F. Faupel, "Plasmonic properties of Ag nanoclusters in various polymer matrices," *Nanotechnology*, vol. 17, no. 14, p. 3499, 2006.

[113] J. Affinito, P. Martin, M. Gross, C. Coronado, and E. Greenwell, "Vacuum deposited polymer metal multilayer films for optical application," *Thin Solid Films*, vol. 270, no. 1-2, p. 43, 1995.

[114] R. Ludwig, R. Kukla, and E. Josephson, "Vaccum web coating - State of the art and potential for electronics," *Proceedings of the IEEE*, vol. 93, no. 8, p. 1483, 2005.

[115] G. Abbas, Z. Ding, K. Mallik, H. Assender, and D. M. Taylor, "Hysteresis-

free vacuum-processed acrylate-pentacene thin-film transistors," *IEEE Electron Device Letters*, vol. 34, no. 2, p. 268, 2013.

[116] J. D. Affinito, "Hybridization of the polymer multi-layer (PML) deposition process," *Surface & Coatings Techonology*, vol. 133, p. 528, 2000.

[117] G. Abbas, H. Assender, M. Ibrahim, and D. M. Taylor, "Organic thin-film transistors with electron-beam cured and flash vacuum deposited polymeric gate dielectric," *Journal of Vacuum Science & Technology B*, vol. 29, no. 5, pp. 052401–1, 2011.

[118] J. D. Affinito, M. E. Gross, C. A. Coronado, G. L. Graff, E. N. Greenwell, and P. M. Martin, "A new method for fabricating transparent barrier layers," *Thin Solid Films*, vol. 290, p. 63, 1996.

[119] J. D. Affinito, S. Eufinger, M. E. Gross, G. L. Graff, and P. M. Martin, "PML/oxide/PML barrier layer performance differences arising from use of UV or electron beam polymerization of the PML layers," *Thin Solid Films*, vol. 308, p. 19, 1997.

[120] A. Kubono, N. Yuasa, H. Shao, S. Umemoto, and N. Okui, "In-situ study on alternating vapor deposition polymerization of alkyl polyamide with normal molecular orientation," *Thin Solid Films*, vol. 289, no. 1-2, p. 107, 1996.

[121] K. S. Giesfeldt, R. M. Connatser, M. A. De Jesus, P. Dutta, and M. J. Sepaniak, "Gold-polymer nanocomposites: studies of their optical properties and their potential as SERS substrates," *Journal of Raman Spectroscopy*, vol. 36, no. 12, p. 1134, 2005.

[122] S. Alismail and C. A. Hogarth, "Novel sources for metal-loaded polymer-films prepared by vacuum evaporation," *Journal of Physics E-Scientific Instruments*, vol. 20, no. 3, p. 344, 1987.

[123] K. P. Gritsenko and A. M. Krasovsky, "Thin-film deposition of polymers by vacuum degradation," *Chemical Reviews*, vol. 103, no. 9, p. 3607, 2003.

[124] D. W. Schubert and T. Dunkel, "Spin coating from a molecular point of view: its concentration regimes, influence of molar mass and distribution," *Materials Research Innovations*, vol. 7, no. 5, pp. 314–321, 2003.

[125] J. Lu, K.-S. Moon, and C. P. Wong, "High-k polymer nanocomposites as gate dielectrics for organic electronics applications," in *57th Electronic Components & Technology Conference, 2007 Proceedings*, Electronic Components and Technology Conference, p. 453, 2007.

[126] I. S. Bhardwaj, V. Kumar, A. B. Mathur, and A. Das, "Characterization of multiphase polymer system - nylon-6 ABS blends," *Journal of Thermal Analysis*, vol. 36, no. 7-8, p. 2339, 1990.

[127] D. B. Williams and C. B. Carter, *Transmission Electron Microscopy*. Springer, 2 ed., 2009.

[128] D. A. Shirley, "High-resolution X-ray photoemission spectrum of valence bands of gold," *Physical Review B*, vol. 5, no. 12, p. 4709, 1972.

[129] D. Briggs and M. P. Seah, ed., *Practical Surface Analysis*, vol. 1. Wiley, 2 ed., 1990.

[130] Veeco Instruments Inc., *Dektak 6M Manual*.

[131] S. H. Lim, A. C. Rastogi, and S. B. Desu, "Electrical properties of metal-ferroelectric-insulator-semiconductor structures based on ferroelectric polyvinylidene fluoride copolymer film gate for nonvolatile random access memory application," *Journal of Applied Physics*, vol. 96, no. 10, p. 5673, 2004.

[132] J. Xu, S. Bhattacharya, P. Pramanik, and C. P. Wong, "High dielectric constant polymer-ceramic (epoxy varnish-barium titanate) nanocomposites at moderate filler loadings for embedded capacitors," *Journal of Electronic Materials*, vol. 35, no. 11, p. 2009, 2006.

[133] G. G. Raju, *Dielectrics in Electrical Fields*. Marcel Dekker, New York, 2003.

[134] H. K. Reimschuessel, "Relationships on the effect of water on glass transition temperature and young's modulus of nylon 6," *Journal of Polymer Science: Polymer Chemistry Edition*, vol. (16), p. 1229, 1978.

[135] G. M. Turky, A. M. Ghoneim, A. Kyritsis, K. Raftopoulos, and M. A. Moussa, "Dielectric dynamics of some nylon 6/CaCo3 composites using broadband dielectric spectroscopy," *Journal of Applied Polymer Science*, vol. 122, no. 3, p. 2039, 2011.

[136] E. Laredo, M. Grimau, F. Sanchez, and A. Bello, "Water absorption effect on the dynamic properties of nylon-6 by dielectric spectroscopy," *Macromolecules*, vol. 36, no. 26, p. 9840, 2003.

[137] J. D. Reid, W. H. Lawrence, and R. P. Buck, "Dielectric-properties of an epoxy-resin and its composite .1. Moisture effects on dipole relaxation," *Journal of Applied Polymer Science*, vol. 31, no. 6, p. 1771, 1986.

[138] L. L. Marsh, D. C. Vanhart, and S. M. Kotkiewicz, "A dielectric loss investigation of moisture in epoxy-glass composites," *IBM Journal of Research and Development*, vol. 29, no. 1, p. 18, 1985.

[139] P. Gonon, A. Sylvestre, J. Teysseyre, and C. Prior, "Combined effects of humidity and thermal stress on the dielectric properties of epoxy-silica composites," *Materials Science and Engineering B-Solid State Materials for Advanced Technology*, vol. 83, no. 1-3, p. 158, 2001.

[140] Y. P. Khanna, W. P. Kuhn, and W. J. Sichina, "Reliable measurements of the nylon-6 glass-transition made possible by the new dynamic DSC," *Macromolecules*, vol. 28, no. 8, p. 2644, 1995.

[141] H. Zhao and R. K. Y. Li, "Effect of water absorption on the mechanical and dielectric properties of nano-alumina filled epoxy nanocomposites," *Composites Part A-Applied Science and Manufacturing*, vol. 39, no. 4, SI, p. 602, 2008.

[142] V. S. Yadav, D. K. Sahu, Y. Singh, and D. C. Dhubkarya, "The Effect of Frequency and Temperature on Dielectric Properties of Pure Poly Vinylidene Fluoride (PVDF) Thin Films," in *International Multiconference of Engineers and Computer Scientists (IMECS 2010), Vol I-III* (Ao, SI and Castillo, O and Douglas, C and Feng, DD and Lee, JA, ed.), p. 1593, 2010. International Multi-Conference of Engineers and Computer Scientists 2010, Hong Kong, Peoples Republic of China, 17-19 March, 2010.

[143] L. L. Marsh, R. Lasky, D. P. Seraphim, and G. S. Springer, "Moisture solubility and diffusion in epoxy and epoxy-glass composites," *IBM Journal of Research and Development*, vol. 28, no. 6, p. 655, 1984.

[144] K. I. Ivanova, R. A. Pethrick, and S. Affrossman, "Investigation of hydrothermal ageing of a filled rubber toughened epoxy resin using dynamic mechanical thermal analysis and dielectric spectroscopy," *Polymer*, vol. 41, no. 18, p. 6787, 2000.

[145] J. V. Florio, "Dielectric properties of alumina at high temperatures," *Journal of the American Ceramic Society*, vol. 43, no. 5, p. 262, 1960.

[146] P. Katiyar, C. Jin, and R. J. Narayan, "Electrical properties of amorphous aluminum oxide thin films," *Acta Materialia*, vol. 53, no. 9, p. 2617, 2005.

[147] B. G. Segda, M. Jacquet, and J. P. Besse, "Elaboration, characterization and dielectric properties study of amorphous alumina thin films deposited by r.f. magnetron sputtering," *Vacuum*, vol. 62, no. 1, p. 27, 2001.

[148] B. R. Strohmeier, "An ESCA method for determining the oxide thickness on aluminum-alloys," *Surface And Interface Analysis*, vol. 15, no. 1, p. 51, 1990.

[149] N. Reuvers, H. Huinink, and O. Adan, "Water plasticizes only a small part of the amorphous phase in nylon-6," *Macromolecular Rapid Communications*, vol. 34, no. 11, p. 949, 2013.

[150] Y. Zhang, Y. Wang, Y. Deng, M. Li, and J. Bai, "Enhanced Dielectric Properties of Ferroelectric Polymer Composites Induced by Metal-Semiconductor Zn-ZnO Core-Shell Structure," *ACS Applied Materials & Interfaces*, vol. 4, no. 1, p. 65, 2012.

[151] A. Mahadevegowda, N. P. Young, and P. S. Grant, "Electron microscopy of multi-layered polymer-nanocomposite based dielectrics," *Journal of Physics: Conference Series*, vol. 522, p. 012041, 2014.

[152] W. Benhadjala, I. Bord-Majek, L. Bechou, E. Suhir, M. Buet, F. Rouge, V. Gaud, B. Plano, and Y. Ousten, "Improved performances of polymer-based dielectric by using inorganic/organic core-shell nanoparticles," *Applied Physics Letters*, vol. 101, no. 14, p. 142901, 2012.

[153] V. Zaporojtchenko, T. Strunskus, K. Behnke, C. Von Bechtolsheim, A. Thran, and F. Faupel, "Formation of metal-polymer interfaces by metal evaporation: influence of deposition parameters and defects," *Microelectronic Engineering*, vol. 50, no. 1-4, p. 465, 2000.

[154] J. A. Venables, G. D. T. Spiller, and M. Hanbucken, "Nucleation and growth of thin-films," *Reports on Progress in Physics*, vol. 47, no. 4, p. 399, 1984.

[155] J. F. Silvain and J. J. Ehrhardt, "An overview on metal/PET adhesion," *Thin Solid Films*, vol. 236, p. 230, 1993.

[156] M. D. Thoreson, J. Fang, A. V. Kildishev, L. J. Prokopeva, P. Nyga, U. K. Chettiar, V. M. Shalaev, and V. P. Drachev, "Fabrication and realistic modeling of three-dimensional metal-dielectric composites," *Journal of Nanophotonics*, vol. 5, p. 051513, 2011.

[157] A. Goswami, *Thin Film Fundamentals*. New Age International Publishers, New Delhi, 2005.

[158] Nelson, J K, ed., *Dielectric Polymer Nanocomposites*. Springer, 2010.

[159] J. Y. Kim, H. S. Jung, J. H. No, J.-R. Kim, and K. S. Hong, "Influence of anatase-rutile phase transformation on dielectric properties of sol-gel derived TiO2 thin films," *Journal of Electroceramics*, vol. 16, no. 4, p. 447, 2006.

[160] B. Babuji, C. Balasubramanian, and M. Radhakrishnan, "Dilectric-properties of ion plated titanium-oxide thin-films," *Journal of non-crystalline solids*, vol. 55, no. 3, p. 405, 1983.

[161] Q. Cheng, W. Ahmad, G. Liu, and K. Wang, "Structural Evolution of Amorphous Thin Films of Titanium Dioxide," in *11th IEEE International Conference on Nanotechnology*, IEEE-NANO, p. 1598, IEEE, 2011. 11th IEEE International Conference on Nanotechnology, 15-18 August, 2011, Portland, Oregon, USA.

[162] W. G. Lee, S. I. Woo, J. C. Kim, S. H. Choi, and K. H. Oh, "Preparation and properties of amorphous TiO2 thin-films by plasma-enriched chemical-vapor-deposition," *Thin Solid Films*, vol. 237, no. 1-2, p. 105, 1994.

[163] T. Busani and R. Devine, "Dielectric and infrared properties of TiO2 films containing anatase and rutile," *Semiconductor Science and Technology*, vol. 20, no. 8, p. 870, 2005.

[164] C. W. Nan, Y. Shen, and J. Ma, "Physical Properties of Composites Near Percolation," in *Annual Review of Materials Research* (Clarke, DR and Ruhle, M and Zok, F, ed.), vol. 40 of *Annual Review of Materials Research*, p. 131, Annual Reviews, 2010.

[165] M. Panda, V. Srinivas, and A. K. Thakur, "On the question of percolation threshold in polyvinylidene fluoride/nanocrystalline nickel composites," *Applied Physics Letters*, vol. 92, no. 13, 2008.

[166] Y. Zou, Z.-A. Wang, X.-H. Lan, N.-K. Huang, and C.-F. Wang, "Anatase phase TiO2 anode of a dye-sensitized solar cell prepared by using rmfms," *Journal of the Korean Physical Society*, vol. 55, no. 6, 1, SI, p. 2650, 2009.

[167] D. B. Zhang, L. M. Qi, J. M. Ma, and H. M. Cheng, "Formation of crystalline nanosized titania in reverse micelles at room temperature," *Journal of Materials Chemistry*, vol. 12, no. 12, p. 3677, 2002.

[168] A. K. Srivastava, M. Deepa, S. Bhandari, and H. Fuess, "Tunable nanostructures and crystal structures in titanium oxide films," *Nanoscale Research Letters*, vol. 4, no. 1, p. 54, 2009.

[169] D. Shectman, D. Vanheerden, and D. Josell, "FCC titanium in Ti-Al multilayers," *Materials Letters*, vol. 20, no. 5-6, p. 329, 1994.

[170] Y. Zhang, M. Ma, N. Gu, L. Xu, and K. J. Chen, "Preparation of silver nanoshells on silica particles by a simple two-step process," *Chinese Chemical Letters*, vol. 15, no. 8, p. 1005, 2004.

[171] W. Wei, X. Mao, L. A. Ortiz, and D. R. Sadoway, "Oriented silver oxide nanostructures synthesized through a template-free electrochemical route," *Journal of Materials Chemistry*, vol. 21, no. 2, p. 432, 2011.

[172] G. J. Kovacs and P. S. Vincett, "Formation and thermodynamic stability of a novel class of useful materials - close-packed monolayers of sub-micron monodisperse spheres just below a polymer surface," *Journal of Colloid and Interface Science*, vol. 90, no. 2, p. 335, 1982.

[173] G. J. Kovacs, P. S. Vincett, C. Tremblay, and A. L. Pundsack, "Vacuum deposition onto softenable substrates - formation of novel subsurface structures," *Thin Solid Films*, vol. 101, no. 1, p. 21, 1983.

[174] C. von Bechtolsheim, V. Zaporojtchenko, and F. Faupel, "Influence of thermal treatment on the morphology and adhesion of gold films on trimethylcyclohexane-polycarbonate," *Applied Surface Science*, vol. 151, no. 1-2, p. 119, 1999.

[175] Q. M. Zhang, H. F. Li, M. Poh, F. Xia, Z. Y. Cheng, H. S. Xu, and C. Huang, "An all-organic composite actuator material with a high dielectric constant," *Nature*, vol. 419, no. 6904, p. 284, 2002.

[176] J. H. Klootwijk, K. B. Jinesh, W. Dekkers, J. F. Verhoeven, F. C. van den Heuvel, H. D. Kim, D. Blin, M. A. Verheijen, R. G. R. Weemaes, M. Kaiser, J. J. M. Ruigrok, and F. Roozeboom, "Ultrahigh capacitance density for multiple ALD-grown MIM capacitor stacks in 3-D silicon," *IEEE Electron Device Letters*, vol. 29, no. 7, p. 740, 2008.

[177] P. Banerjee, I. Perez, L. Henn-Lecordier, S. B. Lee, and G. W. Rubloff, "Nanotubular metal-insulator-metal capacitor arrays for energy storage," *Nature Nanotechnology*, vol. 4, no. 5, p. 292, 2009.

[178] J. I. Sohn, Y. S. Kim, C. Nam, B. K. Cho, T. Y. Seong, and S. Lee, "Fabrication of high-density arrays of individually isolated nanocapacitors using anodic aluminum oxide templates and carbon nanotubes," *Applied Physics Letters*, vol. 87, no. 12, p. 123115, 2005.

[179] M. Kemell, M. Ritala, M. Leskela, E. Ossei-Wusu, J. Carstensen, and H. Foell, "Si/Al2O3/ZnO : Al capacitor arrays formed in electrochemically etched porous Si by atomic layer deposition," *Microelectronic Engineering*, vol. 84, no. 2, p. 313, 2007.

[180] F. Roozeboom, R. Elfrink, J. Verhoeven, J. van den Meerakker, and F. Holthuysen, "High-value MOS capacitor arrays in ultradeep trenches in silicon," *Microelectronic Engineering*, vol. 53, no. 1-4, p. 581, 2000.

[181] K. B. Shelimov, D. N. Davydov, and M. Moskovits, "Template-grown high-density nanocapacitor arrays," *Applied Physics Letters*, vol. 77, no. 11, p. 1722, 2000.